The Sigma-Lambda Transition Magnetic Moment

PRISCILLA CUSHMAN PETERSEN

October, 1985

Supported in part by:
National Science Foundation

Department of Physics and Astronomy

RUTGERS
THE STATE UNIVERSITY
OF NEW JERSEY

E-619

THE SIGMA-LAMBDA TRANSITION MAGNETIC MOMENT

by

Priscilla Cushman Petersen

A dissertation submitted to the

Graduate School-New Brunswick

Rutgers, The State University of New Jersey

in partial fulfillment of the requirements

for the degree of

Doctor of Philosophy

Graduate Program in Physics

Written under the direction of

Professor Thomas J. Devlin

and approved by

Thomas J. Devlin

Glenn R. Farrar

Gordon B. Thomson

Haruo Kojima

New Brunswick, New Jersey

October 1985

AAB1886

ABSTRACT OF THE THESIS

The Sigma-Lambda Transition Magnetic Moment

by

Priscilla Cushman Petersen

Dissertation Director: Professor Thomas J. Devlin

The Primakoff effect was utilized in a measurement of the Σ°-Λ transition magnetic moment at the Fermilab neutral hyperon facility. A beam containing Λ's with average momenta of 150 GeV/c passed through a target. A small fraction of them interacted with the Coulomb field of the target nuclei to produce a Σ° which subsequently decayed via the process: $\Sigma^{\circ} \rightarrow \Lambda\gamma$.

A sample of 5×10^5 $\Lambda\gamma$ events were analyzed for 7 different targets, and yielded a total of 2028 ± 139 Coulomb-produced Σ°'s. The total Primakoff cross sections for Λ on beryllium, tin, and lead were determined to be $\sigma_{Be} = 0.033 \pm 0.022$ mb, $\sigma_{Sn} = 3.28 \pm 0.34$ mb, and $\sigma_{Pb} = 9.20 \pm 0.81$ mb. There is an additional 7% systematic uncertainty.

The Primakoff formalism predicts $\sigma \propto Z^2 \mu_{\Sigma\Lambda}^2$, where $\mu_{\Sigma\Lambda}$ is the Σ°-Λ transition magnetic moment. A least-squares fit of the experimental cross sections to this functional form yielded $|\mu_{\Sigma\Lambda}| = (1.59 \pm 0.05 \pm 0.05)$ nuclear magnetons. This corresponds to a Σ° lifetime of $\tau = (0.76 \pm 0.05 \pm 0.05) \times 10^{-19}$ seconds or a radiative width of $\Gamma = (8.6 \pm 0.6 \pm 0.6)$ keV, where the uncertainties are statistical and systematic, respectively. An additional uncertainty due to approximations in the Primakoff formalism applies to these derived quantities: <5% on τ and Γ, and <2.5% on $|\mu_{\Sigma\Lambda}|$.

ACKNOWLEDGEMENTS

A High Energy Physics experiment is impossible without the efforts of many dedicated professionals and a spirit of cooperation. All members of the collaboration contributed their time and expertise, and deserve acknowledgement in this paper.

A special note of thanks goes to Cat James for her consistent and capable management of the midnight shift, and for her coffee. Andy Beretvas, Lee Pondrom, Gordon Thomson, and Ken Heller may be indelibly associated with carpets, a 6 ft. cake, luminescent spots, and meatloaf, but they were also responsible for many helpful suggestions and enlightening physics discussions.

I am also grateful to Tom Devlin, whose penchant for a well-ordered Portakamp was reflected in his careful perusal of this document. His enthusiasm and persistence were a great encouragement during some of the bleaker periods of this analysis.

Finally, I wish to thank my husband, Rod, for his patience and support; and for our shared belief in a created order, which has given a deeper meaning to the process of scientific inquiry.

TABLE OF CONTENTS

Abstract ii

Acknowledgements iii

Table of Contents iv

List of Tables vii

List of Figures viii

1. Introduction 1

2. The Experimental Apparatus 10

    1. Introduction 10

    2. Primary Beam 11

    3. Secondary Beam 15

    4. Primakoff Target and Decay Volume 17

    5. Charged Particle Detection 20

    6. Gamma Detection 26

    7. Trigger and Associated Electronics 30

    8. Data Acquisition 32

    9. Running Procedures 35

    10. Chamber Alignment 38

    11. Drift Chamber Calibration 39

    12. Lead Glass Calibration 41

3. Analysis I: Event Reconstruction and Simulation 47

    1. Introduction 47

    2. The Λ Reconstruction 48

    3. The Σ° Reconstruction 53

    4. Data Consistency 61

5. Monte Carlo Data Simulation 65

1. Event Generation 65

2. Charged Track Resolution 67

3. Glass Simulation 72

4. Acceptance 76

4. Analysis II: Cross Section 81

1. Cross Section Definition and Related Terms 81

1. Photon Acceptance 84

2. Software Cuts 84

3. Albedo Correction 85

4. Glass Trigger Efficiency 89

2. Primakoff Σ° Signal 91

1. Introduction 91

2. Further Kinematic Cuts 94

3. Failure of Strong Kinematic Constraint Method .. 95

4. Multi-dimensional Statistical Analysis 104

1. Introduction 104

2. Input Populations 105

3. Global Fit 106

4. Background Subtraction 111

3. Strong Production of Σ°'s 118

4. Subtraction of Non-target Primakoff Σ°'s 126

5. Beam Λ Normalization 128

6. Cross Section Calculation 130

7. Systematic Uncertainties 133

5. Results and Conclusions 137

1. Introduction 137

2. Nuclear Absorption Correction 138

3. Electron Screening 139

4. Transition Magnetic Moment 141

5. Comparison with previous experiment 143

6. Comparison with Theory 144

Appendix A : TDC Event Offset Problem 150

1. Introduction 150

2. The Cause of the Event Offset Problem 151

3. Drift Chamber Event Offset Correction 152

4. Lead Glass Event Offset Correction 154

Appendix B : The Primakoff Cross Section 155

1. Formulae and Definitions 155

2. Corrections to Previous Experiment 158

References 162

Vita 165

LIST OF TABLES

1. Chapter 1

1. Baryon Magnetic Moments 4

2. Chapter 2

1. Primakoff Target Properties 19

2. Data Tape Summary 37

3. Drift Chamber Resolution 41

3. Chapter 3

1. Summary of Software Cuts 54

2. Data Consistency 62

3. Drift Chamber Efficiency 71

4. Chapter 4

1. Albedo Calculation 88

2. Glass Trigger Efficiency 90

3. Results of Global Fit 116

4. Invariant Mass Fit 117

5. Strong Production of Σ^{o}'s 123

6. Non-Target Coulomb Production 127

7. Beam Λ Normalization 129

8. Cross Section and Magnetic Moment 131

Appendix B

1. Revised Dydak Table 161

LIST OF FIGURES

1. Chapter 1

1. Form Factor Corrections 9

2. Chapter 2

1. Schematic of Spectrometer 12

2. Beam Transport System 14

3. Collimator Design 16

4. Λ Momentum Spectrum 18

5. Primakoff Target Manipulator 21

6. Drift Chamber Design 23

7. Lead Glass Array 27

8. Schematic of Trigger 33

9. Lead Glass Calibration 43

3. Chapter 3

1. Kinematic minus Geometric χ^2 51

2. Geometric χ^2 52

3. Λ Decay Vertex Distribution 55

4. Λ Mass Distribution 56

5. Shower Energy (Non-cluster) 58

6. Shower Energy (Cluster) 59

7. Angular Resolution 69

8. Ratio of Glass Array Energies 73

9. Λ Acceptance 77

10. Σ° Acceptance 78

11. Ξ° Acceptance 79

4. Chapter 4

1. $\Lambda\gamma$ Invariant Mass (Tgts 1-4) 92

2. $\Lambda\gamma$ Invariant Mass (Tgts 5-7) 93

3. Λ Target Pointing Distributions 96

4. Σ° Target Pointing Distributions 97

5. Λ Transverse Momentum Distributions 98

6. Σ° Transverse Momentum Distributions 99

7. Σ°-Λ Transverse Momentum Distributions 100

8. Shower Energy vs Position 101

9. $\Lambda\gamma$ Invariant Mass with Tight Cuts 103

10. $\Lambda\gamma$ Invariant Mass vs Q^2 108

11. Background Q^2 and $\Lambda\gamma$ Invariant Mass 111

12. $\Lambda\gamma$ Invariant Mass after Background Subtraction (tgt 1) 112

13. $\Lambda\gamma$ Invariant Mass after Background Subtraction (tgt 2-3) 113

14. $\Lambda\gamma$ Invariant Mass after Background Subtraction (tgt 4-5) 114

15. $\Lambda\gamma$ Invariant Mass after Background Subtraction (tgt 6-7) 115

16. $\Lambda\gamma$ Invariant Mass with $Q^2 > 0.1$ (tgt 1) 119

17. $\Lambda\gamma$ Invariant Mass with $Q^2 > 0.1$ (tgt 2-3) 120

18. $\Lambda\gamma$ Invariant Mass with $Q^2 > 0.1$ (tgt 4-5) 121

19. $\Lambda\gamma$ Invariant Mass with $Q^2 > 0.1$ (tgt 6-7) 122

20. Strong Production of Σ°'s 125

21. Primakoff Σ° Cross Section 132

5. Chapter 5

1. Σ°-Λ Transition Magnetic Moment 142

CHAPTER 1

Introduction

The magnetic moment is a valuable probe of the internal structure of a particle. It is defined as $\overline{\mu}_B = \frac{g}{2}\frac{q}{mc}\overline{S}$, where $\overline{S}$ is the spin. For pointlike particles with half-integral spin, Dirac theory predicts intrinsic moments of $\overline{\mu} = \frac{q}{mc}\overline{S}$. Thus the value of g gives a measure of how closely the particle matches the Dirac ideal: g=2 for charged particles and g=0 for neutral particles. The close agreement of lepton magnetic moments with g=2 is a result of their pointlike properties. Deviations from the Dirac value are called anomalous moments and give evidence for internal structure. In the case of the leptons, the anomaly is completely accounted for by higher order Quantum Electrodynamic (QED) corrections. In other words, the internal structure of electrons and muons is caused by virtual photon loops.

The baryons, on the other hand, have very large anomalous moments. This is consistent with their being composite objects rather than pointlike. In the most current models, the baryons are made up of three quarks, bound together by the strong force. Calculations of the baryon magnetic moments from first principles thus requires detailed knowledge of the quark-quark interactions in this three-body system. Perturbation theory, which was so successful in QED, is not as helpful when applied to the theory of strong interactions (Quantum Chromodynamics or QCD) because the correction terms are higher order in α_s (~1) rather than α_e (~1/137).

Due to the complexity of the situation, it is not surprising that QCD is not yet in a position to make theoretical predictions of the magnetic moments which approach the level of experimental accuracy. Lattice gauge calculations are just beginning to yield reasonable values for the hyperon masses and the proton and neutron moments[1]. On the other hand, group theoretical constraints and models of quark confinement do make some fairly accurate predictions. For example, in a naïve SU(6) quark model the wave functions of the baryons are regarded as s-wave states of three quarks, symmetric in space, spin, and flavor, and antisymmetric in color. The baryon magnetic moment is then the vector sum of the constituent quark moments:

$\bar{\mu}_B = \sum_i \langle B| \bar{\mu}_i |B\rangle$. Here $|B\rangle$ represents the baryon wave function and μ_i is the magnetic moment operator for each quark. Each constituent quark, whether up (u), down (d), or strange (s), is assumed to have intrinsic moments μ_u, μ_d, and μ_s. By inserting the SU(3) X SU(2) wavefunctions into the equation for μ_B, the magnetic moments of each baryon can be described as a linear combination of quark moments[2]. Using the experimental values for the p, n, and Λ magnetic moments, the three equations for μ_p, μ_n, and μ_Λ can be solved for the quark moments. The moments of the other members of the $\frac{1}{2}$ (+) baryon octet can then be deduced from the quark moments. Table 1.1 lists these predictions and compares them with the experimental values.

Stated in a more general way, the diagonal elements of the matrix $\langle F|H_{em}|I\rangle$ yield the static magnetic moments, where H_{em} is the electromagnetic interaction Hamiltonian and $|I\rangle$ and $|F\rangle$ refer to the initial and final state baryon wave functions. The off-diagonal elements give amplitudes for photo-production and radiative decay. The static moments of the baryon octet (with the exception of Σ°) have all been measured using spin precession in a magnetic field[3], transitions in exotic atoms[4], or Nuclear Magnetic Resonance for the nucleons. The only non-zero off-diagonal element is the Σ° radiative decay: $\Sigma^\circ \rightarrow \Lambda\,\gamma$. It is an M1 transition whose expectation value can be called the Σ°-Λ transition

Table 1.1

Baryon Magnetic Moments

Baryon	Quark Model Prediction	Experiment[a] (in nuclear magnetons)
p	input	2.7928456(11)
n	input	-1.91304184(88)
Λ	input	-0.613 ± 0.004
Σ^+	2.67	2.379 ± 0.020
Σ^-	-1.09	-1.10 ± 0.05
Ξ^0	-1.43	-1.253 ± 0.014
Ξ^-	-0.49	-0.69 ± 0.04[b]
Ω^-	-1.84	-2.1 ± 1.0[c]
Σ^0-Λ	-1.63	-1.61 ± 0.07[d]

(a) Particle Data Group, Rev Mod Phys 56, S1 (1984) (except as noted).

(b) New world average including R. Rameika et al., Phys Rev Lett 52,581(1984).

(c) K.B.Luk, Ph.D. Thesis, Rutgers University 1983, (unpublished).

(d) New world average including the value reported in this paper.

magnetic moment, or $\mu_{\Sigma\Lambda} = \langle\Lambda|H_{em}|\Sigma^\circ\rangle$. Seen from this perspective, the transition moment is just as fundamental a property as the static moments.

A direct measurement of $\mu_{\Sigma\Lambda}$ is not possible with existing techniques. Fermi's Golden Rule states that the rate, or decay width, is proportional to $|\langle F|H_{em}|I\rangle|^2$. Using Dirac spinors, the Σ° width can be written $\Gamma = \tau^{-1} = 4\ \mu^2_{\Sigma\Lambda}\ k^3$ in natural units, where k = momentum of the decay γ in the Σ° center of mass system[5]. Thus, one might hope to find the moment by lifetime estimates in a bubble chamber or maybe the width of the resonance. However, since the Σ° decay is electromagnetic, the lifetime is of the order of 10^{-19} seconds which produces a track too short to measure directly, and a corresponding width, 10 keV, much smaller than the resolution presently attainable.

Fortunately, an indirect method does exist. The transition magnetic moment can be determined by measuring the cross section of the inverse process: electromagnetic production of Σ°'s in the Coulomb field of the nucleus. That the cross section for $Z+\Lambda \rightarrow Z+\Sigma^\circ$ is proportional to $\Sigma^\circ \rightarrow \Lambda\ \gamma$ was demonstrated independently by Dreitlein and Primakoff[6] and Pomeranchuk and Shmushkevitch[7], and is commonly referred to as the Primakoff effect (or simply Coulomb production). The form of the differential cross section is as follows:

$$\frac{d\sigma}{dq^2} = 98\left(\frac{Z}{82}\right)^2\left(\frac{\mu_{\Sigma\Lambda}}{\mu_N}\right)^2 \frac{p_\Lambda^2}{m_\Lambda^4}\left(\frac{q_l q_t}{q^2}\right)^2 F^2(q^2) \quad \text{mb/GeV}^2 \qquad (1.1)$$

where

$m_\Lambda, m_{\Sigma^\circ}$ = Λ, Σ° rest masses

Z = Nuclear charge

p_Λ = incident Λ momentum

$q_l = (m_{\Sigma^\circ}^2 - m_\Lambda{}^2)/2p_\Lambda$ = longitudinal momentum transfer

$q_t = p_\Lambda \sin\theta_{\Sigma\Lambda}$ = transverse momentum transfer

$q^2 = q_l{}^2 + q_t{}^2$

$F(q^2)$ = a dimensionless form factor of order unity which includes the effects of the charge distribution and nuclear absorption, and is therefore model dependent.

In this expression c=1 and masses and momenta are expressed in GeV.

Once a form for $F(q^2)$ is determined, the differential cross section can be integrated to give a total cross section. In particular, a black sphere model of nuclear absorption with nuclear radius $R=1.14A^{\frac{1}{3}}$, yields the closed form solution presented here.

$$\sigma(\Sigma^\circ)_{Pk} = 0.496\left(\frac{Z}{82}\right)^2\left(\frac{\mu_{\Sigma\Lambda}}{\mu_N}\right)^2\{(2+u^2)\ln(2/u) - 2.154 + 0.423u^2\} \text{ mb} \qquad (1.2)$$

where $u = q_l R$. Fäldt et al.[8] have shown that this assumption is a good approximation to a partially absorbing sphere.

Equation 1.2 has the advantage of explicitly displaying some of the features which distinguish the Primakoff process from competing strong processes. The Primakoff cross section depends only logarithmically on the energy and nuclear radius, but varies quadradically with Z. Thus, targets of different material but the same number of radiation lengths should yield equal numbers of Primakoff Σ^0's. Production by strong processes will actually drop for the higher Z targets, since the interaction length gets smaller more slowly than the radiation length as Z increases. By using various targets in the beam, this Z^2 dependence can be used to confirm the Coulomb nature of the signal.

A second characteristic feature of Coulomb production is apparent from the form of the differential cross section (Eq. 1.1). The cross section has a sharp maximum at $q_t = q_l$ and then falls off rapidly as q_t increases. Thus the Primakoff signal is concentrated at such small q_t (~1 MeV/c for 200 GeV incident Λ's) that any observable width in q_t is due solely to the experimental resolution. On the other hand, Σ^0's produced by strong interactions cover a large range of q_t and can therefore be eliminated by examining the q_t dependence of the data.

The purpose of this experiment is to determine the number of Σ°'s produced in various target materials by an incoming Λ beam, to separate the Coulomb-produced Σ°'s from the strongly produced Σ°'s, and by normalizing to the incident Λ's establish the total cross section. From this cross section, the transition moment and Σ° lifetime can be calculated using the Primakoff formalism. In the final analysis, we use a complete optical model of a partially absorbing sphere rather than Eq. 1.2. The full treatment includes nuclear absorption of incoming and outgoing hyperons and screening of the Coulomb field by orbital electrons. The change in the theoretical cross section due to these corrections and normalized to the cross section with $F(q^2)=1$ (impulse approximation) is shown in Fig 1.1 for lead as a function of momentum transfer. It can be seen from this figure that at Fermilab energies, we are close to the minimum necessary correction.

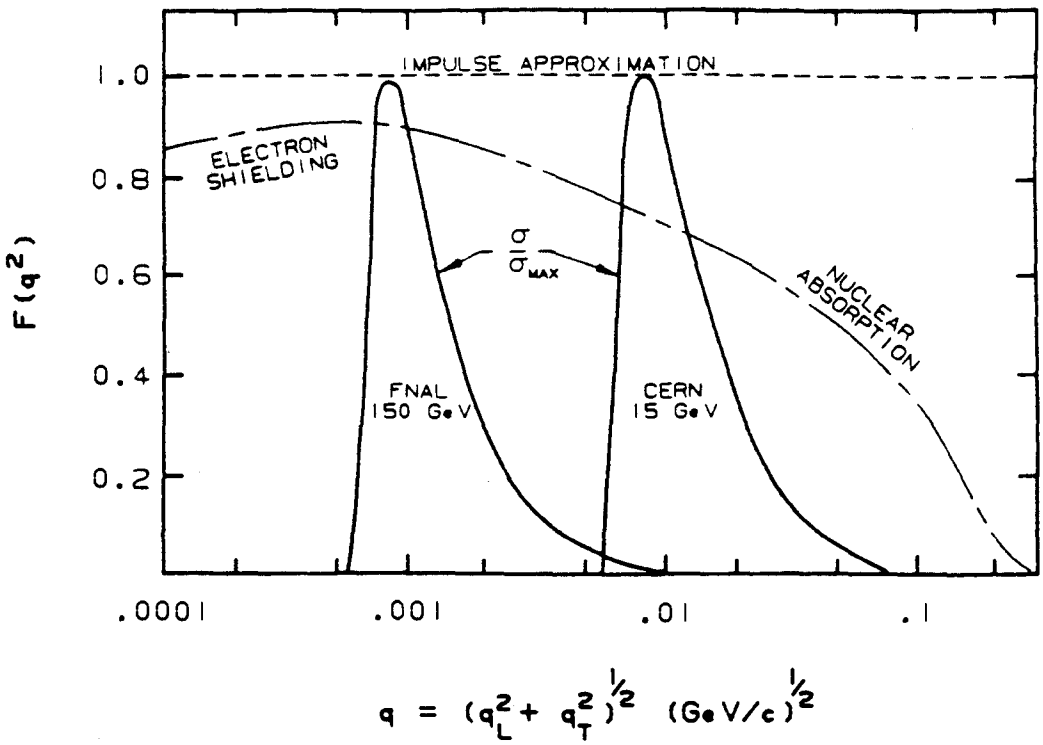

Figure 1.1 Deviations from $F(q^2)=1$ due to corrections for nuclear absorption, the finite charge distribution of the nucleus, and shielding by orbital electrons, plotted as a function of momentum transfer. Normalized Primakoff cross sections for neutral beam energies corresponding to both Fermilab and CERN experiments are shown.

CHAPTER 2

The Experimental Apparatus

2.1 Introduction

The goal of this experiment (E619 in Fermilab nomenclature) was to measure the cross section of the process $Z+\Lambda \rightarrow Z+\Sigma^{\circ}$. E619 was performed in the Fermilab Proton Center beam line in the Spring of 1982. In order to produce an incident beam of Λ hyperons, 400 GeV protons were steered onto a lead target where high energy reactions produced a variety of secondary particles. Charged particles were removed from the secondary beam as it passed through a long magnetized collimator and the resulting neutral beam was incident on one of seven secondary targets of various materials and thicknesses. A certain fraction of the time, the Λ's in this neutral beam interacted with a target nucleus

to produce a Σ°. Σ°'s produced in the secondary or "Primakoff" target immediately decayed through the reaction $\Sigma^{\circ} \rightarrow \Lambda \gamma$.

A spectrometer consisting of two magnets and eight multi-wire proportional chambers (MWPC's), supplemented by three drift chambers, detected the charged particles from the Λ decay. The p and π^- formed a narrow cone upstream of the magnets and were bent to the east (p) and west (π^-) downstream of them. This topology will hereafter be referred to as a 'vee'. The photon energy and position were detected by a lead glass array downstream of the spectrometer. This information was sufficient to fully reconstruct the events of interest and distinguish them from a background of other processes. A schematic of the spectrometer is shown in Fig 2.1.

2.2 Primary Beam

The Fermilab Synchroton was operated at an energy of 400 GeV. Protons were extracted and sent to the experimental areas every 8-15 seconds in beam spills one second in duration. This primary beam was delivered to the Proton Center pre-target area from the upstream enclosure at an angle of .05 mrad from the nominal beam line, entering the area 3 cm west of the line.

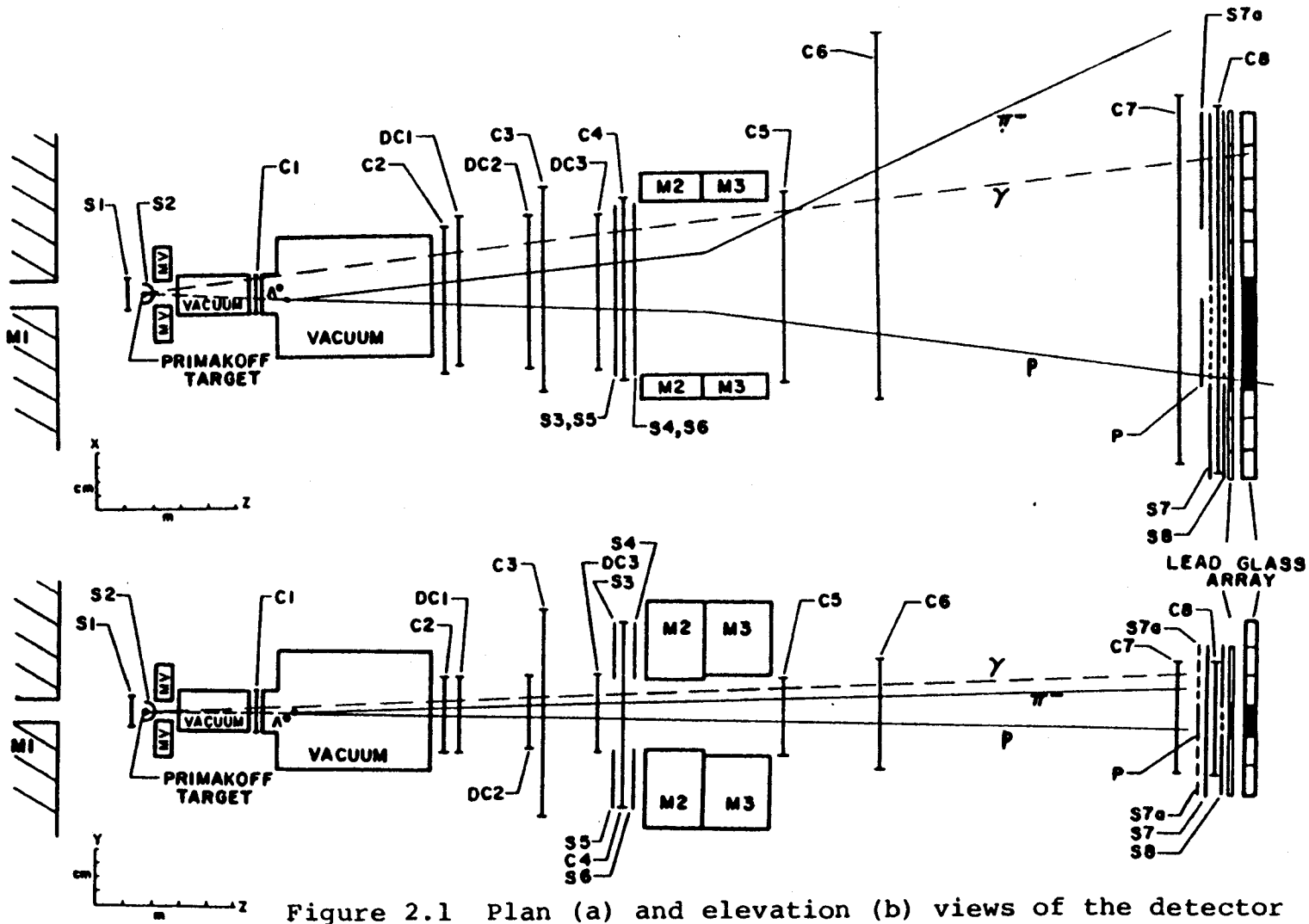

Figure 2.1 Plan (a) and elevation (b) views of the detector apparatus where S1-S8 are scintillation counters, MV and M1-M3 are magnets, C1-C8 are MWPC's and DC1-DC3 are drift chambers. Tracks corresponding to production of a Σ^{o} at the Primakoff target and the subsequent decay $\Sigma^{o} \rightarrow \Lambda \gamma$ are also shown.

The beam transport system in the pre-target area is shown in Fig 2.2. Five quadrupole magnets focussed the beam at the production target. A 3-meter-long dipole and one vernier dipole steered the beam onto the production target in the horizontal plane, and aligned it with the collimator. The production angle was controlled by four vertical bending magnets. The two upstream verniers deflected the beam from the median plane and the two downstream dipoles restored it to the plane at the target. By adjusting the magnet currents it was possible to set the production angle anywhere in the range between -5 to +5 mrad. The verniers were adjusted to deliver ± 3.2 mrad during the experiment. A roughly equal number of tapes were taken at each polarity. Later comparison between the Λ momentum spectrum generated by empirical differential cross section formulae[9] (adjusted for the spectrometer acceptance) and the Λ momentum spectrum for each of the two data samples indicated that the production angles were closer to +3.1 and -3.4 mrad.

The production target was a 1-mm-square and 1/4-interaction-length long piece of lead, positioned 30 cm inside the upstream face of the sweeper magnet, M1. It was mounted on a remotely-controlled manipulator which enabled us to position the target in or out of the beam. Two segmented wire ion chambers (SWIC) with 2-mm wire spacing were located at the entrance of the pre-target area and 11.6 meters

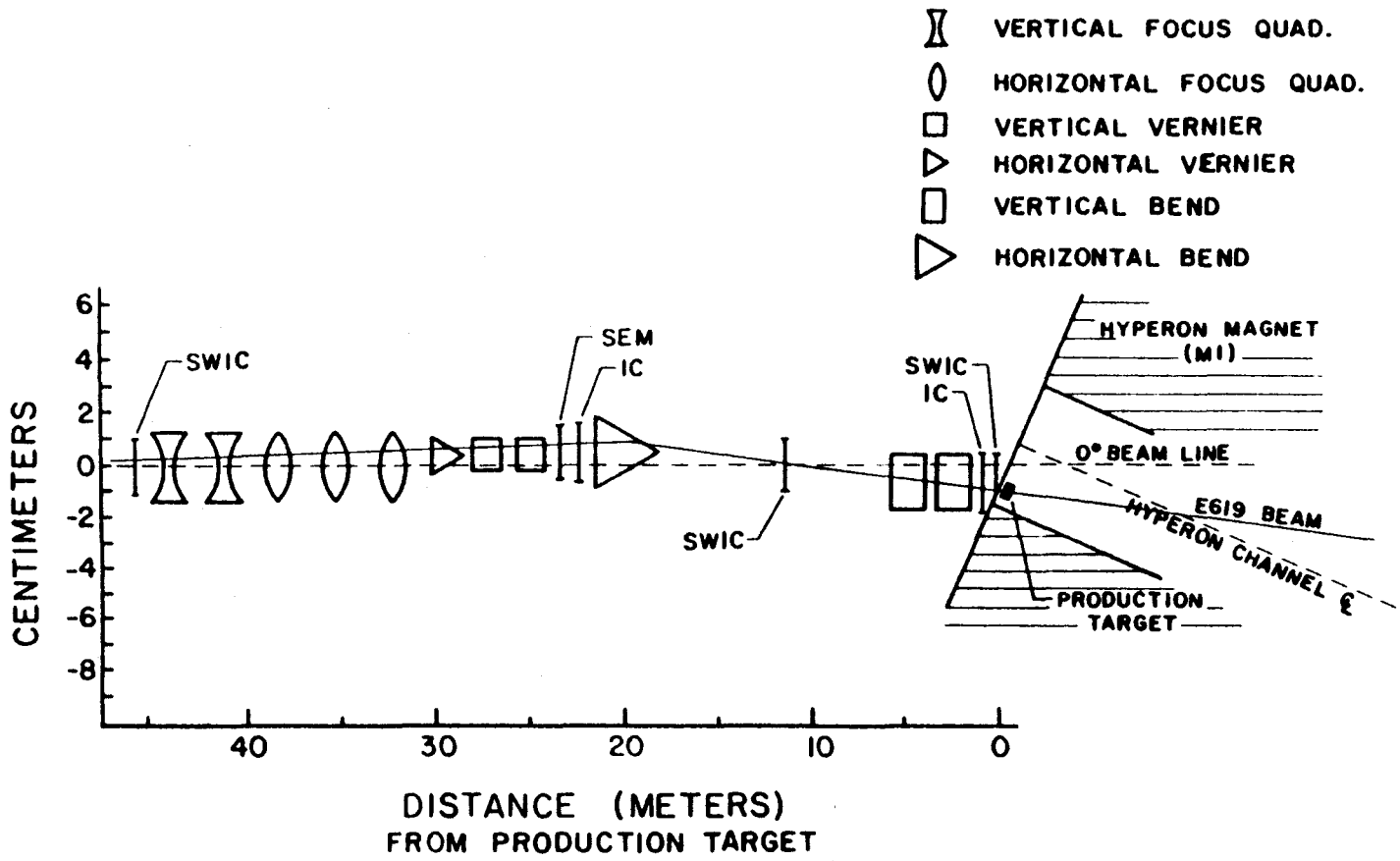

Figure 2.2 Plan view of the beam transport system in the pre-target area. Note that the x-scale (and consequently any x-z angle) is greatly expanded.

upstream of the target (-11.6 m). They, as well as a 0.5-mm SWIC immediately preceding the target, monitored the position and focus of the proton beam. The intensity was monitored by a secondary emission monitor (SEM) located at -23 m and two ion chambers (IC) at -23 m and -0.3 m. We operated at intensities between 10^{10}-10^{11} protons per spill in data-taking mode.

2.3 Secondary Beam

The secondary beam then passed through a collimator embedded in M1, a 7.3 meter long dipole with a vertical field of 35 kgauss ($\int Bdl$ = 24.5 tesla-meters). The collimator entrance was offset 2.5 cm east of the magnet center line and passed through the magnet at a 7 mrad angle to emerge 2.5 cm west of center. The collimator consisted of twelve brass blocks with circular apertures ranging from 0.2 cm to 2.5 cm in diameter. A tungsten insert in the eighth block provided a defining aperture 2 mm in diameter and 76 cm long. See Fig 2.3 for the details of the collimator geometry.

Within this defining aperture, thirteen teflon coated 3-mm-thick uranium plugs served as a filter to reduce the photon flux in the beam. The positions of the plugs were chosen to optimize the filtering process: photon conversion

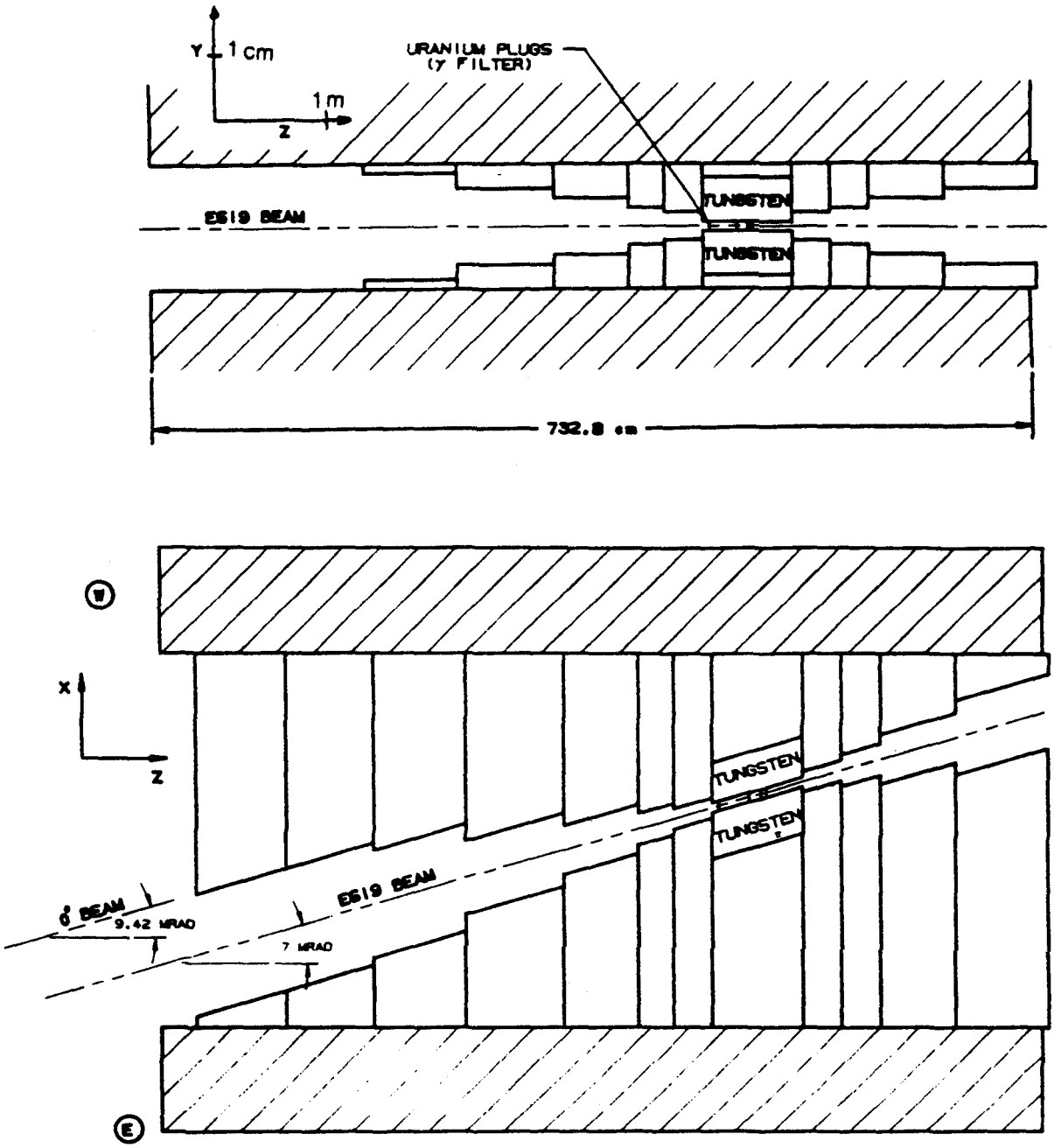

Figure 2.3 Elevation (a) and plan (b) views of the collimator which was embedded in the sweeper magnet, M1. The collimator defined a neutral beam by sweeping charged particles out of the channel. The defining apperture was 2 mm in diameter.

in the material and subsequent deflection of the e^+e^- pairs out of the channel. The singles rate in chamber C2, normalized to the beam intensity, was reduced by a factor of eight after insertion of the γ filter, whereas the normalized rate of Λ triggers was only reduced by a factor of two, indicating that the device was eliminating a significant fraction of the background created by photons in the neutral beam. A downstream photon monitor indicated a reduction factor of five, corroborating the above evidence.

A neutral beam of mostly Ξ°, Λ, γ, K°, and neutrons emerged from the exit aperture of this collimator. The momentum spectrum of the Λ component, shown in Fig 2.4, was peaked at 150 GeV.

2.4 Primakoff Target and Decay Volume

A scintillation veto counter, S1, just upstream of the Primakoff target insured that only incoming neutral particles were observed. There were seven targets used in this experiment: two of beryllium, two of tin, two of lead, and one of air. Their properties are listed in Table 2.1. Each target was 2 cm in diameter. Since the FWHM of the secondary beam at the target position is only 0.5 cm, essentially all the beam Λ's passed through the Primakoff target. The

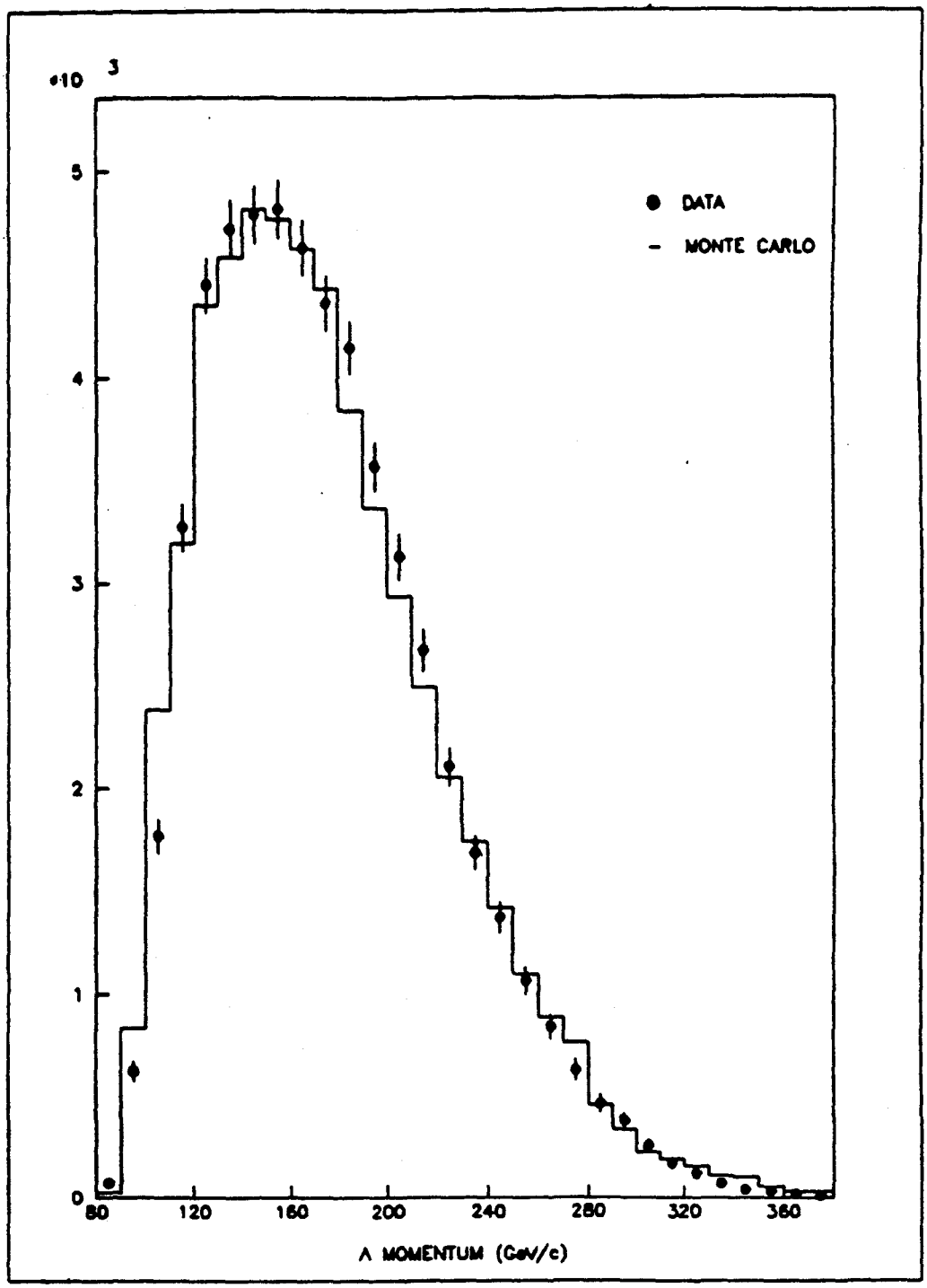

Figure 2.4 The momentum spectrum of Λ's emerging from the collimator. Both data and Monte Carlo are shown for reconstructed Λ's from the prescaled Λ' trigger.

Table 2.1

Primakoff Target Properties

Target No.	Material (Z)	Length L(cm)	L/L_{abs}	L/L_{rad}
1	Air (7)	--	--	--
2	Be (4)	1.1197	0.0305	0.0317
3	Be (4)	5.3303	0.1452	0.1510
4	Sn (50)	0.6942	0.0303	0.5737
5	Sn (50)	1.2082	0.0528	0.9985
6	Pb (82)	0.0821	0.0044	0.1467
7	Pb (82)	0.5609	0.0304	1.0016

targets were housed in aluminum cylinders attached to a rotating drum which was remotely operated to facilitate quick target changing. When a target was in position, it was encased in a sleeve of scintillator, S2, with an end cap. S2 provided a veto on charged particles exiting the target. Fig 2.5 shows the Primakoff target/veto configuration. An evacuated decay region ten meters long followed the Primakoff target.

2.5 Charged Particle Detection

A small 13 x 13 cm^2 MWPC, C1, with 1-mm wire spacing was inserted one third of the way along the decay pipe for improved track resolution. The rest of the MWPC's were of conventional design and are described in detail elsewhere[10]. Chambers C2 and C5-C8 consisted of horizontal and vertical signal planes with 2-mm wire spacing. In order to resolve track ambiguities during reconstruction, C3 was constructed with U and V planes: X and Y planes of 2-mm wire spacing rotated by 45 degrees about the z-axis. C4 contained X and Y planes plus an additional U plane with $2\sqrt{2}$ mm spacing. The MWPC's were filled with a gas mixture of 99.9% argon to 0.1% freon bubbled through methylal at 0°C. The operating voltages ranged from 2.8 - 3.2 kilovolts. Most of the chambers were centered on the beam line, defined by surveying through the

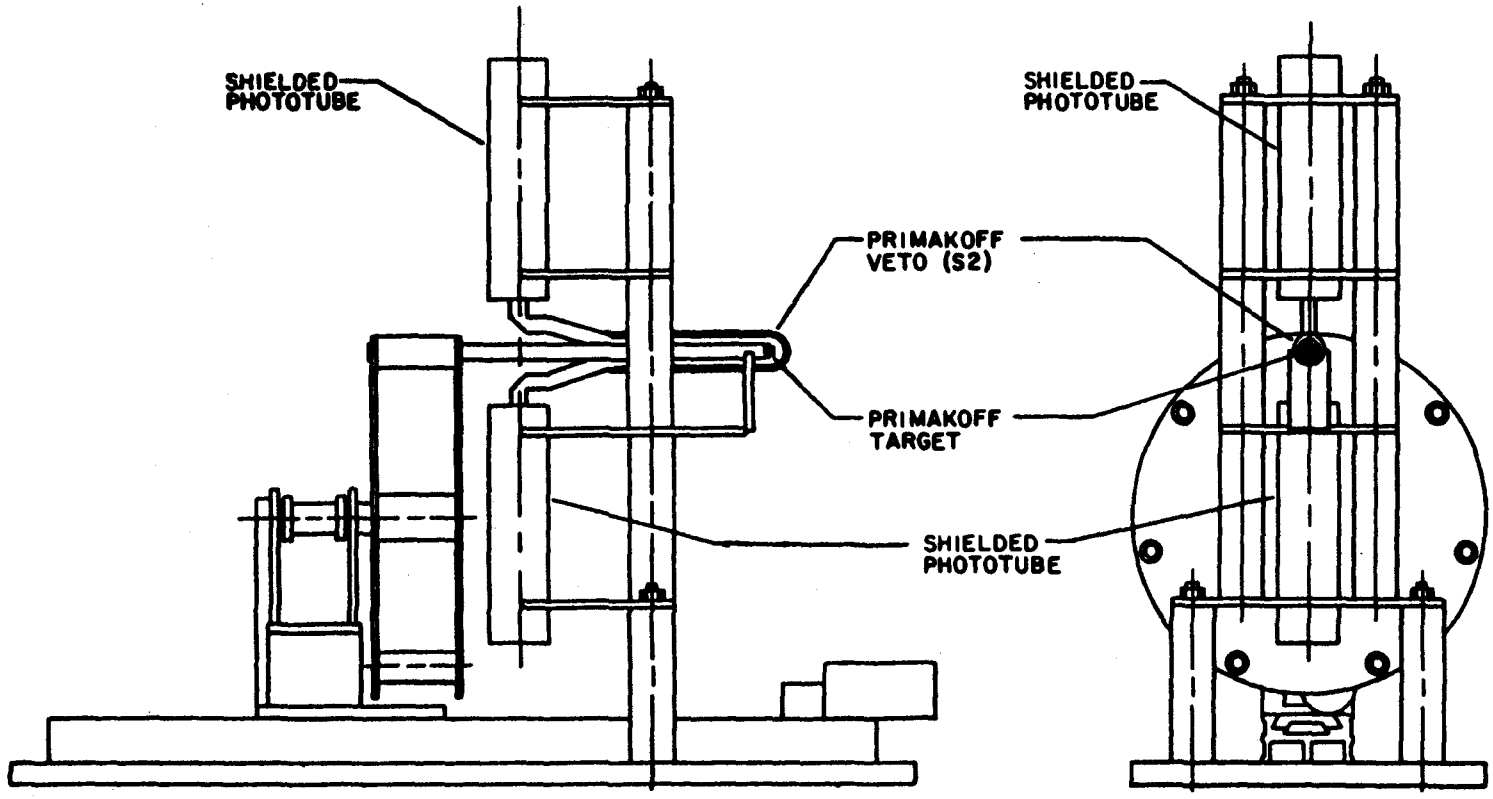

Figure 2.5 Design of the Primakoff target and manipulator. To change targets, a drum with 7 equally spaced aluminum target holders moved away from the phototube stand, freeing the target from the scintillator sleeve, rotated to the next position, and then moved forward to engage the new target.

collimator. C6, however, was offset 24 cm west of the beam line in order to cover the full spatial range of the low momentum π^-'s which were bent west by the spectrometer magnets (M2, M3).

Three drift chambers were located upstream of the analyzing magnet to improve target pointing resolution. Each consisted of two X and two Y sense planes offset by half a cell from each other to resolve left-right cell ambiguities. There were 26 Y wires and 52 X wires per chamber. The sense wires of 25 μm gold-plated tungsten alternated with 125 μm beryllium-copper field wires to produce cells 2 cm across. The field planes consisted of 375 μm (for V_4) and 62 μm (for V_1,V_2) BeCu wires with a spacing of 0.5 cm. Guard and ground planes of 225 μm BeCu isolated the drift regions from each other. A typical cell and the order of planes are shown in Fig 2.6.

The field wire voltages V_0-V_4 were chosen to optimize the field uniformity within a cell, and were run with the following ratios:

$$V_0 = 0.28\ V_4$$
$$V_1 = 0.31\ V_4$$
$$V_2 = 0.49\ V_4$$
$$V_3 = 0.80\ V_4$$

The drift chambers were operated at V_4 = 3.2 kilovolts, drawing a current of 170 μamps. They were filled with argon

DRIFT CHAMBER CONSTRUCTION

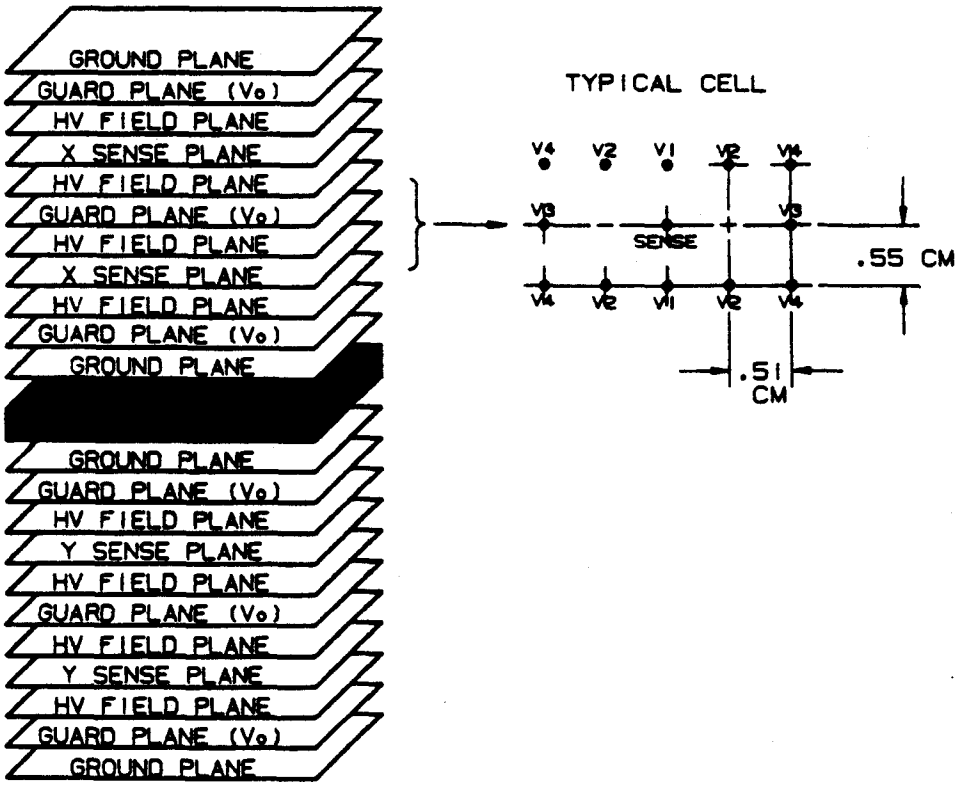

Figure 2.6 The order of planes and a typical cell from the drift chambers. V_0-V_4 are the voltages applied to the wires and S refers to the sense wire.

and ethane in a mixture ratio of 1:1. The gas mixture was bubbled through alcohol at 0°C. An outer box with mylar windows enclosed the drift chamber and associated electronics. This was sealed and continuously flushed with dry nitrogen to minimize oxygen and water contamination of the inner chamber and to prevent sparking in the electrical connections.

The signals were converted to differential ECL pulses by sets of LeCroy DC201A discriminators attached to the chamber bases. The differential pulses were transmitted to the electronics room via a flat twisted pair cable. A LeCroy 2270A time-to-digital converter (TDC) initiated time encoding at the receipt of the pulse and halted processing when it received a "common stop" signal from the delayed event trigger. The combination of a malfunction in the TDC's and a problem associated with the data acquisition system caused drift chamber information from one event to be associated with spectrometer information from a different one. A major effort was made to recover this information, and, to a large degree, it suceeded. The details can be found in Appendix A.

The two analyzing magnets M2 and M3, each 2.5 meters long, had apertures of 61 x 25 cm^2 and 61 x 30 cm^2 respectively. They were operated at currents which gave field values of 15 and 12 kilogauss. Together they delivered

a total transverse momentum transfer of 1.57 GeV/c. Over the course of the experiment the momentum transfer changed by as much as 4% because of regulation problems. It was corrected on a run-to-run basis by comparing the measured Λ mass with its known value. The total field strength was chosen such that the lower momentum π^-'s would be swept off the lead glass array to the west and the higher momentum protons would pass through a four-block hole near the array center. The field integral at operating current was measured precisely after the experiment using a Fermilab field-mapping device called the Ziptrack. This device consisted of three orthogonal induction coils which moved along an adjustable track under computer control. The field was uniform to 1% in the central region several centimeters from any magnet boundary. The second magnet was found to be rotated about the z-axis by 7.5 mrad. This was calculated from the magnitude of the y-component of the magnetic field measured by the Ziptrack. It was confirmed by a later survey. The effect of the fringe field was negligible.

Polyethylene bags filled with helium were mounted between all the chambers and inside the analyzing magnets in order to reduce multiple scattering.

2.6 Gamma Detection

The primary detector for γ-rays was a lead glass array divided into two parts: a front wall and a main array. The constituent blocks were made of type F2 lead glass manufactured by Schott and by Ohara with a radiation length of 32 mm. The arrays were made up of 90 such blocks with dimensions of 10.0 x 10.0 x 38.4 cm^3. RCA 6342/V1 phototubes screwed into a threaded lucite plate which was glued onto the endface of a block, applying pressure evenly to the optical grease joint. A small hole was drilled in the corner of the lucite square to accomodate an optical fiber from a light pulser monitoring system.

Twenty-four blocks were arranged vertically in two rows to make up the front wall. The remaining 66 were stacked horizontally in a main array with alternate rows displaced relative to their neighbors by half a block width (see Fig 2.7). Together the arrays provided 15 radiation lengths of material.

Both arrays were stacked in a steel box which was mounted on rails transverse to the beam direction enabling the whole structure to be moved 1.5 m in either direction. Once the box was surveyed in place, a bolt was inserted into the cement floor to prevent accidental displacement. The

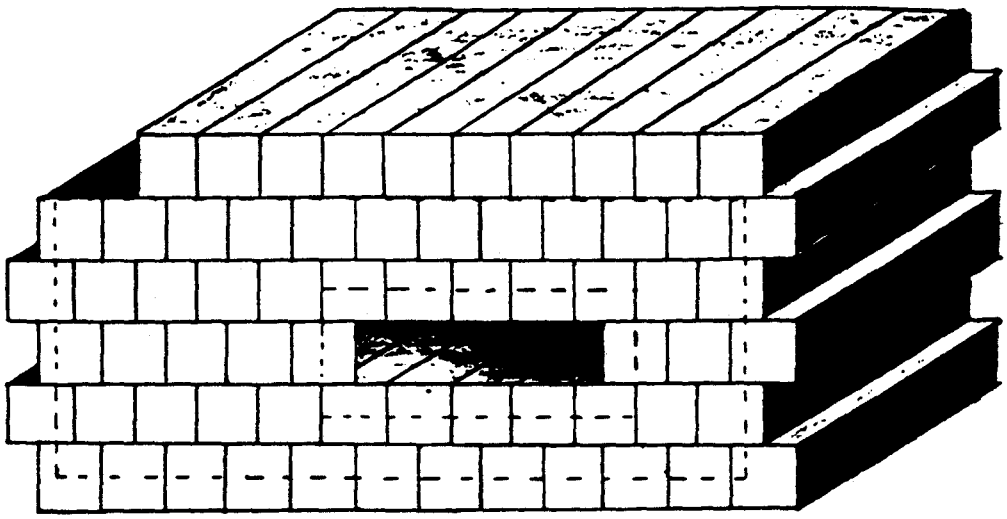

Fig. 2.7 (a)

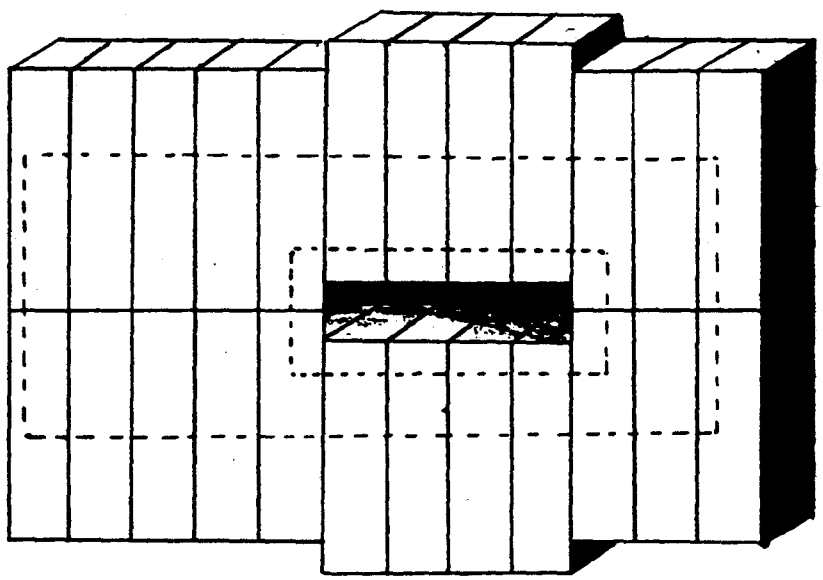

Figure 2.7 The geometry of the main array (a) and front wall (b) lead glass block arrays. The dashed line defines the boundary of the fiducial volume.

upstream face of the front wall was located 42 meters downstream of the sweeper magnet exit. At this distance all the photons from the Σ° decay which passed through the analyzing magnets were intercepted by interior blocks, i.e. blocks not on the outer perimeter of the array.

Three LeCroy HV4032 modules supplied the high voltage to the phototube bases. The modules were remotely controlled by the on-line computer and voltages were checked on a regular basis, approximately every eight hours.

All the phototubes used in the array were tested for linearity and rate dependence. A green light-emitting diode (LED) was inserted in the optical fiber hole and the photomultiplier signal was recorded for various input amplitudes, rates, and tube voltages. All the phototubes were operated in their linear regions for signals corresponding to 10 GeV photons. A typical tube was run at -1400 volts and displayed a 10% gain increase at rates above 1 MHz. Only eight tubes showed rate dependent effects above 100 KHz and they were placed at the edges of the array.

In order to distinguish between hadrons and photons entering the glass array, a 1-cm-thick lead converter was sandwiched between two 13-mm-thick scintillators S7 and S8. S7 and the lead were mounted on the upstream face of C8 and

S8 was mounted on the upstream face of the front wall glass array. The scintillators were acrylic doped with 10% napthalene. Light from the scintillator was reemitted by two BBQ waveshifter bars which were mounted along the horizontal edges of the scintillator, separated by a small air gap. Two phototubes were attached to each scintillator sheet: T1 and T2 on S7, T3 and T4 on S8.

S7 was used in veto in the trigger to eliminate charged particles in the glass. Since S7 was found to be inefficient in the region far from the phototube end, an extra scintillator S7a was installed, covering the west third of the glass array. Photons which converted in the lead were detected by S8, setting a corresponding latch bit. A 40 x 10 cm^2 hole in the scintillators, lead, and both glass arrays allowed the neutral beam and protons from Λ decay to pass through the array without interacting, and, thus, interfering with γ-ray detection.

A standard Monte Carlo program for generating electromagnetic showers (EGS[11]) was run with the detector geometry discussed above. It indicated that for photons in the 10-50 GeV range, only 3% of the energy was lost out the back of the array and less than 1% was absorbed in the inactive lead converter. See Section 3.5.3 for details about the EGS software package.

An auxilliary γ-ray detector was located in front of the spectrometer magnet to eliminate events with two photons. Two pairs of scintillation counters S3-S4 and S5-S6, each 61 x 24 cm^2 were attached to C4 directly above and below the M2 aperture. Each pair consisted of 1 cm of lead sandwiched between two 0.3 cm scintillators. The absence of a signal in the first scintillator and a hit in the second indicated that a photon had converted in the lead. The information was latched and used off-line to eliminate such events.

2.7 Trigger and Associated Electronics

Good events were selected by a simple vee topology (≥ 1 track in the right side and ≥ 1 track in the left side of the spectrometer), plus at least 2.5 GeV deposited in the glass. Each MWPC generated fast pulses corresponding to logical "OR"'s of all the horizontal wires and all the vertical wires. Upstream of the analyzing magnet at least one hit was required in C2, corresponding to the horizontal OR signal. Downstream, C6 was divided into two horizontal OR regions to distinguish between + and -. particles deflected by the magnet. The left chamber OR, denoted C6L, was triggered by the π^-. A 10.2 x 32.7 cm^2 scintillator, P, (the Proton Counter) was mounted across the hole in the glass array, and triggered on the protons. A veto on charged particles

entering and leaving the Primakoff target completed the charged particle trigger identified as $\Lambda=\overline{S1}\cdot\overline{S2}\cdot C2\cdot C6L\cdot P$. A second trigger defined as Λ' included a veto on charged particles entering the glass array: $\Lambda' = \Lambda\cdot(\overline{S7+S7a})$.

The Σ° trigger was a combination of Λ' and an energy criterion in the glass as follows. The signal from the anode output of each phototube was brought into the electronics room and split into three parts. One signal went to a Lecroy 2770A time-to-digital converter (TDC) via a LeCroy ECLine 4416 discriminator to suppress accidental γ's; the second to a LeCroy 2280 analog-to-digital converter (ADC) for pulse height information; and the third signal was used in the trigger. The trigger signals from all but the top row of main array blocks were fed into five LRS127 linear adders and the resulting signals were summed in a sixth adder. The summed signal then went to a discriminator with an output width of 40 nsec. The threshold was set at 32 mvolts which corresponded to an energy of roughly 2.5 GeV.

On average, an incident photon deposits approximately 25% of its energy in the front wall. For a given energy deposited in the array, the fraction in the front wall is much smaller for an incident hadron. Therefore an energy requirement was also placed on the front wall in order to provide some measure of hadron rejection. Signals from the

front wall were input to a linear adder. The summed signal was first amplified x 4 before input to a discriminator with the same threshold as that used by the main array. Over the course of the experiment, drifts in the LRS127 DC offsets and changes in the adder configurations caused drifts in the front wall energy threshold from 0.01 to 0.8 GeV, but a later software energy cut of 1 GeV rendered the final analysis insensitive to these changes.

The coincidence of the main array and front wall discriminator outputs and the Λ' trigger defined the Σ^0 trigger. The final E619 trigger consisted of Σ^0 triggers with Λ and Λ' triggers prescaled at the level of 2^9 (2^{10} for later higher rate tapes). A schematic of the experimental trigger and gating system is shown in Fig 2.8.

2.8 Data Acquisition

Whenever an event satisfied the trigger requirements, a "busy" logic level was generated to prevent further accumulation of data. An "enable" pulse was sent back to all the MWPC's to latch the wire hit information responsible for generating the fast OR, and a "common stop" pulse was sent to the TDC's to halt the time encoding and fill a FIFO buffer. The occurrance of a trigger also caused a priority interrupt

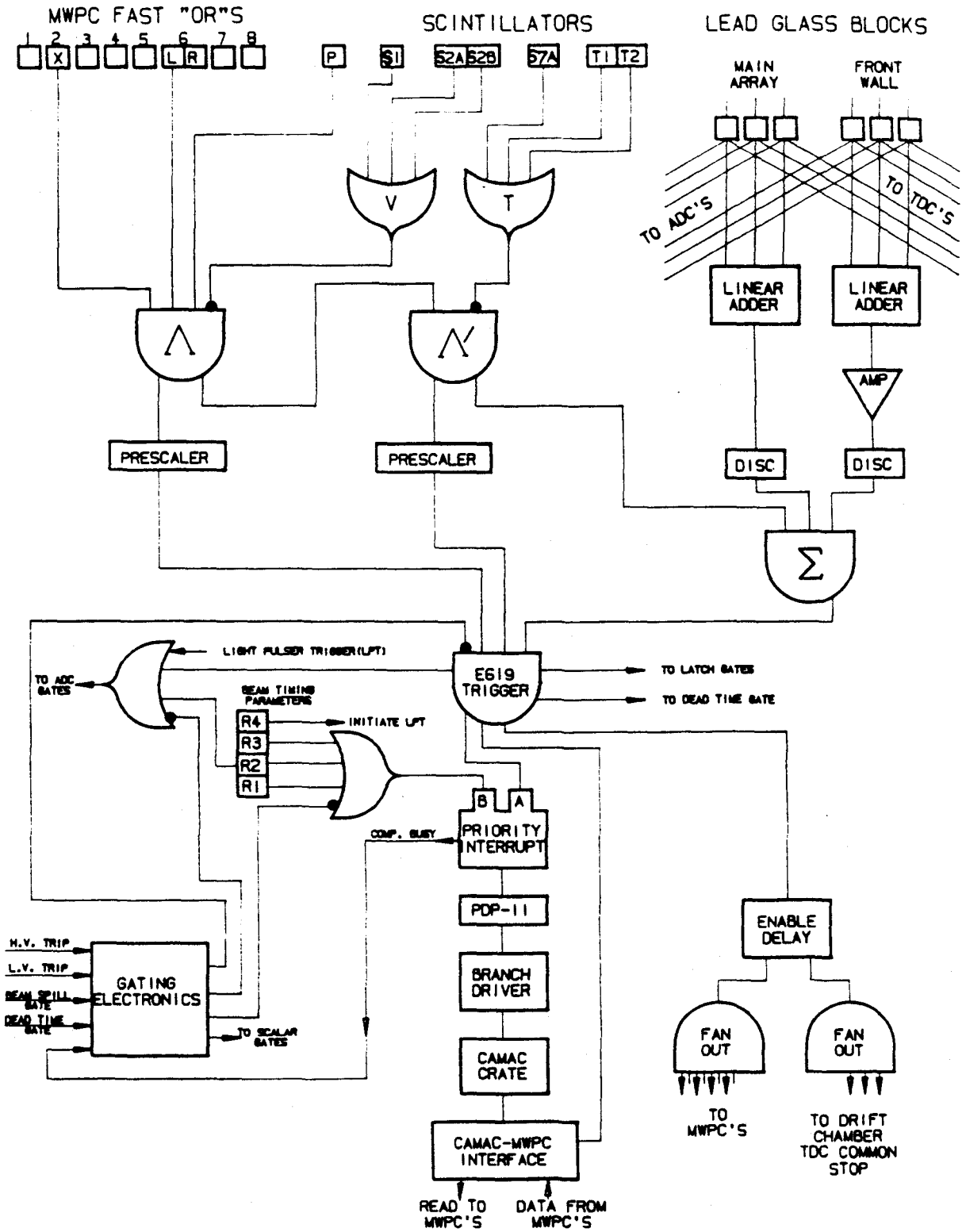

Figure 2.8 A schematic of the trigger electronics. The Λ, Λ', and Σ° triggers are correspondingly labeled and provide the input to the final coincidence gate labeled "E619 trigger".

(the A-interrupt) to be sent to the computer to instruct it to begin the read-out process.

The following data were recorded for each event:

1) MWPC wire hits, read out serially through the MWPC-CAMAC Interface,

2) drift chamber wire addresses and timing information from the three TDC's,

3) the position and pulse height of hits in the lead glass array from the ADC's,

4) timing information for the hits in the lead glass from the fourth TDC, and

5) latch settings for all scintillators and trigger configurations.

The MWPC wire hits, three sets of 16 latches, and all the TDC and ADC data were encoded as 16-bit words. A typical event from the Σ° trigger consisted of about 80 words.

Between spills, beam timing parameters (R1-R4) obtained from the accelerator main control were used to gate off the E619 trigger. Another priority interrupt (the B-interrupt) initiated the read out of a second set of data. Signals generated by the light pulsers and pedestals for every glass block were read from the ADC's. Scalar records accumulated during the spill were read and then zeroed. These records

included the number of triggers of each kind, the number of counts in each scintillator, and the C2 singles rate.

The data described above were written to 6250 BPI tape using a PDP11/45 and the standard CAMAC Interface. The on-line software, based on RT-MULTI[12], determined the record format and generated diagnostic histograms while the experiment was in progress.

2.9 Running Procedures

The behavior of the different spectrometer elements was monitored in various ways throughout the experiment in order to ensure proper operation and to detect failure or malfunction in any of the systems. Differential changes in the glass block efficiencies or problems in the chambers (especially amplifier card failure in the MWPC's) could be easily spotted in the on-line diagnostic histograms. Each MWPC also had a small 1-μCu Fe55 source directed at an independently instrumented wire. The signals produced by the 5.9 keV X-rays passed through an emitter follower and were viewed on an oscilloscope at least once every eight hours, to check on the condition of the MWPC gas mixture and high voltage. Once a stable operating voltage was established, these signals became the standard; their amplitude was kept

constant by small adjustments to the high voltage. Major failures, such as a high or low voltage trip in any of the chambers gated off the E619 trigger and B-interrupt electronics, and caused an alarm to sound.

Any other quantities judged to be of some diagnostic use, such as the beam intensity (SEM counts), the number of A and B-interrupts, the individual trigger rates, and the ungated C2 singles rate, were accumulated on scalars over the whole run. The scalar records, time of tape mount and dismount, magnet currents, phototube voltages, and general running conditions were recorded in a tape summary file.

Data tapes were taken under a number of conditions. The sign of the production angle and the polarity of the sweeper magnet current were changed several times in order to better understand possible systematic effects. The Primakoff target was changed every run to avoid any possible target dependence due to time-dependent running conditions. Running with the long, high Z targets was emphasized because of the greater percentage of Σ^0's expected per tape. Table 2.2 summarizes the number of tapes taken under all the above conditions. A typical data tape contained about 100,000 triggers or 700 spills at 140 events per spill.

Table 2.2

Data Tape Summary

Number of Data Tapes in the Final Analysis Sample
Taken at Different Running Conditions

Target	Production Angle (mrad) and MV Current (amps)				Totals
	-3.2 -3300.	+3.2 -3300.	-3.2 +3300.	+3.2 +3300.	
1	3	0	0	3	6
2	1	0	2	2	5
3	2	1	0	3	6
4	5	1	3	8	17
5	8	3	7	13	31
6	2	1	2	3	8
7	8	5	5	13	31
Totals	29	11	19	45	104

In addition to the 104 data tapes, there were a number of specialized tapes. Two "straight-through" tapes were taken for the purpose of aligning the MWPC's and drift chambers. One was taken at the beginning of the experiment and the other at roughly the midpoint. This process is described in more detail in the next section. Four sets of lead glass calibration tapes (18 tapes in all) were also obtained. Two of the sets were used to balance the phototube gains prior to their use in the trigger. The third set (taken at the beginning of the experiment) and the fourth set (taken at the midpoint) produced calibration constants for all the lead glass blocks. Their means of production and the calibration procedure are discussed in Section 2.12. Finally, four tapes were taken with various parts of the canonical trigger removed. They were helpful in isolating any inefficiencies in the trigger elements.

2.10 Chamber Alignment

In order to determine the relative positions of the MWPC sense wires with respect to the spectrometer coordinate system, several straight-through tapes were taken. The production target was removed and the sweeper and analyzing magnets turned off. A very low intensity proton beam ($\sim 10^5$/sec) was directed through the Proton Center collimator

and triggered scintillators at the upstream and downstream ends of the spectrometer. Hit positions were recorded in all wire chambers. The centroid of the hit distribution was determined to an accuracy of 0.1 mm. This method aligned the chambers without recourse to track reconstruction. Further refinements such as small corrections to the surveyed z-positions or rotations about an axis were obtained by reconstructing straight tracks (analyzing magnets off) and minimizing the residuals.

2.11 Drift Chamber Calibration

A first estimate of the drift chamber TDC calibration was made by noting the width (T) and the starting point (t_0) of the distribution of TDC counts for each channel. The drift length is defined as $X = X_c(t-t_0)/T$ where X_c is the chamber cell size. A typical width of 85 counts corresponded to 83 cts/cm or a drift velocity of 0.004 cm/nsec.

Next a clean sample of events was selected as follows. Since a sense wire can be excited by electrons from particles entering the cell on either side, there exists an inherent left-right ambiguity. The practice of using two planes offset by half a cell (ambiguity planes) resolves the problem. The chambers were scanned for hits in ajacent wires

of the two ambiguity planes. Hits with more than two adjacent wires were rejected. The sum of the drift lengths derived from the two wires was required to equal the cell size with a 2-mm tolerance. Only events where the charged tracks were separated by one or more cells were used.

The tracks fit from MWPC data alone were projected to the drift chamber planes and residuals were generated. T, t_0, and the wire positions were adjusted to give the narrowest residuals for each cell. Next, the drift chambers themselves were used to fine-tune the calibration. For example, tracks fitted with DC1 and DC3 were used to form residuals in DC2. The field generated by the high voltage planes was not completely uniform over the cell, giving slightly higher drift velocities near the sense wires. Hits within 4 mm (3 mm for DC3) of a sense wire were corrected for this non-linearity by adjusting both t_0 and T. The resolution per plane for the three drift chambers is listed below.

Table 2.3 Drift Chamber Resolutions in Microns

Chamber	X	Y
1	340	350
2	400	300
3	250	225

2.12 Lead Glass Calibration

The lead glass was calibrated in a e+e- beam created by removing the uranium γ-filter and placing a thin lead foil in the secondary beam at the position of the Primakoff target. A small horizontal-field vernier magnet, MV, just downsteam of the target separated the charged leptons in y. The analyzing magnets, set at a reduced current of 800 amps, provided x separation. By varying the field of the vernier magnet and moving the glass array horizontally, the entire array could be illuminated with e+ or e- of various momenta. The pattern produced by forward going e+e- pairs looked like a Y in the horizontal plane with only one track before the analyzing magnets and two symmetric ones downstream. Therefore, the calibration sample was selected using the trigger configuration $\overline{S1}\cdot S2\cdot C2\cdot C6L\cdot C6R\cdot(S7+S7a)$. The $e^{\pm}$ energies and their projected positions in the glass were obtained by the standard track reconstruction.

Once energy and position are known, the calibration constants, c_i, which convert the digitized charge in each block i into the energy deposited, can be calculated. The constants were determined by a least squares method, minimizing the expression:

$$\sum_k (E_k - \sum_i c_i q_{ik})^2$$

where E_k = shower energy determined from spectrometer measurement for the kth event and q_{ik} = pulse height in the ith block for the kth event.

The energy resolution of the glass was determined by measuring the ratio of the $e^{\pm}$ energy as calculated from the calibration constants to that obtained from track reconstruction in bins of 2 GeV. A resolution of $\sigma(E)/E = 0.111/\sqrt{E} + 0.010$ (± 0.007) was obtained. The degree to which the data fit this functional form is evident in Fig 2.9. The spatial resolution was determined by comparing the position of the projected $e^{\pm}$ track in the glass to the shower center as determined from a weighted average of the energy deposited in the blocks. The average resolution over the whole array was found to be 1.5 cm. It was poorer (1.9 cm) near the central hole where transverse losses distorted the position, and better (0.9 cm) for completely contained showers.

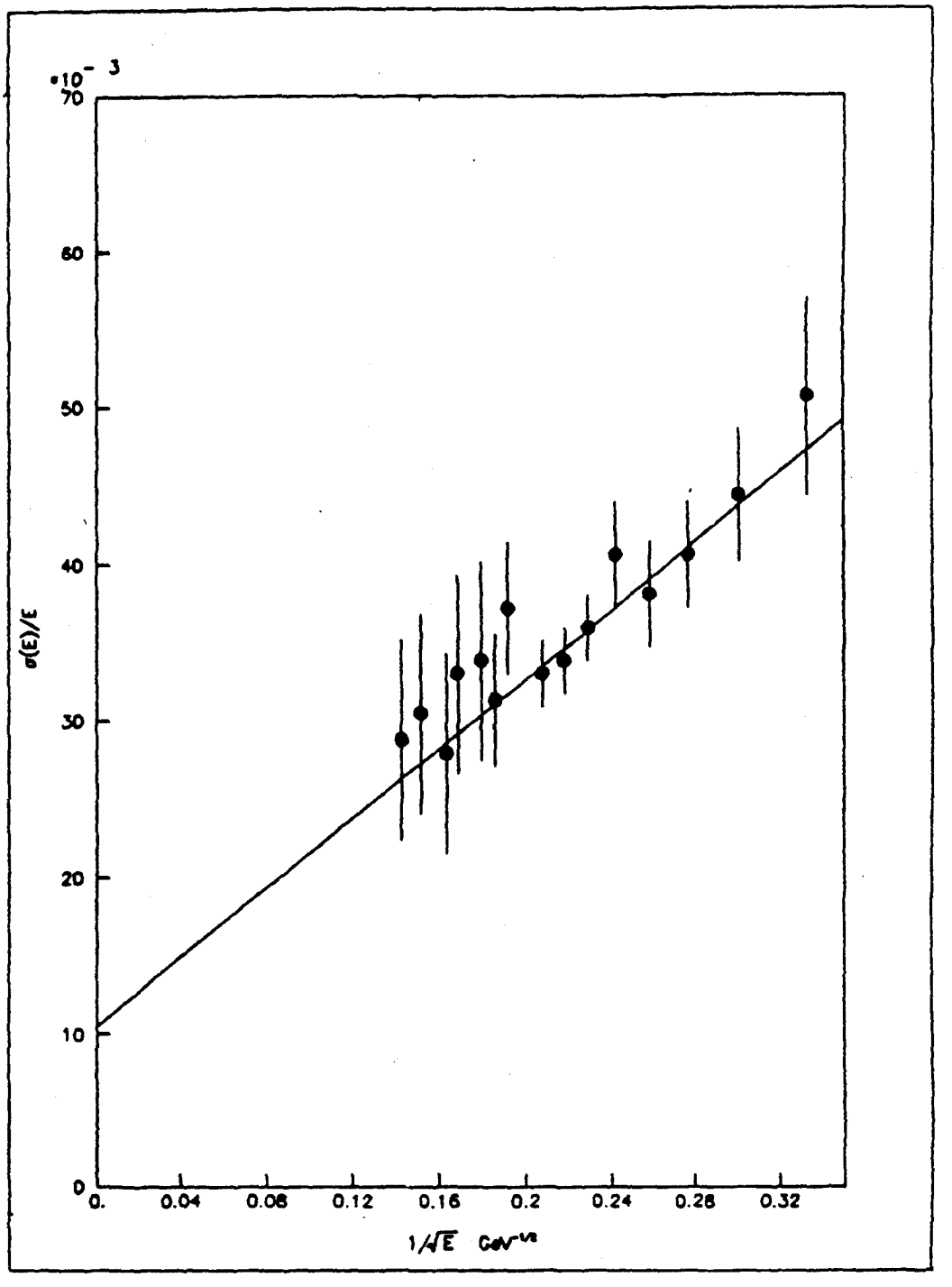

Figure 2.9 The lead glass energy calibration. All the points lie along a straight line which can be determined from a least squares fit to be: $\sigma(E)/E = 0.111/\sqrt{E}+0.010$

Since the signals from the phototube were summed and used in the data trigger, it was important that the gain of the different tubes be comparable. Therefore several preliminary calibration runs were taken merely for the purpose of balancing the glass and determining which magnet settings and glass positions provided the most uniform distribution of momentum. An initial set of five calibration quality tapes was then taken. They established the calibration constants present at the beginning of the experiment.

A second set of five tapes with three times the statistics and more uniform block coverage was obtained midway through the experiment. This set was used to determine the glass resolution and provided a better set of calibration contants. The five tapes corresponded to glass x-displacements of 0, ± 30, ± 60 cm. Each tape consisted of five MV currents of 0, ± 25, ± 50 amps with approximately 3500 $e^{\pm}$ events at each setting after cuts to eliminate hadron contamination. Changes in the calibration constants over the course of the experiment were monitored by comparing the second set of calibration constants to the first, and by the two methods discussed below.

Six neon flash lamps were triggered between spills. Fiber optic bundles distributed the light to the glass blocks and the phototube response was recorded. Tube or cable failure was easy to spot. The light pulser system was also useful in detecting any large scale drift in calibration due to such effects as temperature variation or radiation damage. Since six blocks were serviced by each pulser it was easy to distinguish between pulser fluctuations which affected all blocks in that group and a true calibration change.

A second check on changes in the calibration constants over time was performed using the reconstructed Ξ^0 events found on a regular data tape. A 'bootstrap' calibration analagous to the e^+e^- procedure was performed on those Ξ^0's which had two γ showers in the glass (2-γ Ξ^0's). The e^+e^- calibration constants provided a first guess at the energy per event, E_k. When the $\gamma\gamma$ invariant mass thus determined was forced to match the π^0 mass, the same least squares method yielded a new set of calibration constants.

The statistical fluctuations on the bootstrap calibration constants run-to-run was larger than those found in an e^+e^- tape because there were fewer 2-γ Ξ^0 events per tape. Since the constants obtained by the two methods were consistent, the more precise e^+e^- calibration was used in the analysis. In general, the bootstrap constants for any

particular tape varied no more than ±5% from the average over all runs. In the three cases where a block changed by more than this, the run or set of runs was tagged and the bootstrap calibration constant was used in place of the e+e- value.

CHAPTER 3

Analysis I: Event Reconstruction and Simulation

3.1 Introduction

The object of the event reconstruction analysis is to identify $\Sigma^\circ \rightarrow \Lambda\ \gamma$ candidates. First the raw data tapes were searched for $\Lambda \rightarrow p\ \pi^-$ events and preliminary cuts were applied to insure a pure Λ sample. Next the glass was examined for separated electromagnetic showers and hadron contamination was partially eliminated. Obvious 2-γ events were identified as Ξ°'s and comprised a separate data set used for bootstrap calibration and tuning the lead glass software routines. A number of cuts isolated the 1-γ events which became the final Σ° candidate sample. A Σ° was then reconstructed using the Λ information and the position and energy of the shower.

3.2 The Λ Reconstruction

The MWPC wire-hit data were searched for events which satisfied a neutral vee topology: two charged tracks originating from a vertex in the decay volume which are deflected through opposite angles after passing through the analyzing magnets (M2-M3). Raw wire hits from the MWPC's were fitted by the least-squares method, applied separately to the track segments upstream and downstream of M2-M3. The x and y-views were required to correlate with the u and v-views in the rotated chamber C3 and the additional U-plane in C4. The upstream and downstream x-view track segments were required to intersect at one bend point. The bend point was determined empirically as that point which minimized the geometrical χ^2, (χ^2_G), for most events. The empirical bend point was within 0.5 cm of that which can be calculated for two ideal dipoles with homogeneous fields over their effective lengths. A preliminary screening removed obviously unmanageable track topologies, such as events with >2 hits in >2 upstream or downstream chambers and events with <2 upstream or downstream track segments. Only events which passed the initial topological screening and also fit the two track hypothesis with a $\frac{\chi^2_G}{d.f.} < 3$ were retained.

The momentum and charge of the reconstructed tracks were determined from the bend angle in the analyzing magnets and compared with the decay hypotheses: $\Lambda \rightarrow p\ \pi^-$, $\bar{\Lambda} \rightarrow \bar{p}\ \pi^+$, and $K^\circ_S \rightarrow \pi^+\ \pi^-$. If the "reconstructed vee" was determined to have a mass within 15 MeV of the Λ mass, the event was retained as a "reconstructed Λ". The data which passed this cut contained a certain percentage of events which also fulfilled the K hypothesis ($|M_{vee} - M_K| < 25$MeV). These ambiguous events were retained since 30% of all true Λ's fall into this catagory. The resulting K°_S contamination is < 5% at this stage and it is further suppressed when the full Σ° reconstruction is performed.

The geometrical fitting procedure was iterated several times. The drift chambers and C1 were used after the first pass when including their hits in the track did not increase χ^2 by more than the number of added degrees of freedom. Corrections were made in the downstream tracks for the second magnet's 7.5 mrad rotation. The bend point was also modified for second-order corrections as a function of entering angle and momentum. The magnitude of the field integral was adjusted on a tape-to-tape basis to give the proper Λ mass.

The program had a reconstruction efficiency of 80% for Λ Monte Carlo events which included the effects of multiple scattering and chamber inefficiencies. For data tapes taken

with a positive sweeper magnet current of +3300 amps, 40% of the Σ^0 triggers and 65% of the Λ and Λ' triggers yielded reconstructed vees. When the sweeper current was switched to -3300 amps, the yield for Σ^0 triggers dropped slightly to 30% whereas the yield for Λ and Λ' triggers plummeted to 20-30% with great variation run to run. Approximately 92% of the reconstructed vees were identified as Λ's.

The reconstructed Λ's were then passed to the second stage of the Λ analysis. A χ^2 function was constructed which included the charged track momenta from the previous reconstruction procedure. The momenta were allowed to vary within their uncertainties with the constraint that the calculated parent mass be equal to the Λ mass. The difference between the resulting kinematic χ^2_K and the first pass χ^2_G, $\Delta\chi^2=\chi^2_K - \chi^2_G$, is shown in Fig 3.1. It was used to eliminate poorly reconstructed Λ's by cutting out all events with $\Delta\chi^2 > 21$. Such selected Λ's were generally 89% of the reconstructed Λ's. Fig 3.2 displays the χ^2_G per degree of freedom for selected Λ's from both the prescaled Λ triggers and Λ Monte Carlo.

Two other cuts were also made at this stage. The z-position of the Λ decay vertex was required to be within the decay volume and the proton and π^- tracks were required to miss the lead glass array. These cuts and the ones

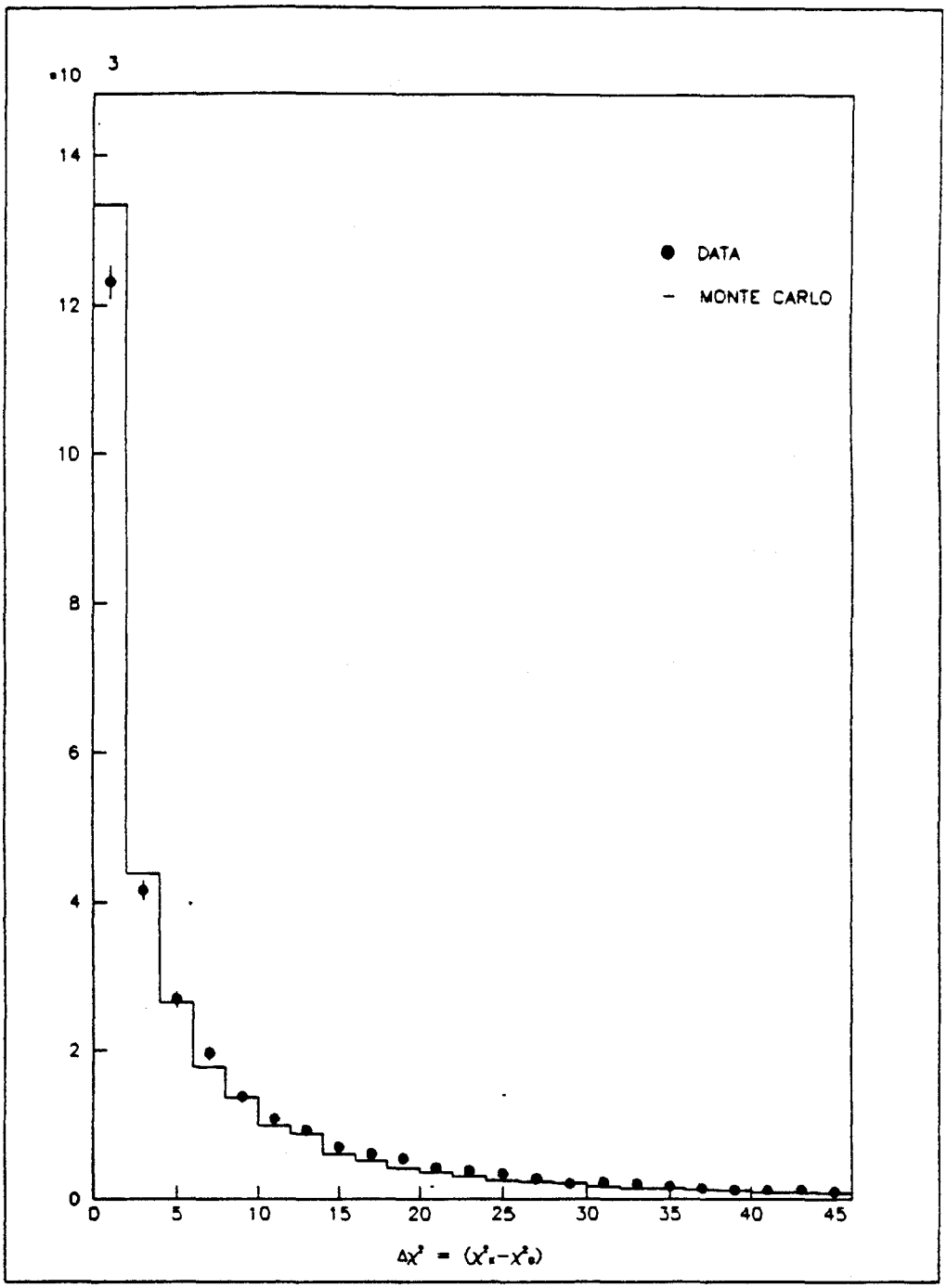

Figure 3.1 The difference between the final pass kinematic fit χ^2 and the initial geometric χ^2. The arrow indicates the upper limit of acceptable events in the final data sample.

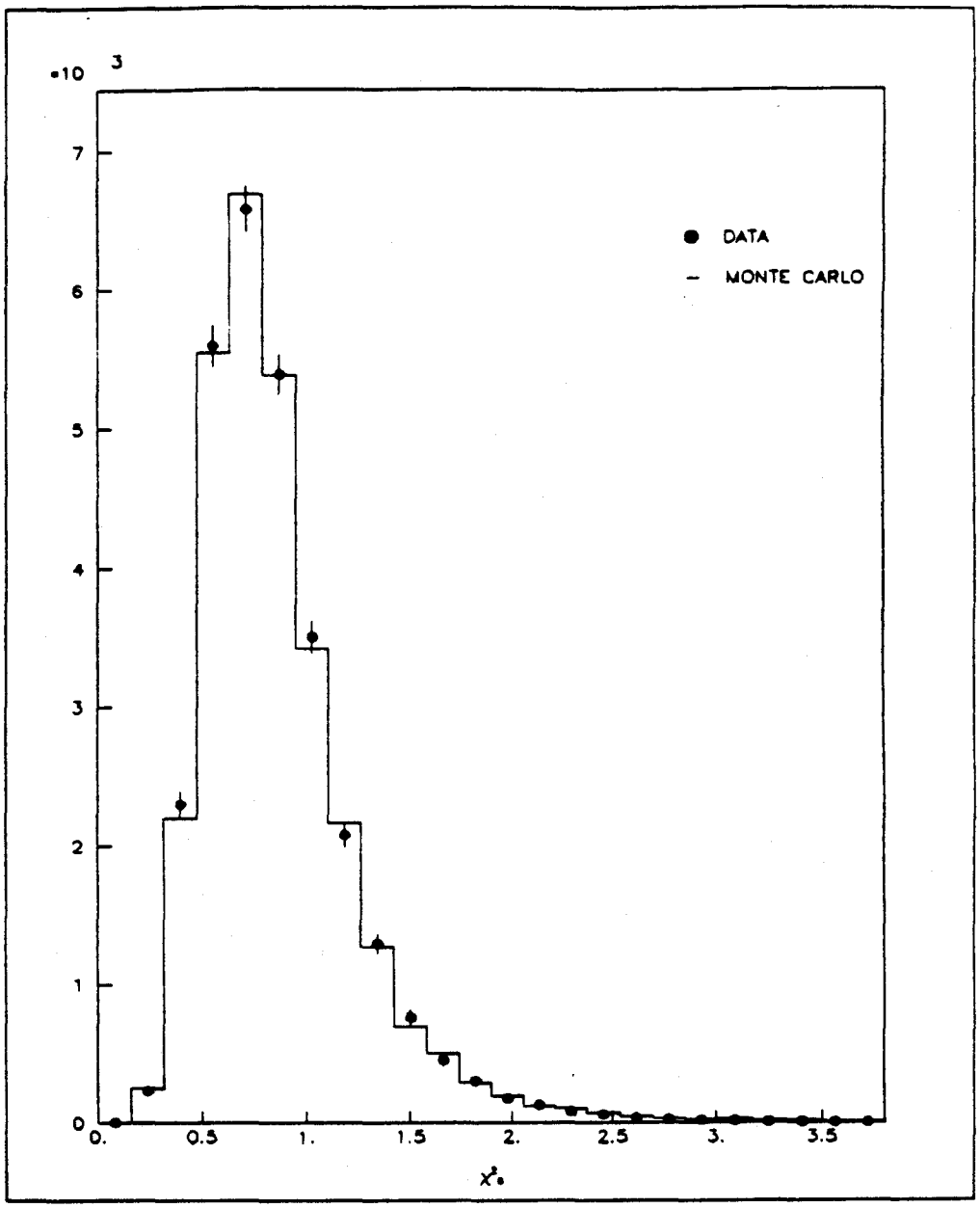

Figure 3.2 The geometric χ^2 per degree of freedom from prescaled Λ' triggers after all "Λ" cuts, including $\Delta\chi^2 < 21$.

described previously were applied to all the data independent of trigger. Their effect on both data and Monte Carlo is summarized in Table 3.1 under the heading "Λ cuts". The Λ decay vertex and Λ mass after all Λ cuts are shown in Figs 3.3 and 3.4.

3.3 The Σ° Reconstruction

The final ingredients needed to reconstruct the Σ° are the energy and position of the γ. These quantities were determined from the lead glass information. First the TDC information was used to eliminate any blocks found to be out of time with the charged track event. Next the energy deposited in each block was found by multiplying the pulse height in the ADC's by the calibration constants obtained in the manner described earlier. The main array block with the highest energy and its nearest neighbors comprised the main array cluster. The γ position was found by performing a weighted average of these cluster blocks. This center position was projected to the front wall and a front wall cluster was defined by all non-zero nearest neighbors. The sum of cluster energies in the front wall and main array gave the energy of the photon. The weighted average of the front wall blocks provided a slight correction to the γ x-position found by the main array alone.

Table 3.1

Summary of Software Cuts

	Fraction of Events left after Cuts			
	$\Sigma^{\circ}{}_{Pk}$M.C.	$\Lambda\gamma_{acc}$M.C.	Ξ°M.C.	Data
Λ Cuts:				
reconstructed vees	0.79	0.79	0.77	normalized
Λ mass within 15 Mev $p\ \pi^-$ vertex in decay vol. no $p\ \pi^-$ in glass	0.78	0.78	0.76	0.73
$\Delta\chi^2 < 21$	0.70	0.69	0.68	0.59
Σ° Cuts:				
no γ in S3-S6	0.70	0.61	0.54	0.53
$E_{FW} > 1$ GeV $E_{MA} > 5$ GeV $(E_{FW}+E_{MA}) < 50$ GeV	0.56	0.22	0.41	0.20
ESUM > 2 GeV	0.56	0.13	0.26	0.11
fiducial glass cut	0.35	0.08	0.18	0.07
Further Kinematic Cuts:				
$r^2_{prod}(\Lambda) > 5$ mm^2	0.32	0.03	0.18	0.06
$0.001 < p_t{}^2(\Sigma\Lambda) < 0.008$	0.32	0.02	0.07	0.03
ECUT	0.32	0.02	0.06	0.02
$Q^2 < 0.002$	0.23	0.003	0.01	0.004

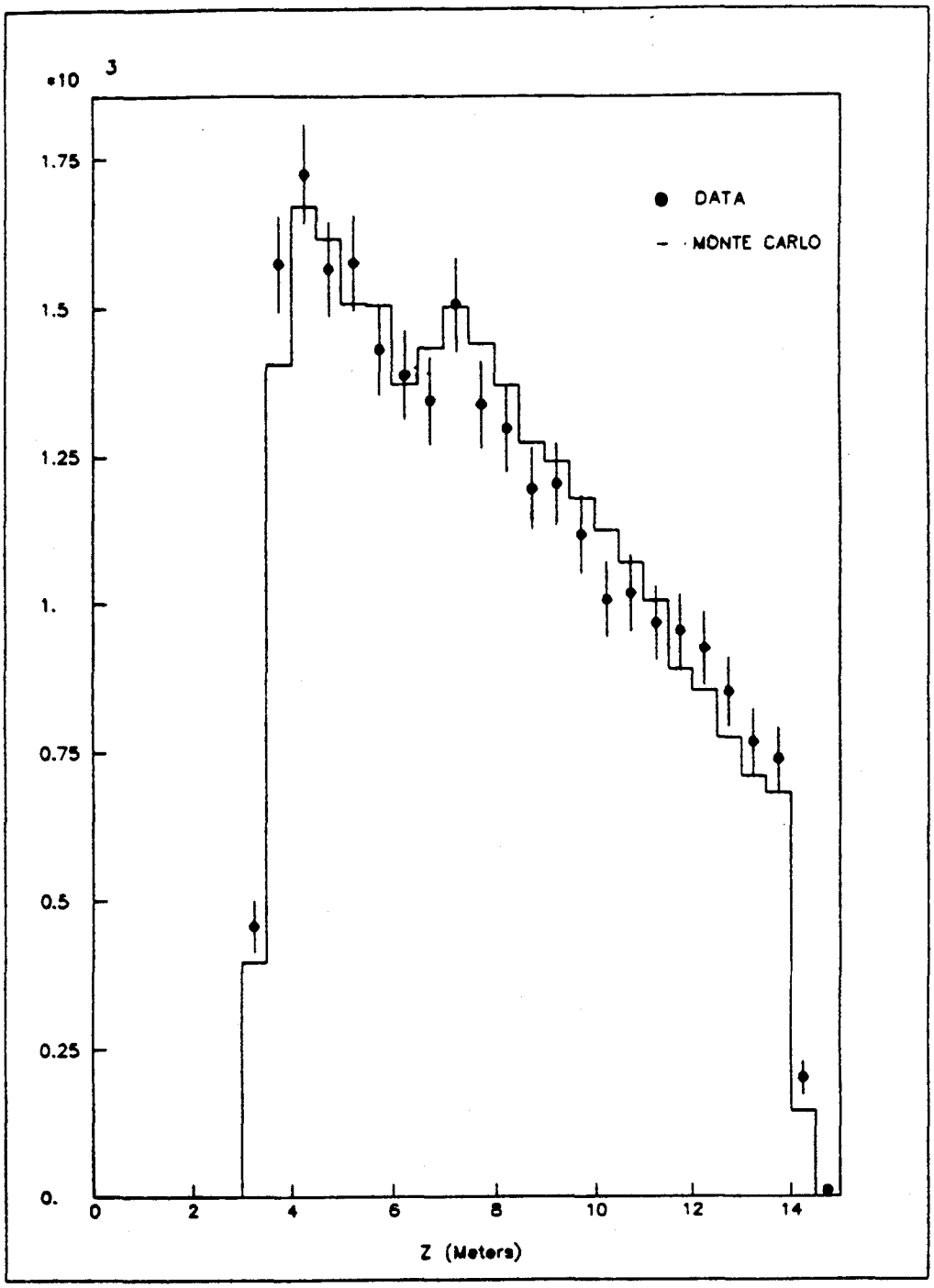

Figure 3.3 The z-position of the Λ decay vertex after all Λ cuts.

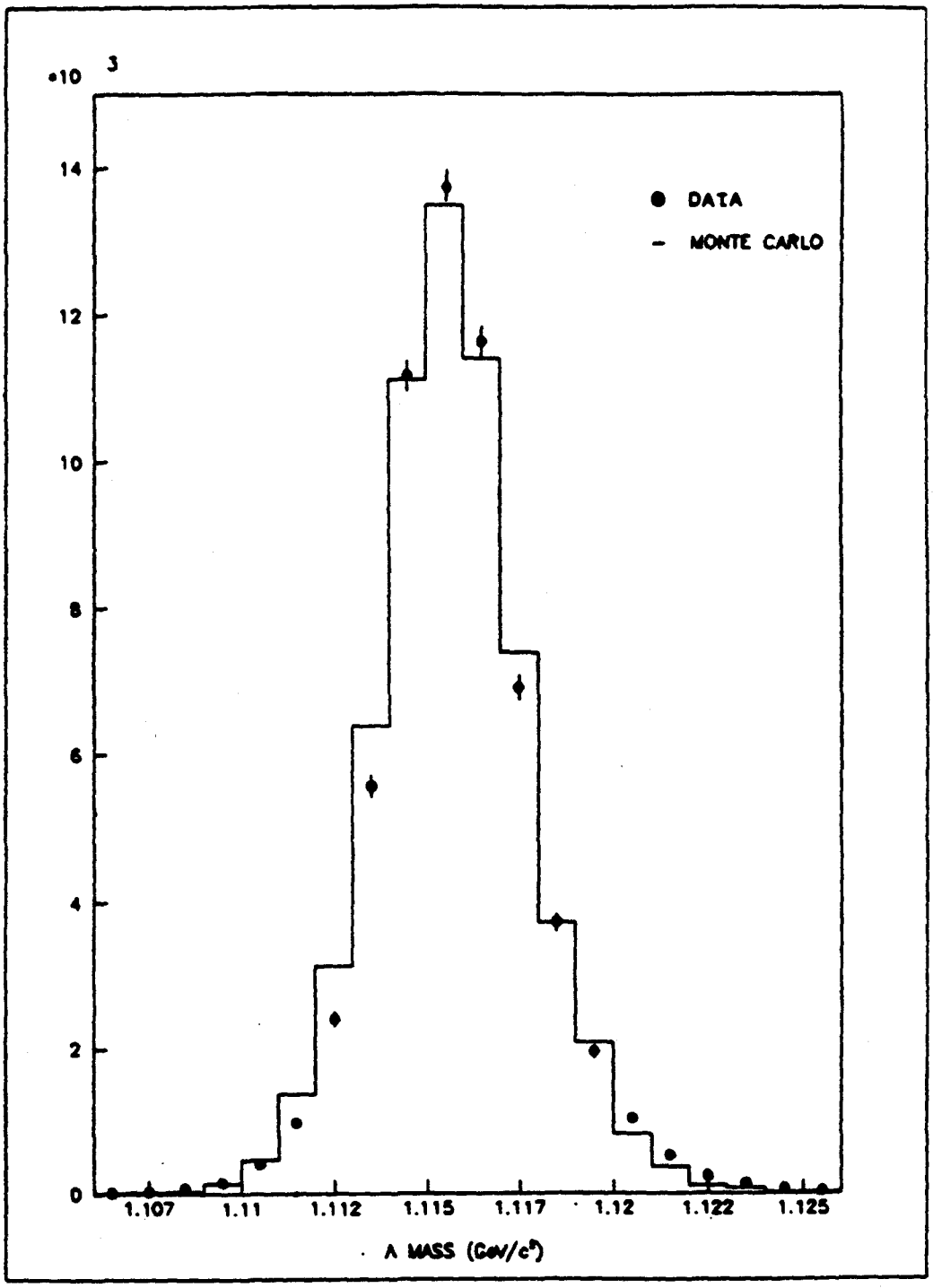

Figure 3.4 The $p\pi^-$ invariant mass distribution from prescaled Λ' triggers after all "Λ" cuts. The width of the distribution is 2.1 MeV (st. dev.).

The energy in all non-cluster blocks in both the front wall and main array was also summed. The event was rejected if this sum exceeded 2 GeV. This effectively removed 2-γ events from the sample without eliminating 1-γ events with a few noisy blocks. This cut also removed events where the cluster spread over more than its nearest neighbors since these clusters were usually hadronic showers. Although these hadronic showers were generally much higher energy, they were not eliminated by later energy cuts because they often happened near the edge of the hole, thus losing much of their energy, but not their spread. Fig 3.5 displays the non-cluster energy (ESUM) for the data and a Ξ^0 Monte Carlo.

Three more cuts ensured the success of this simple one-cluster algorithm. The elimination of events where the projected track of the p or π^- intersected the glass array has already been included under Λ cuts, but deserves mention since it removed the most obvious source of hadron contamination. Secondly, if the center of any cluster was within 5.2 cm of the hole or outside the fiducial edge of the array, it was also rejected. See Fig 2.7 for the dimensions of the fiducial volume. Finally, clusters were required to have at least 1 GeV deposited in the front wall and 5 GeV in the main array, but not more than 50 GeV in all. The cluster energy after all cuts peaked at 10 GeV. The shape of the

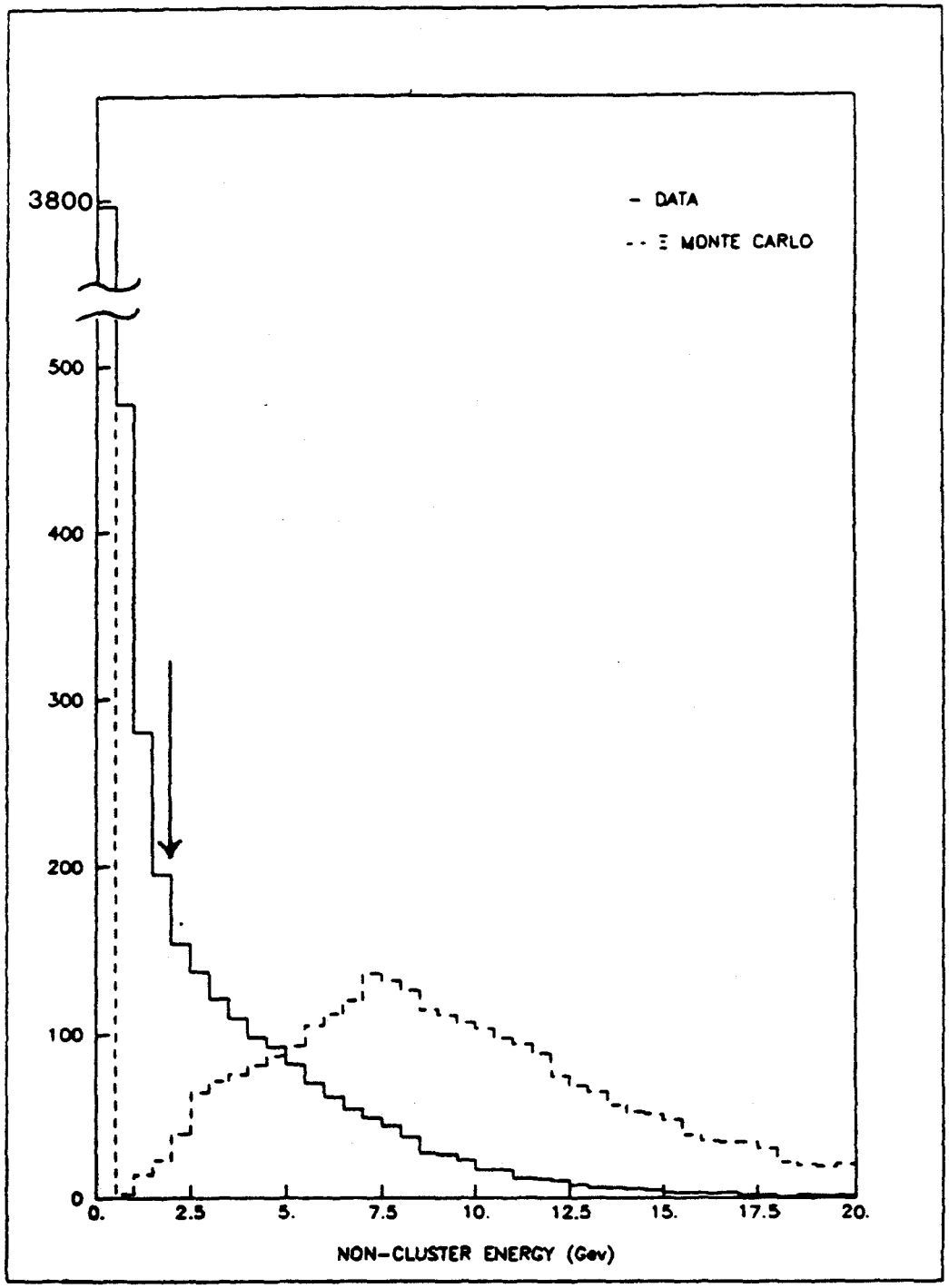

Figure 3.5 The sum of the energy in all non-cluster blocks. The Ξ^0 Monte Carlo shows a broad peak corresponding to the second γ of the π^0 decay. The tail of the data distribution is composed of this element plus contributions from noisy blocks and hadron contamination. Events with non-cluster energy greater than 2 Gev (see arrow) were rejected.

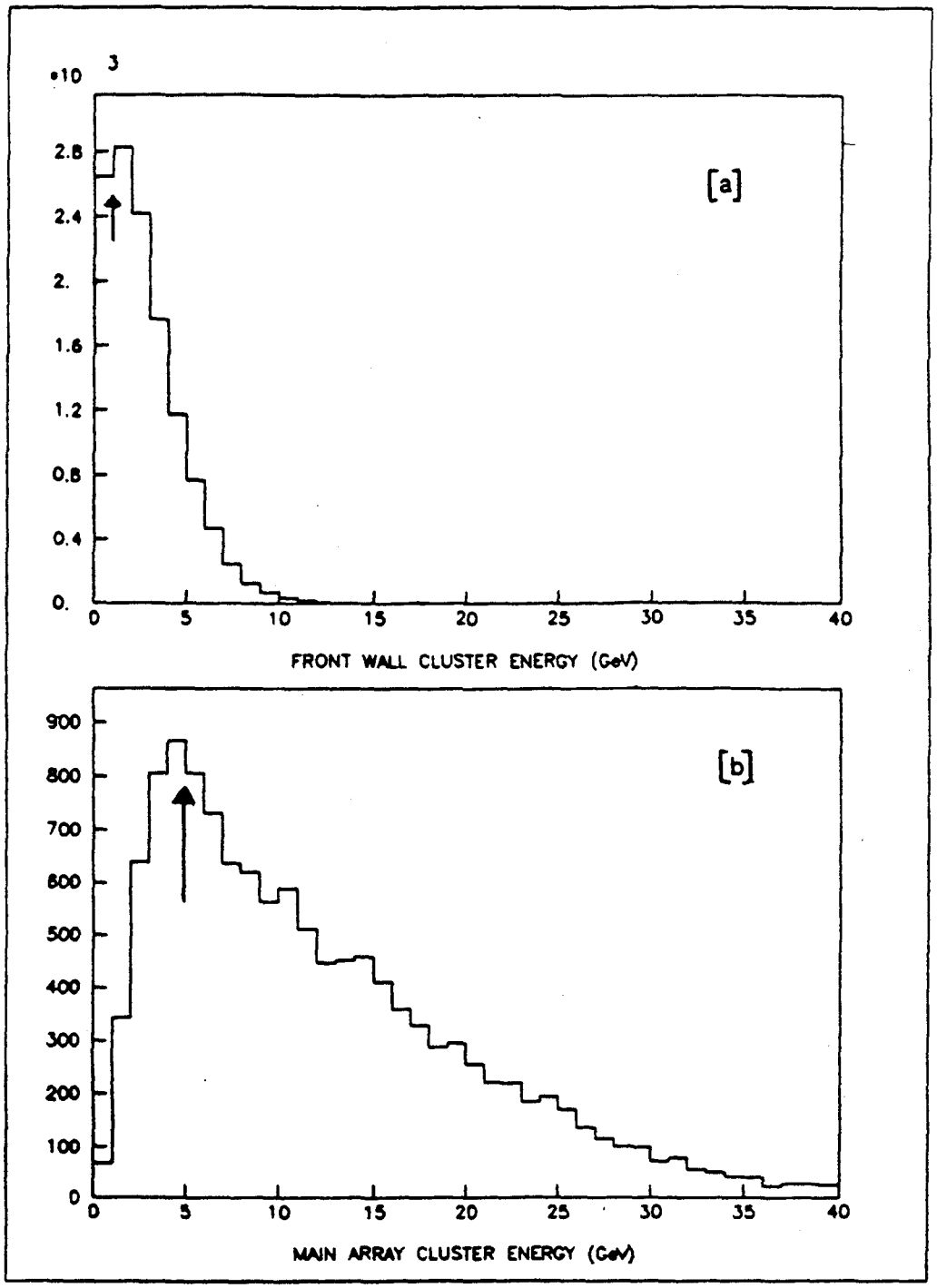

Figure 3.6 The energy distribution of a shower detected by the front wall (a) and main array (b). The arrows indicate the lower bound of acceptable energies.

front wall and main array energy distributions for such 1-γ showers can be found in Fig 3.6.

Although events with 2 γ's in the glass have now been eliminated, a certain fraction of the Ξ° background had only one γ which hit the glass. If the second γ can be observed in the auxilliary detector, the number of events in this catagory can be reduced. Latches from S3-S4 and S5-S6, the scintillator sandwiches mounted on the upstream face of M2, were noted for each event. If either sandwich showed a typical photon conversion signal $\bar{A}\cdot B$, the event was rejected. This cut plus the glass clean-up cuts mentioned above are summarized in Table 3.1 under the heading "Σ° cuts".

The energy and position of the γ was then combined with the charged track information to reconstruct the Σ°. The Λ decay vertex and momentum vector having been already determined by the charged track reconstruction, the trajectory was projected upstream to the plane of the Primakoff target. The x-y coordinates of its intersection with that plane constituted the Σ° vertex. The line connecting the Σ° vertex with the position of the γ detected in the glass was the γ trajectory. Together with the γ energy, they determined the parent momentum and $\Lambda\gamma$ invariant mass for the Σ° hypothesis.

3.4 Data Consistency

Changing conditions in the beam and trigger electronics caused fluctuations as large as 50% in on-line rate ratios such as Λ/SEM and Σ^0/Λ. The effect on the Λ yield caused by switching the sweeper polarity has already been mentioned. The corresponding effect on the ratio of Σ^0/Λ triggers was a dramatic reduction from .012 to .006. Polarity tests several days later confirmed that switching the M1 current was solely responsible. Happily, the change in M1 polarity had no effect on the Σ^0/Λ ratio for reconstructed vees, since it was compensated by the change in Λ yield, i.e.

$$\frac{\text{(No. of reconstructed } \Lambda\text{'s in } \Sigma^0 \text{ trigger)}}{\text{(No. of reconstructed } \Lambda\text{'s in } \Lambda \text{ trigger)}} \times (\Sigma^0/\Lambda \text{ trigger ratio})$$

remained constant. Changes in the front wall trigger threshold caused by linear adder and amplifier drift, and changes in amplifier configuration also affected the number of Σ^0/Λ triggers observed on-line. The 1 GeV cut in the front wall was especially helpful in reducing these discrepancies.

Table 3.2 illustrates how the Σ^0/Λ ratios became much more uniform tape-to-tape once the data was reconstructed and the glass cuts were applied. The typical statistical errors are quoted above each column. Comparisons of the Σ^0/Λ ratios between tapes gives an idea of the internal consistency of

Table 3.2

Data Consistency

(No. of Events in Σ Trigger)/(No. of Events in Λ Trigger)

Tape No.	Scalar Record (±0.00005)	Reconstructed Vees (±0.0001)	After Glass Cuts (±0.003)
TARGET 1			
2291	0.012	0.009	0.034
2333	0.014	0.012	0.034
2334	0.013	0.010	0.034
2363	0.006	0.007	0.030
2373	0.008	0.010	0.025
2395	0.007	0.010	0.034
TARGET 2			
2271	0.025	0.021	0.026
2280	0.013	0.009	0.019
2298	0.013	0.010	0.021
2329	0.013	0.010	0.034
2368	0.007	0.007	0.027
TARGET 3			
2292	0.014	0.009	0.031
2311	0.017	0.013	0.028
2325	0.012	0.010	0.025
2350	0.011	0.010	0.031
2364	0.008	0.007	0.022
2383	0.008	0.010	0.034
TARGET 4			
2272	0.026	0.022	0.030
2274	0.028	0.021	0.032
2288	0.013	0.009	0.030
2293	0.013	0.009	0.025
2299	0.013	0.010	0.029
2303	0.013	0.010	0.024
2306	0.010	0.008	0.019 (removed)
2318	0.017	0.013	0.031
2326	0.013	0.012	0.029
2330	0.012	0.009	0.032
2335	0.013	0.010	0.031
2339	0.013	0.009	0.027
2358	0.010	0.009	0.021
2365	0.006	0.006	0.021
2369	0.008	0.006	0.026
2374	0.069	0.009	0.038
2378	0.007	0.010	0.031
2391	0.007	0.009	0.032

Table 3.2 cont.

TARGET 5			
2273	0.026	0.022	0.029
2275	0.011	0.006	0.025
2277	0.012	0.008	0.021
2281, 2282	0.012	0.009	0.027
2284	0.012	0.009	0.023
2289	0.012	0.008	0.029
2294	0.013	0.009	0.022
2300, 2301	0.013	0.009	0.027
2304	0.013	0.010	0.023
2307	0.011	0.008	0.020
2308	0.011	0.009	0.026
2312	0.016	0.012	0.029
2314	0.017	0.013	0.038
2319	0.015	0.012	0.028
2327	0.011	0.010	0.020
2331	0.012	0.009	0.030
2336	0.013	0.010	0.033
2340	0.013	0.010	0.033
2351	0.006	0.009	0.028
2353	0.010	0.009	0.031
2359	0.008	0.008	0.030
2366	0.006	0.007	0.027
2372	0.009	0.009	0.036
2375, 2376	0.007	0.010	0.031
2379	0.007	0.011	0.030
2385	0.009	0.010	0.031
2387	0.050	0.009	0.030
2392	0.007	0.010	0.030
TARGET 6			
2278	0.012	0.008	0.024
2285	0.012	0.009	0.026
2309	0.013	0.010	0.030
2315	0.017	0.014	0.030
2341	0.013	0.010	0.023
2354	0.009	0.010	0.031
2381	0.007	0.011	0.031
2388	0.007	0.010	0.033

Table 3.2 cont.

TARGET 7			
2279	0.012	0.009	0.029
2283	0.012	0.009	0.030
2286	0.013	0.009	0.027
2287	0.012	0.009	0.026
2290	0.012	0.008	0.022
2295, 2296	0.013	0.009	0.024
2302	0.013	0.009	0.024
2305	0.013	0.009	0.022
2310	0.013	0.009	0.035
2313	0.016	0.013	0.030
2316	0.017	0.013	0.027
2317	0.016	0.012	0.029
2320	0.016	0.012	0.026
2328	0.010	0.008	0.020
2332	0.014	0.010	0.024
2338	0.013	0.009	0.025
2342	0.013	0.009	0.016
2349	0.006	0.010	0.029
2352	0.007	0.009	0.025
2355	0.009	0.009	0.025
2357	0.006	0.009	0.024
2360	0.007	0.009	0.026
2361	0.007	0.008	0.015
2362	0.007	0.007	0.021
2367	0.006	0.006	0.028
2377	0.008	0.010	0.037
2382	0.008	0.009	0.028
2386	0.007	0.009	0.034
2389	0.007	0.009	0.029
2390	0.008	0.009	0.030
2393	0.004	0.006	0.021 (removed)
2394	0.007	0.008	0.016 (removed)

each target sample. The distribution of tapes with ratios from 1 - 3 σ away from the norm follows Gaussian statistics. Three tapes, FE2306, FE2393, and FE2394, were removed from the sample: the first because of beam focussing problems in the accelerator, and the others because of glass trigger anomalies noted on-line as well as off.

3.5 Monte Carlo Data Simulation

3.5.1 Event Generation

It is important to understand the acceptance of the apparatus and the effect of software cuts on particle yields and kinematic variables. A Monte Carlo simulation of the experiment accomplishes these goals. Neutral strange particles were generated at the production target with the appropriate momentum spectrum. Although the empirical formulae for the Λ and Ξ^0 differential cross sections derived from previous neutral hyperon studies[9] did a good job of matching the observed spectra, the final version of the Monte Carlo used a spectrum adjusted to match the data presented here.

The particles were then propagated through the collimator. The charged tracks of their decay products, including kinks from π^- decay, produced hits in the MWPC's, drift chambers, and counters with the appropriate efficiencies. The processes of most interest were $\Lambda \rightarrow p\,\pi^-$ from non-interacting beam Λ's (Λ_B Monte Carlo), $\Xi^\circ \rightarrow \Lambda\,\pi^\circ$ (Ξ° Monte Carlo), and $Z+\Lambda \rightarrow \Sigma^\circ \rightarrow \Lambda\,\gamma$ ($\Sigma^\circ{}_{Pk}$ Monte Carlo). Variations on the three mentioned above provided insight into background from strongly produced Σ°'s ($\Sigma^\circ{}_{str}$ Monte Carlo) and beam Λ's plus an accidental γ ($\Lambda_B+\gamma_{acc}$ Monte Carlo).

Multiple Coulomb scattering was introduced at all counters, chamber and decay windows, air volumes, helium bags, and lead converter. The probability of scattering from each chamber wire plane was calculated from its wire spacing and applied discretely. The angular distribution of multiple scattering is only approximately Gaussian with single large angle scatters giving rise to long non-Gaussian tails. Therefore, the scattering angle was chosen from a distribution of normalized scattering angles θ/θ_{rms}, obtained from the tables of Marion and Zimmerman[13]. The distribution was then scaled for each scattering element by $\theta_{\frac{1}{e}}$, the angle at which the scattering probability has dropped by e. This angle is given by Highland[14] as

$$\theta_{\frac{1}{e}} = \frac{0.017}{p}(\mathrm{GeV/c})\,\sqrt{X}\,\left(1+\frac{1}{8}\log_{10}(10X)\right)$$

where X is the thickness of the material in radiation lengths and p is the incident momentum. In the Gaussian approximation, $\theta_{\frac{1}{e}} = \theta_{rms}$. In thin scattering elements only the direction cosines were changed. In thick elements of length L, the new track was also displaced $\Delta x=\theta(x)_{\frac{1}{e}} L/\sqrt{3}$, $\Delta y=\theta(y)_{\frac{1}{e}} L/\sqrt{3}$, $\Delta z=L$ from the point of entrance. Including multiple scattering increased the standard deviation of the Monte Carlo Λ mass from 1.2 MeV to 2.2 MeV as compared to the experimental value of 2.1 MeV.

3.5.2 Charged Track Resolution

It is important that the track resolution of Monte Carlo generated hits match that of the data. Chamber efficiencies can play a crucial role in determining the momentum resolution. Most of the MWPC's were close to 100% efficient, so slight differences over time and any position dependence did not affect the resolution much. C1, on the other hand, was in the process of being tested during the run. Thus it was run at various voltages, not all of which were optimum. Its average efficiency over all runs was found to be 92%. Since C1 was a high resolution chamber with a large lever arm, it was capable of improving the track resolution by a factor of 2. A histogram of the uncertainty in the angle

between the reconstructed Λ and the beam shows a two peak structure (Fig 3.7). The lower peak is composed of those Λ's which decayed upstream of C1, thus employing the full power of its better resolution. This histogram is a sensitive measure of C1 efficiency, since any inefficiency in C1 will shift events from the first peak to the second.

The drift chambers were also resposible for improving the momentum resolution. Fits which use at least two of the three chambers populate the low mrad region of the broad second peak. Effective drift chamber efficiencies per plane per track were in general quite low. This is because other effects besides normal wire inefficiencies had to be folded in. The first effect was due to nature of the TDC trigger. If both charged tracks went through the same or adjacent drift cells, the TDC was reset for one or both wires. Secondly, the event was rejected if the χ^2 per degree of freedom on a fit including the drift chamber hit was larger by 3 σ than the χ^2 of the track without it. Thirdly, a certain amount of chamber data was irretrievably lost: (a) the TDC event offset problem (see Appendix A) prevented records from beng written to tape and (b) due to wire breakage and general maintanence problems, we often ran with only one or two operative drift chambers.

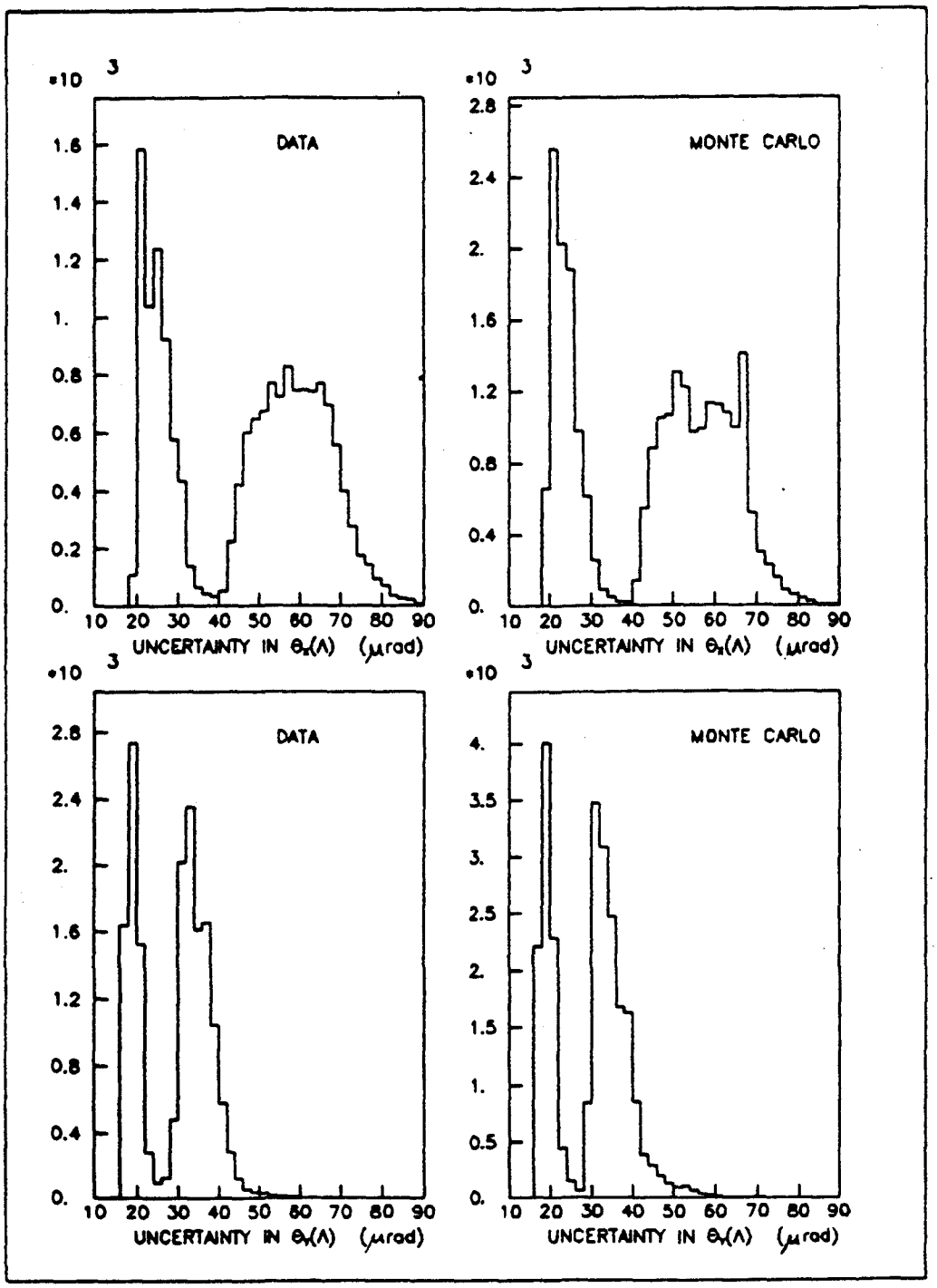

Figure 3.7 The uncertainty in the angle of the reconstructed Λ to the beam centroid for both x and y projections.

The first effect is well understood and was put into the Monte Carlo explicitly. An efficiency based only on the second condition was obtained by comparing the Ξ^0 Monte Carlo to only that Ξ^0 data which already had drift chamber information. To avoid double counting the TDC data loss in the efficiency calculation, only tracks two or more cells apart were used in the calculation. This is labeled efficiency I in Table 3.3 and is a measure of the number of wrong event offset correlations made by the TDC matching algorithm. As can be seen from these efficiencies, the wider π^- tracks were generally identified more accurately than the proton tracks.

A second efficiency was defined as whatever additional efficiency was needed by the Monte Carlo to match the number of drift chamber hits finally used in the track fit. Labeled efficiency II in the table, it contains the effects of data loss through offset shifts and inoperative drift chambers. Here DC2, which was most often pulled from the beam for repairs, has a lower effective efficiency than the other chambers.

The overall agreement in resolution between Monte Carlo and data can be seen by comparing the angle error plots generated by the Monte Carlo (Fig 3.7) with those previously shown for the data.

Table 3.3

Drift Chamber Efficiency

EFFICIENCY I (per track per plane)

Drift Chamber	Proton x1	Proton x2	Proton y1	Proton y2	Pion x1	Pion x2	Pion y1	Pion y2
1	0.50	0.49	0.63	0.63	0.70	0.64	0.73	0.74
2	0.80	0.78	0.85	0.83	0.79	0.82	0.82	0.53
3	0.61	0.60	0.85	0.84	0.79	0.79	0.87	0.86

EFFICIENCY II (per track per coordinate)

Drift Chamber	Proton x	Proton y	Pion x	Pion y
1	0.73	0.67	0.74	0.65
2	0.57	0.52	0.52	0.57
3	0.77	0.68	0.66	0.64

3.5.3 Glass Simulation

Since kinematic variables such as the Σ^0 momentum and the invariant mass are very sensitive to γ position and energy, much effort went into simulating the glass properly in the Monte Carlo. First the energy of the incoming photon was partially randomized by a Gaussian distribution with a σ equal to the experimental glass resolution determined in Section 2.12. In discussions of Monte Carlo events, the energy refers to this partially randomized variable.

In order to understand how to split the energy between the front wall and main array, the e+e- calibration tapes were examined. Since the incident particles' energy and position were known, the ratio of front wall to total energy was plotted as a function of incident energy. This ratio and its width (which is a measure of fluctuations in the longitudinal energy deposition) are shown in Fig 3.8. The behavior of these variables can be approximately described by the polynomials below

$$\frac{E_{FW}}{(E_{FW}+E_{MA})} = \begin{cases} 0.18 & p(e^{\pm}) > 39 \text{ GeV/c} \\ 0.331-(0.0039)p(e^{\pm}) & p(e^{\pm}) < 39 \text{ GeV/c} \end{cases} \tag{3.1}$$

$$\sigma\left(\frac{E_{FW}}{E_{FW}+E_{MA}}\right) = \begin{cases} 0.06 & p(e^{\pm}) > 39 \text{ GeV/c} \\ 0.125-(0.0017)p(e^{\pm}) & p(e^{\pm}) < 39 \text{ GeV/c} \end{cases} \tag{3.2}$$

for an incoming electron or positron.

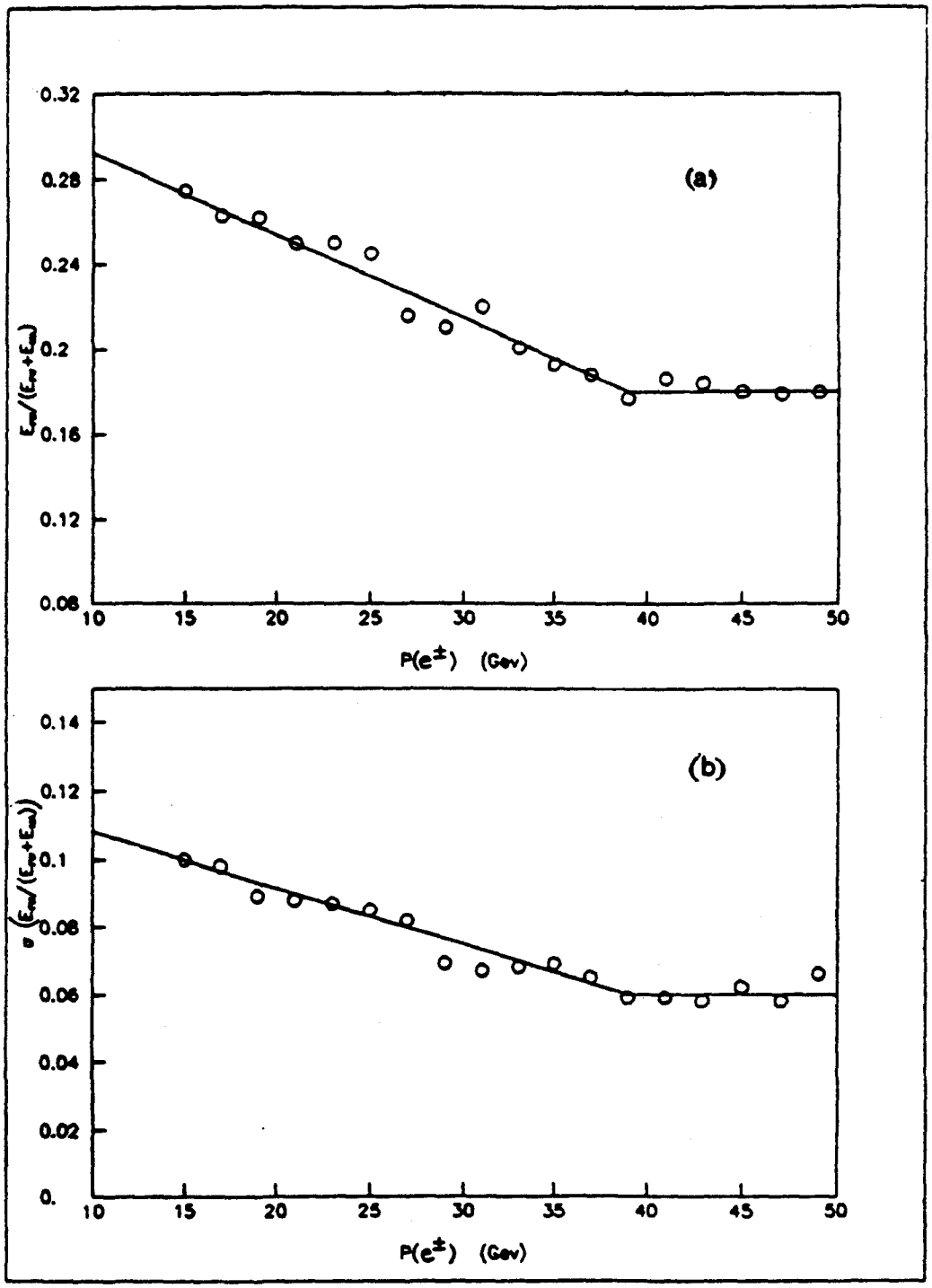

Figure 3.8 The fraction of detected energy deposited in the front wall (a) and the standard deviation of this fraction (b) as a function of incident electron energy.

An incident photon, however, tends to shower later than an electron, and therefore has a smaller energy ratio. In order to understand such detailed questions, a Monte Carlo program called EGS (Electron-Gamma Shower)[11] was used. Once the incident particle type, position, and momentum was defined, the program traced each of the subsequent shower particles through a user-specified material and geometry until one of three things happened: another interaction occurred, the particle energy fell below threshold (1.5 MeV for charged particles and 1 Kev for photons), or it entered a region of space where the user requested it be discarded. The EGS Monte Carlo was run with the counter and glass configuration used in this experiment for both electron and photon cases. The difference in $E_{FW}/(E_{FW}+E_{MA})$ between the electron and γ cases was well described by a conversion factor of $\gamma/e = 0.7019+(0.0047)p(e^{\pm})$. The corresponding factor for the width was $\gamma/e = 1.4$. Multiplying equations 3.1 and 3.2 by their respective conversion factors gave the percentage of energy deposited in the front wall with the appropriate fluctuations.

Next the lateral spread of the shower was modeled. Ninety percent of the energy was contained in a Gaussian with σ=2.85 cm, representing the core of the shower, and the remaining 10% in a Gaussian σ=13 cm wide to account for the long tails. The front wall was split 93% to 7% between two

Gaussians of σ=0.85 cm and σ=20 cm. The splits and standard deviations were obtained by matching Monte Carlo and data distributions of the number of blocks assigned to the main array cluster and to the front wall cluster. Multiple solutions were eliminated by matching energy loss and position shift of clusters near the central hole.

In the data analysis program and the e^+e^- calibration program, a software threshold of 20 counts per block (0.5 MeV typically) was imposed to reduce noise. The calibration constants thus compensated for this energy loss in the data, but not in the Monte Carlo. The energy loss from this threshold cut was determined for three cluster center types: A) interior blocks, B) blocks exposed on one side, and C) blocks exposed on several edges. Three average correction factors were thus obtained. The correction factors were not calculated event by event since the calibration constants used with real data are also averages over many events with different cluster types. Just before submission to the analysis, the pulse heights from a Monte Carlo cluster of type A, B, or C were multiplied by their respective correction factors.

Since a pure sample of Primakoff Σ^0's could not be extracted from the data, all comparisons were made between the Ξ^0 Monte Carlo and the 1-γ Ξ^0s in the data. For the

purposes of these comparisons, the 1-γ Ξ^0 sample was defined as non-target-pointing Λ's with a clean γ in the glass. However, a peak from strongly produced Σ^0's can be observed in the $\Lambda\gamma$ invariant mass for $Q^2 > 0.1$ where the background is greatly reduced. Because of the narrowness of the Σ^0 peak, FWHM=10 MeV, it has greater sensitivity to the overall glass calibration than any other variable. The Σ^0 mass peak in the data is 2 MeV higher than the known mass value, a shift that can be completely corrected for by multiplying the calibration constants by 0.97. Such a slight shift is well within the uncertainties associated with glass calibration by either the e+e- or bootstrap method and does not change the broader (FWHM=25 MeV) π^0 mass from $\Xi^0 \rightarrow \Lambda\pi^0$ significantly. It is also of the same order as the difference between electron and photon longitudinal leakage out the back of the array.

3.5.4 Acceptance

The acceptance of the spectrometer was determined by generating the Monte Carlo events at the production target with a flat momentum spectrum and passing them through the apparatus using the techniques described above. In Figs 3.9-3.11 the acceptance for Λ's, Σ^0's, and Ξ^0s are plotted as functions of momentum. The upper curves are

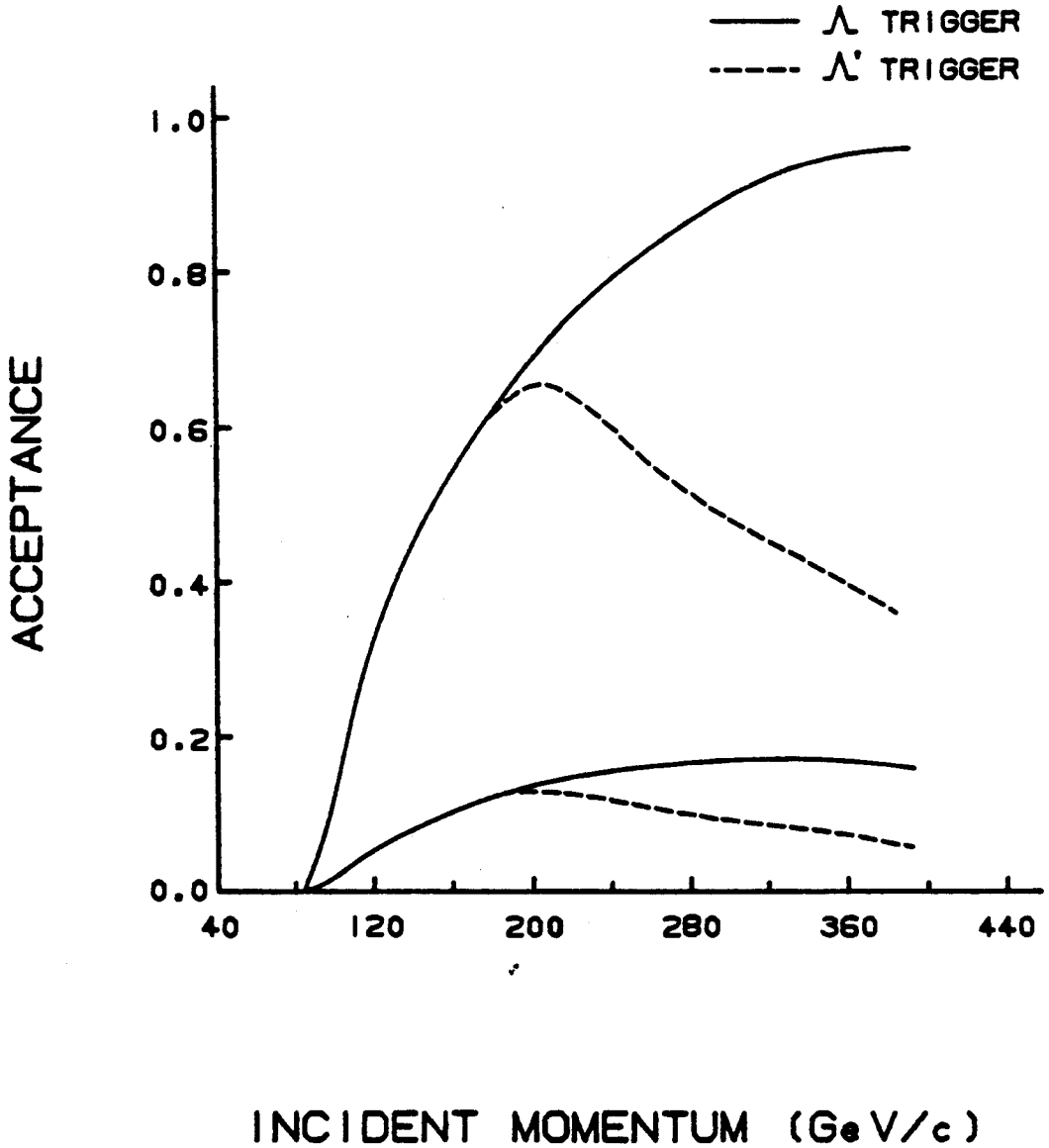

Figure 3.9 The spectrometer acceptance for beam Λ's which pass the Λ and Λ' triggers. The upper curves are normalized to the number of Λ's in the decay volume and the lower curves correspond to the total acceptance.

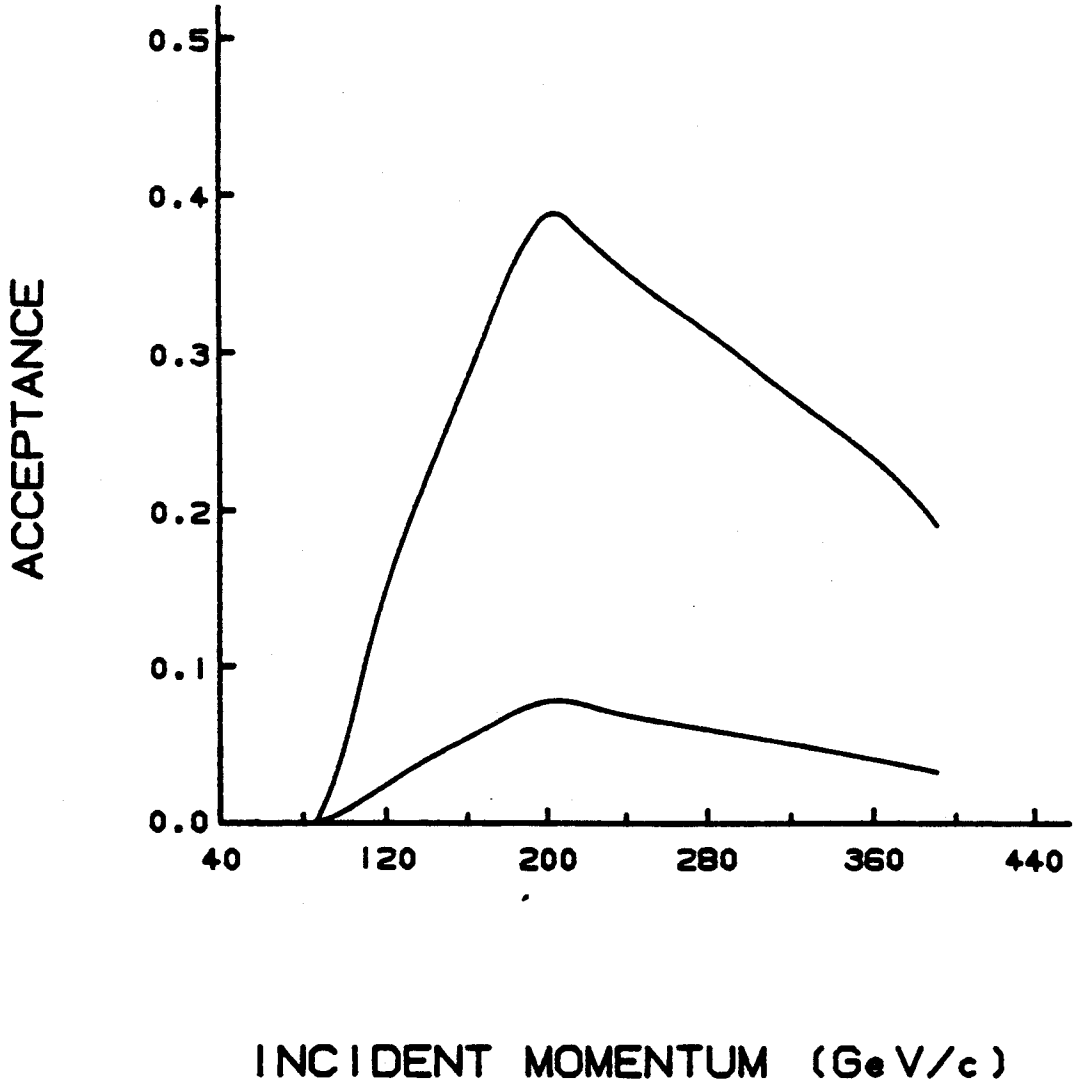

Figure 3.10 The spectrometer acceptance for Σ°'s which pass the Σ° trigger. The upper curve is normalized to the number of Λ's in the decay volume and the lower curve corresponds to the total acceptance.

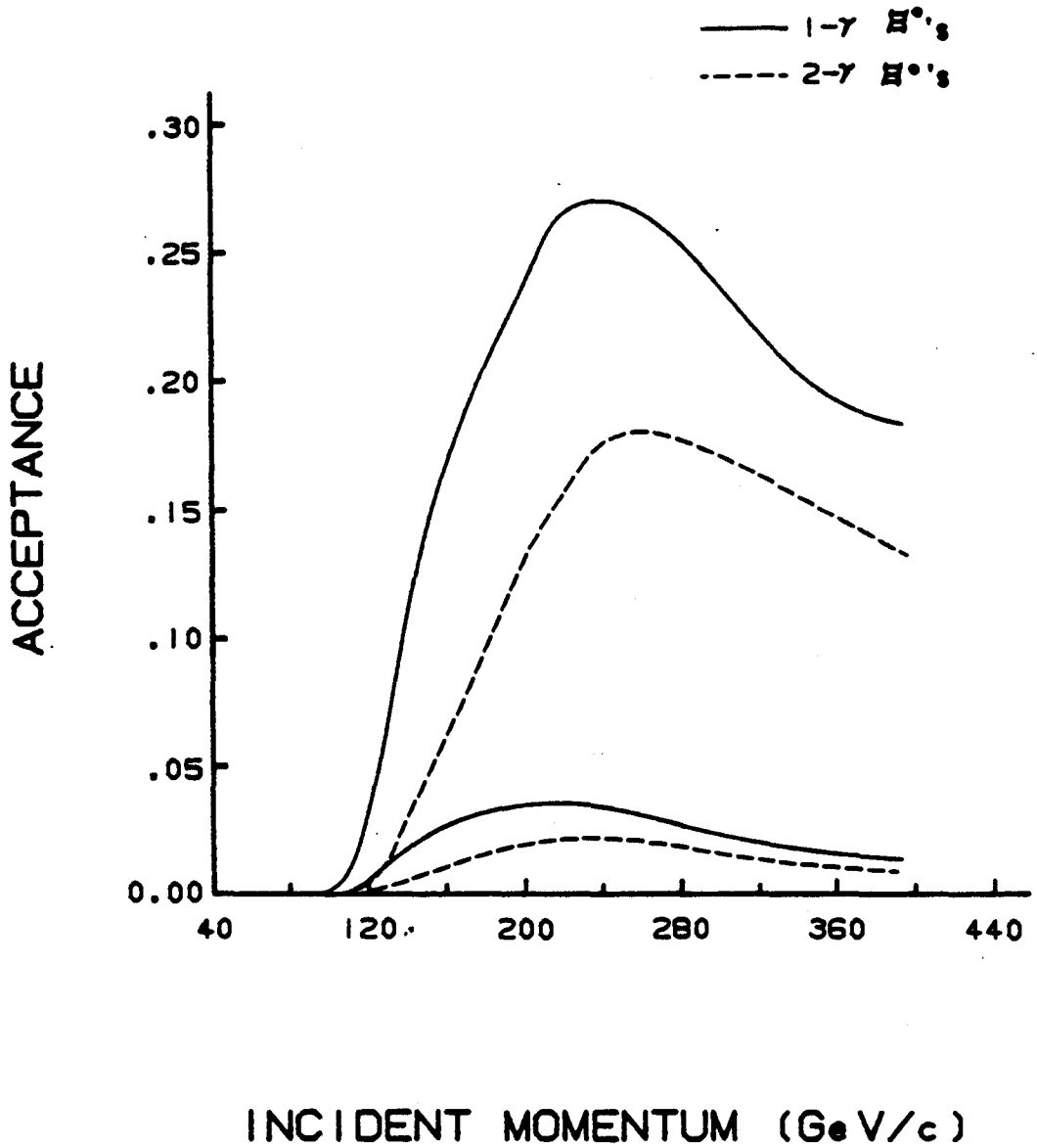

Figure 3.11 The spectrometer acceptance for Ξ°'s which pass the Σ° trigger. The upper curves are normalized to the number of Λ's in the decay volume and the lower curves correspond to the total acceptance.

normalized to the number of Λ's in the decay volume and correspond to the trigger efficiency for detecting a particle whose daughter Λ decays in the fiducial volume. The lower curves correspond to the total acceptance. They include the reconstruction efficiency and lifetime correction as well as the geometrical acceptance. For the appropriate momentum spectra, the overall acceptances for Λ', Σ°, and $1\text{-}\gamma\ \Xi^\circ$ (normalized to Λ's in the decay volume) are 0.29, 0.15, and 0.04 respectively.

Those Monte Carlo events which passed the experimental trigger requirements (either Λ' or Σ° as needed) were written to a tape in the same format as the data. The Monte Carlo tapes could then be analyzed with the same program used to analyze the data.

CHAPTER 4

Analysis II: Cross Section

4.1 Cross Section Definition and Related Terms

We are interested in the cross section for the process $\Lambda+Z \rightarrow \Sigma^{\circ}+Z$. A Λ beam traversing a target of length, L, produces a Σ° which decays almost immediately by $\Sigma^{\circ} \rightarrow \Lambda\gamma$. The daughter Λ and γ must emerge intact from the target or the event will be vetoed by counter S2. The number of Σ°'s, dN, produced in an increment dx of target material by N_0 incident Λ's is

$$dN = N_0 \, \rho \, \sigma \, \frac{A_0}{A} \, dx \, e^{-x/L_{abs}}$$

where A_0 is Avagadro's number, A is the atomic number, ρ is the density, and σ is the cross section for the process. A correction is made for nuclear absorption (L_{abs} = target

absorption length) of the incoming particle. In order for the daughter particles to survive as they traverse the remainder of the target, we must correct for nuclear interaction of the Λ and pair production (and thus veto) of the outgoing photon. The number of events which survive intact is

$$N_\Sigma = \int N_0 \rho \sigma \frac{A_0}{A} dx \; e^{-x/L_{abs}} \; e^{-(L-x)/L_{abs}} \; e^{-7(L-x)/9L_{rad}}$$

N_Λ can be defined as the number of Λ's detected downstream of the Primakoff target, i.e. $N_\Lambda = N_0 \; e^{-x/L_{abs}} \; e^{-(L-x)/L_{abs}}$, in which case factors involving L_{abs} are the same for Λ and Σ° and drop out of the equation. After integration the remaining terms can be rearranged as follows

$$N_\Sigma / N_\Lambda = \rho \sigma \frac{A_0}{A} L \; \{\tfrac{3}{7} X \; (1 - e^{-\frac{7}{9}X})\} \qquad (4.1)$$

where the term in curly brackets contains the suppression factor for photons converted in the target and will henceforth be labeled G. $X = L/L_{rad}$ = the length of the target in radiation lengths.

It is clear that N_Σ / N_Λ is the number we need to know to extract a value for the cross section. The numerator will be found by counting the number of Primakoff Σ°'s and the denominator will be furnished by the prescaled Λ' triggers. Corrections must be made for any differences in acceptance or trigger inefficiencies between the two samples. The

prescaled Λ' trigger is preferable to the Λ trigger because it includes S7 in the trigger and thus automatically compensates for veto inefficiencies and/or acceptance mismatch.

The only remaining difference in the Σ° and Λ' triggers is the γ detection. Thus the efficiency of the glass trigger and the geometrical acceptance for γ detection must be determined. Software cuts which include the γ component are only made on the Σ° sample and their effect must also be taken into account when normalizing to beam Λ's. The cross section can now be rewritten in terms of quantities that can be readily extracted from the data.

$$\sigma(\Sigma^\circ) = \frac{A}{G\rho A_0 L} \quad \frac{N(\Sigma)}{f\ N(\Lambda)\ \varepsilon_1\ \varepsilon_2\ \varepsilon_3\ \varepsilon_4} \tag{4.2}$$

where $N(\Sigma)$, $N(\Lambda)$ are the number of reconstructed Σ°'s and Λ's in the final sample of Σ° and Λ' triggers.

ρ, A are the density and atomic number of the target material.

L, G are properties of the target (see Table 2.1 for L, L_{rad}).

f = prescale factor for the Λ' trigger.

ε_1 = γ acceptance.

$\varepsilon_2 = \dfrac{\text{(No. of } \Sigma^\circ\text{'s after } \Sigma^\circ \text{ cuts)}}{\text{(No. of } \Sigma^\circ\text{'s after } \Lambda \text{ cuts)}}$

ε_3 = albedo correction factor.

ε_4 = glass trigger efficiency.

The rest of this section will describe how each term in this rate expression was determined.

4.1.1 Photon Acceptance

The terms in the denominator that deal with γ acceptance and Σ° yield after cuts are best determined by using the Σ° Monte Carlo. The overall acceptance has already been shown in the Fig 3.10. The number of interest, ε_1 in Eq. 4.2, is only that part of the acceptance which includes the γ-ray. It is not normalized to the total number of Σ°'s generated, but to those which have already passed the Λ' trigger. From the Monte Carlo we find that 49% of the Σ°'s which pass the Λ' trigger will trigger the glass as well. Most of this loss is due to a photon hitting above or below the analyzing magnets' aperatures. Thus $\varepsilon_1 = 0.495 \pm 0.004$.

4.1.2 Software Cuts

The software cuts which were applied to all charged tracks were summarized in Table 3.1 under the name "Λ cuts". The name "Σ° cuts" was applied to all cuts which used γ information and were therefore applicable only to events from the Σ° trigger sample. The fraction of Monte Carlo events left after each cut was presented in the right columns of the

table. Term ε_2 is simply the ratio of the fraction of Σ°'s remaining after all Σ° cuts to those surviving the Λ cuts alone: $\varepsilon_2 = 0.35/0.70 = 0.50 \pm 0.01$.

4.1.3 Albedo calculation

The front face of the hadron veto system S7+S7a was mounted only a centimeter from the lead converter and was therefore sensitive to backscatter from those electromagnetic showers which were initiated in the lead. A certain proportion of non-hadronic showers were thus vetoed. Even though the counters were included in the Λ' trigger, this did not affect that trigger sample since beam Λ's had no accompanying γ-ray. A correction for this effect, ε_3 in Eq. 4.2, has been calculated by the following method.

The total sample of prescaled Λ triggers was separated into seven groups according to target. The events were subjected to all the Λ cuts, and all Σ° cuts except the exclusion of a γ in the S3-S4, S5-S6 counters. In addition, all events with hits in C7 other than those produced by the charged tracks were also rejected. Since this particular sample of prescaled Λ's with a well identified cluster in the glass was richer in out-of-time glass hits than the data sample, a stricter timing cut than that used for the Σ°

candidates had to be applied. All blocks known to be out of time have already been removed from the summary tapes. However, because of the TDC event offset problem, some of the blocks had no recoverable timing information. If one of these blocks was the central block of an identified cluster the stricter cut removed the event from the sample. This eliminated 17% of the data.

Next the data for each target was separated into four catagories corresponding to the following configurations:

$(T1+T2+S7a)\cdot(T3+T4)$ = group 1 (backscatter or hadrons)

$(\overline{T1+T2+S7a})\cdot(T3+T4)$ = group 2 (photons)

$(T1+T2+S7a)\cdot(\overline{T3+T4})$ = group 3

$(\overline{T1+T2+S7a})\cdot(\overline{T3+T4})$ = group 4

where T1, T2, T3, T4, S7a refer to latches set by the corresponding phototubes. Define G_1, G_2, G_3, and G_4 as the number of events which fall into each of the four groups. S7 and S8 have efficiencies ε_a and ε_b which may differ from unity and there is a certain probability that a true photon will not convert in the lead. Therefore, the albedo is not a simple ratio of $G_1/(G_1+G_2)$. The more general form can be written as follows. Let n_1, n_2, n_3 refer to the number of photons which convert in the lead and backscatter, convert in the lead and don't backscatter, and don't convert in the lead. Thus $n_3=e^{-\frac{7}{9}X}(n_1+n_2+n_3)$. For 1.7 radiation lengths of

lead this gives $n_3=0.35(n_1+n_2)$. G_1 through G_4 can be written in terms of these variables as follows:

$$G_1 = \varepsilon_a\varepsilon_b n_1$$

$$G_2 = \varepsilon_b n_2+(1-\varepsilon_a)\varepsilon_b n_1$$

$$G_3 = \varepsilon_a(1-\varepsilon_b)n_1$$

$$G_4 = n_3+(1-\varepsilon_b)n_2+(1-\varepsilon_a)(1-\varepsilon_b)n_1 = (1.35-\varepsilon_b)n_2+(1.35-\varepsilon_a-\varepsilon_b+\varepsilon_a\varepsilon_b)n_1$$

which can be solved for ε_a, ε_b, n_1, n_2.

Rather than solving for the four unknowns directly, an independent measure of ε_a and ε_b was obtained from a subsample of the prescaled Λ triggers: charged p or π^- tracks which intersect the glass. This sample yields counter efficiencies of $\varepsilon_a=\varepsilon_b=.97$, reducing the number of unknowns to two. Since groups 1 and 2 are more reliable (delta rays, backward going particles, and noisy glass can inflate groups 3 and 4), the first two equations were solved for n_1, n_2 and thence n_3. The albedo was defined as $n_1/(n_1+n_2)$ and the correction factor used in the rate calculation was defined as $(n_2+n_3)/(n_1+n_2+n_3)$. Table 4.1 lists the actual number of events in groups 1-4 and the calculated albedo and correction factor for each target. The numbers were consistent with each other within their errors and were eventually summed to obtain an average correction factor of $\varepsilon_3 = 0.75 \pm 0.02$ (or albedo of 0.34 ± 0.02).

Table 4.1

Albedo Calculation

Target	Number of Events G_1	G_2	G_3	G_4	Albedo	Correction Factor
1	32	52	2	13	0.39 ± 0.08	0.71 ± 0.07
2	17	42	0	11	0.29 ± 0.08	0.78 ± 0.07
3	20	46	4	17	0.30 ± 0.08	0.77 ± 0.07
4	53	100	6	30	0.35 ± 0.06	0.74 ± 0.05
5	74	164	16	47	0.31 ± 0.05	0.76 ± 0.04
6	31	63	1	14	0.33 ± 0.07	0.75 ± 0.06
7	103	177	19	56	0.37 ± 0.04	0.72 ± 0.03
EGS	193	414	10	183	0.33 ± 0.03	0.75 ± 0.02

Average Albedo over all targets: 0.34 ± 0.02

Average Correction Factor over all targets: 0.75 ± 0.02

The EGS Monte Carlo was run for the counter and glass configuration used in this experiment. Eight hundred 20 GeV photons were propagated through the scintillator-glass system. The counter efficiency was not explicitly input to the program, but a scintillator energy threshold of 0.2 MeV had much the same effect. The number of Monte Carlo events satisfying each of the veto configurations is also listed in the table. The correction factor calculated from this exercise was 597/800=0.75 in complete agreement with the experimental determination.

4.1.4 Glass Trigger Efficiency

The efficiency of the glass trigger must also be folded into the answer. Cuts similar to those used for the albedo calculation were applied to the sample of prescaled Λ and Λ' triggers to obtain a clean γ sample in which the hardware trigger had not been required. In addition, the events had to have veto latch configurations corresponding to group 1 or group 2. Since only the response of the glass was being tested, the reconstructed vees were not required to be a Λ or K^o.

Table 4.2

Glass Trigger Efficiency

Target	for Veto Configuration 1	2
1	0.92 ± 0.17	0.86 ± 0.13
2	0.91 ± 0.23	0.85 ± 0.14
3	0.95 ± 0.17	0.95 ± 0.14
4	0.92 ± 0.12	0.86 ± 0.09
5	0.86 ± 0.09	0.85 ± 0.07
6	0.84 ± 0.16	0.90 ± 0.12
7	0.89 ± 0.10	0.88 ± 0.07
Average efficiency:	0.89 ± 0.05	0.87 ± 0.04

Average over veto configuration: 0.88 ± 0.03

While these events did not require the glass trigger, they did not preclude it. The responses of the glass trigger logic were recorded in latches. The glass trigger efficiency was defined as the percentage of this cut sample with both main array and front wall latches set. The data were analyzed separately for each target and veto configuration. The results are shown in Table 4.2. No significant difference between the separate data sets was observed. Combining all the data sets yielded an average glass trigger efficiency of $\varepsilon_4 = 0.88 \pm 0.03$.

4.2 Primakoff Σ° Signal

4.2.1 Introduction

It now remains to count the number of Primakoff Σ°'s and beam Λ's in the experiment, $N(\Sigma^\circ)$ and $N(\Lambda)$ of Eq. 4.2. The number of Σ°'s expected from crude estimates of the lifetime is only one for every 200 events left after all Λ and Σ° cuts. There are two main sources of background: Ξ°s with one γ in the glass and unconverted beam Λ's with an accidental γ in the glass. Plots of the $\Lambda\gamma$ invariant mass, $M_{\Lambda\gamma}$, after cuts for all 7 targets (Figs 4.1 and 4.2) illustrate the problems inherent in picking a signal out of this background.

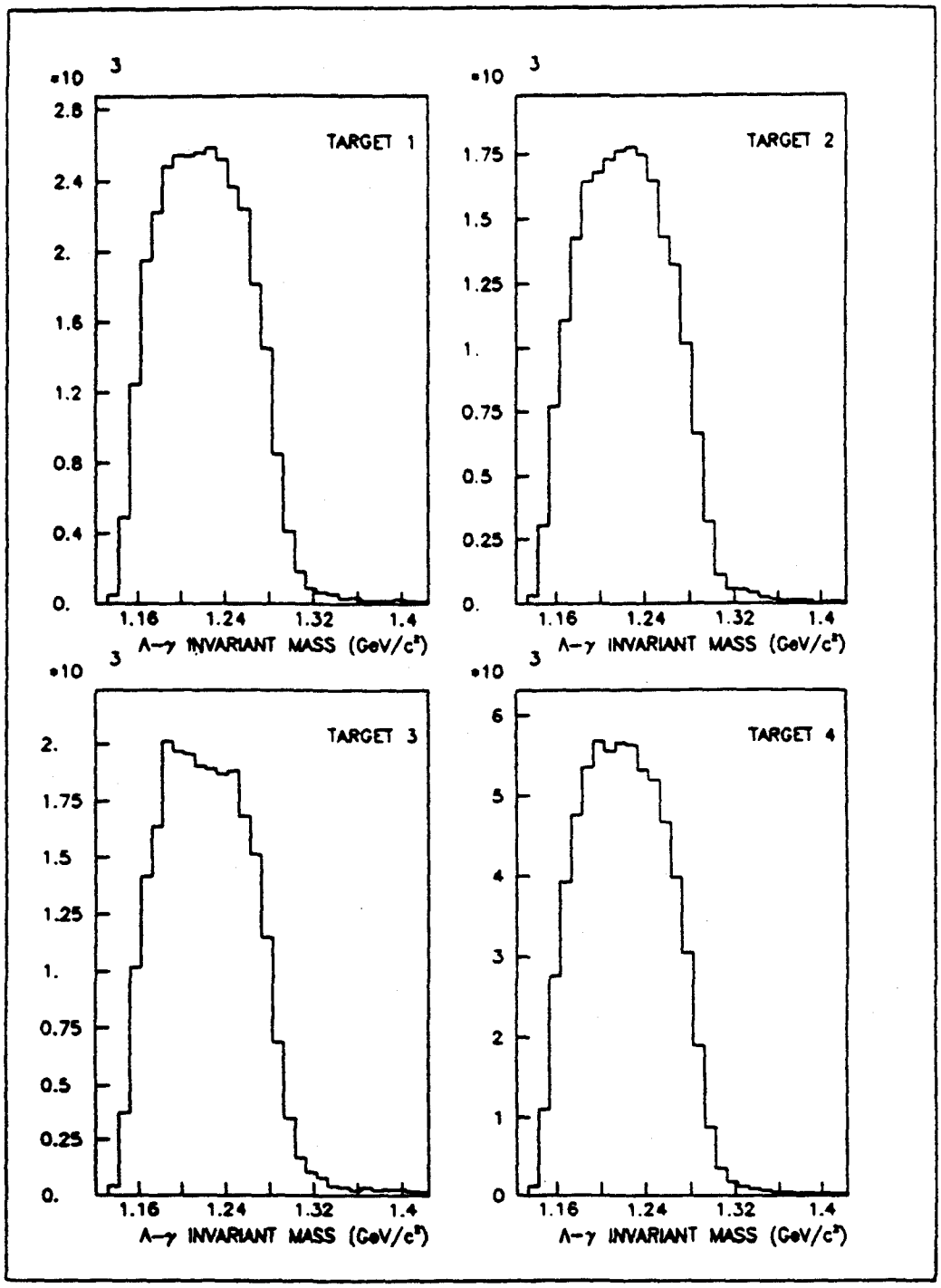

Figure 4.1 The ΛΥ invariant mass for data from targets 1-4 after "Λ" and "Σ°" cuts.

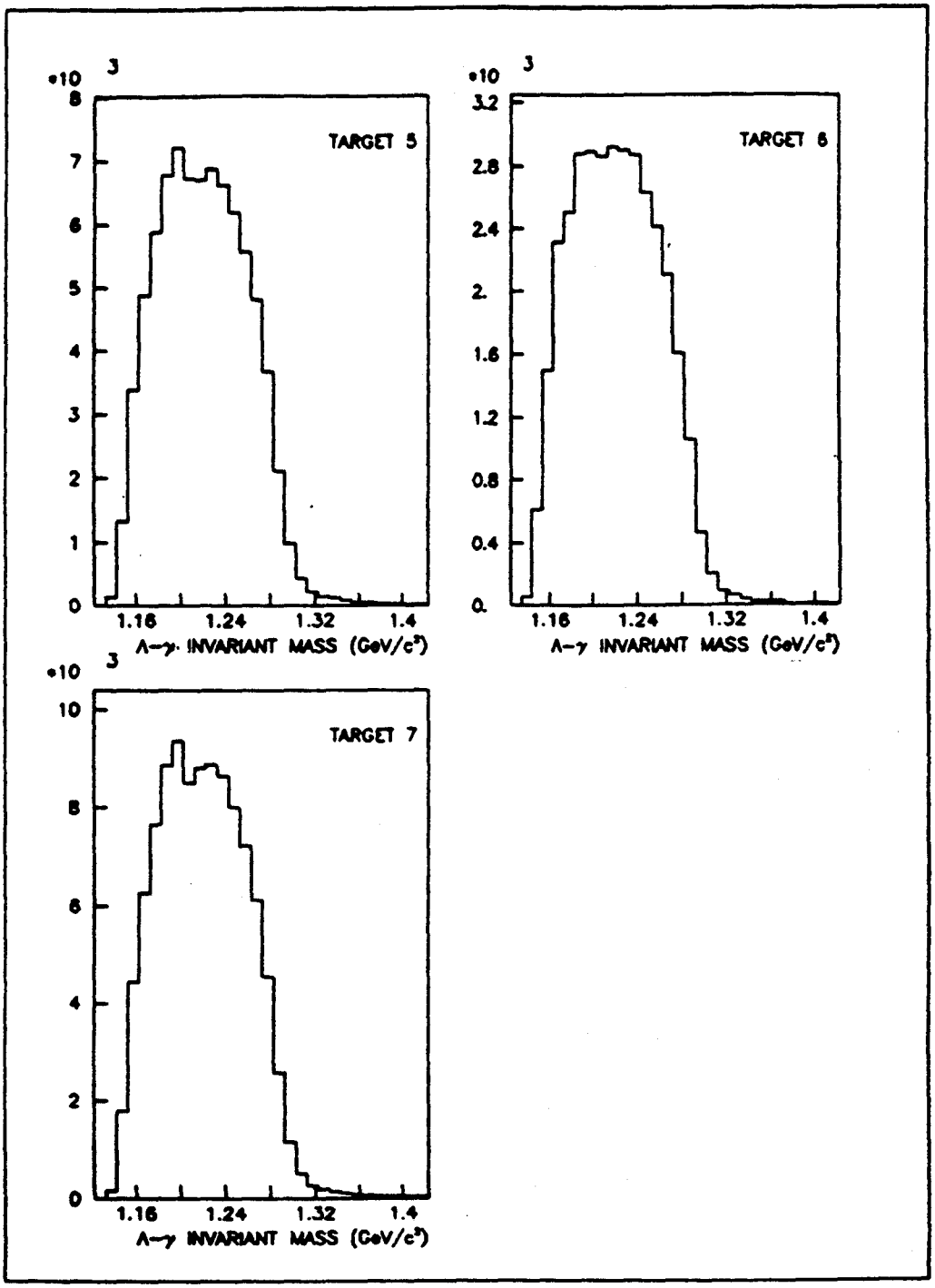

Figure 4.2 The ΛΥ invariant mass for data from targets 5-7 after "Λ" and "Σ°" cuts.

4.2.2 Further Kinematic Cuts

There are other kinematic variables which can distinguish between Primakoff Σ°'s and the background, the most powerful of which is target pointing. The x and y positions of the beam at both the production and Primakoff target were monitored throughout each run by taking the running average of the prescaled Λ's. The beam centroid thus defined changed by no more than 0.8 mm at either target over the course of the experiment. The path of the detected Λ was projected back to the plane of the production target. Its distance from the beam centroid, $r_{prod}(\Lambda)$, was then a measure of how closely it corresponded to the undeflected beam. A daughter Λ from Σ° or Ξ° decay will tend not to point back to the production target whereas a beam Λ will.

A parent particle reconstructed from the Λ and the γ can also be projected back to the production target. This target pointing variable is called $r_{prod}(\Sigma^\circ)$. Since the Primakoff Σ°'s are all produced in the forward direction, $r_{prod}(\Sigma^\circ)$ should be very small only for those particles which fulfill the Σ° hypothesis. Since the spectrometer had better position resolution in y than in x (due to the lack of magnet complications), the beam Λ distribution at the targets was elliptical rather than circular with a major-to-minor axis ratio of 1.23. Therefore the target pointing variables

actually used in the analysis were of the form $r^2 = x^2 + 1.5y^2$.

Two related variables can be defined here. The transverse momenta corresponding to the daughter Λ and Σ° target pointing variables are $p_t(\Lambda)=p_\Lambda \sin\theta_\Lambda$ and $Q=q_t=p_\Sigma \sin\theta_\Sigma$ where θ_Λ and θ_Σ are referenced to the centroid of the beam Λ's. Q is the variable which should be able to distinguish between forward going Primakoff Σ°'s and wider angle strongly produced Σ°'s. A third transverse momentum $p_t(\Sigma\Lambda)=p_\Lambda \sin\theta_{\Sigma\Lambda}$, where $\theta_{\Sigma\Lambda}$ is the angle between the Σ° and the daughter Λ, will have a Jacobian peak for a true Σ° decay, corresponding to a center of mass momentum of 74 MeV/c. All other Λ-γ combinations will be smeared out. Figs 4.3-4.7 show the above variables as generated by the various Monte Carlos. Arrows on the Σ°_{Pk} Monte Carlo distributions indicate optimum cuts and Table 3.1 indicates the percent of each event type which is removed by these cuts. One further cut, ECUT, takes advantage of the generally lower γ energy of the Σ° decay and its population distribution in r_γ-E_γ space, see Fig 4.8.

4.2.3 Failure of Strong Kinematic Constraint Method

A sample of data was obtained by applying these additional kinematic cuts. When the invariant mass for a Λ-γ

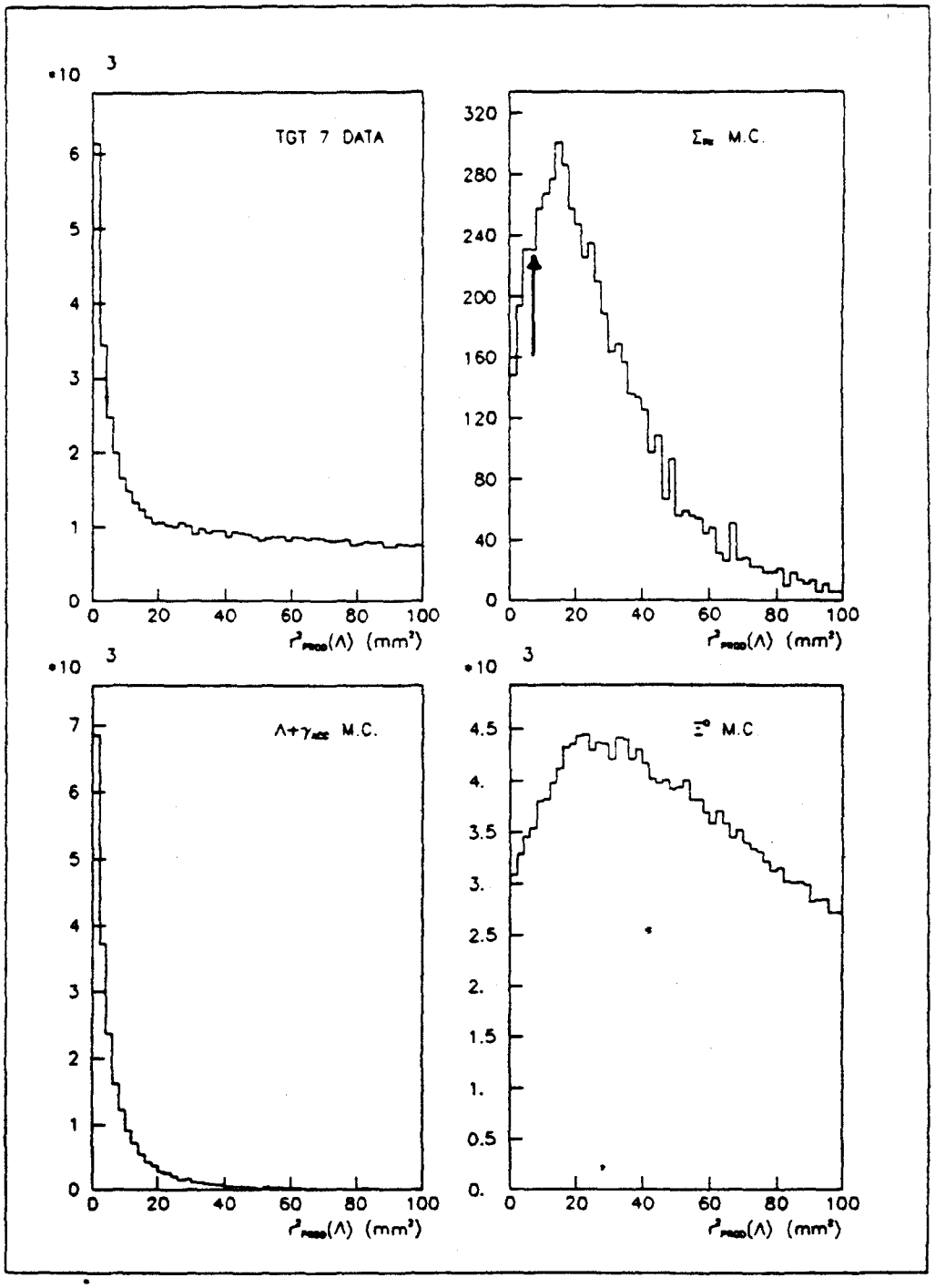

Figure 4.3 The distribution of Λ positions at the production target referenced to the beam centroid: $r^2_{prod}(\Lambda)$ for target 7 data.

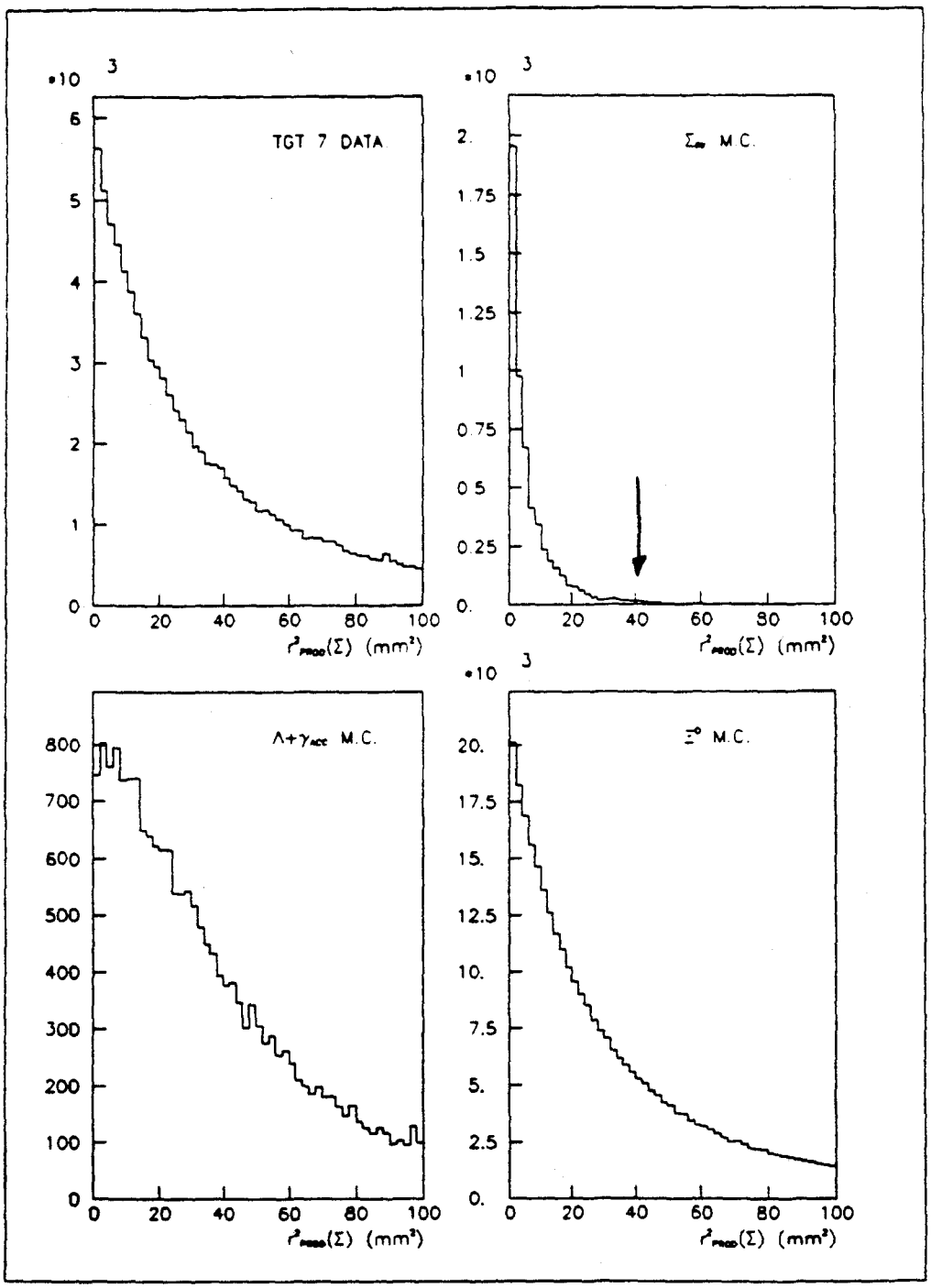

Figure 4.4 The distribution of the Σ° positions at the production target referenced to the beam centroid: $r^2_{prod}(\Sigma)$ for target 7 data.

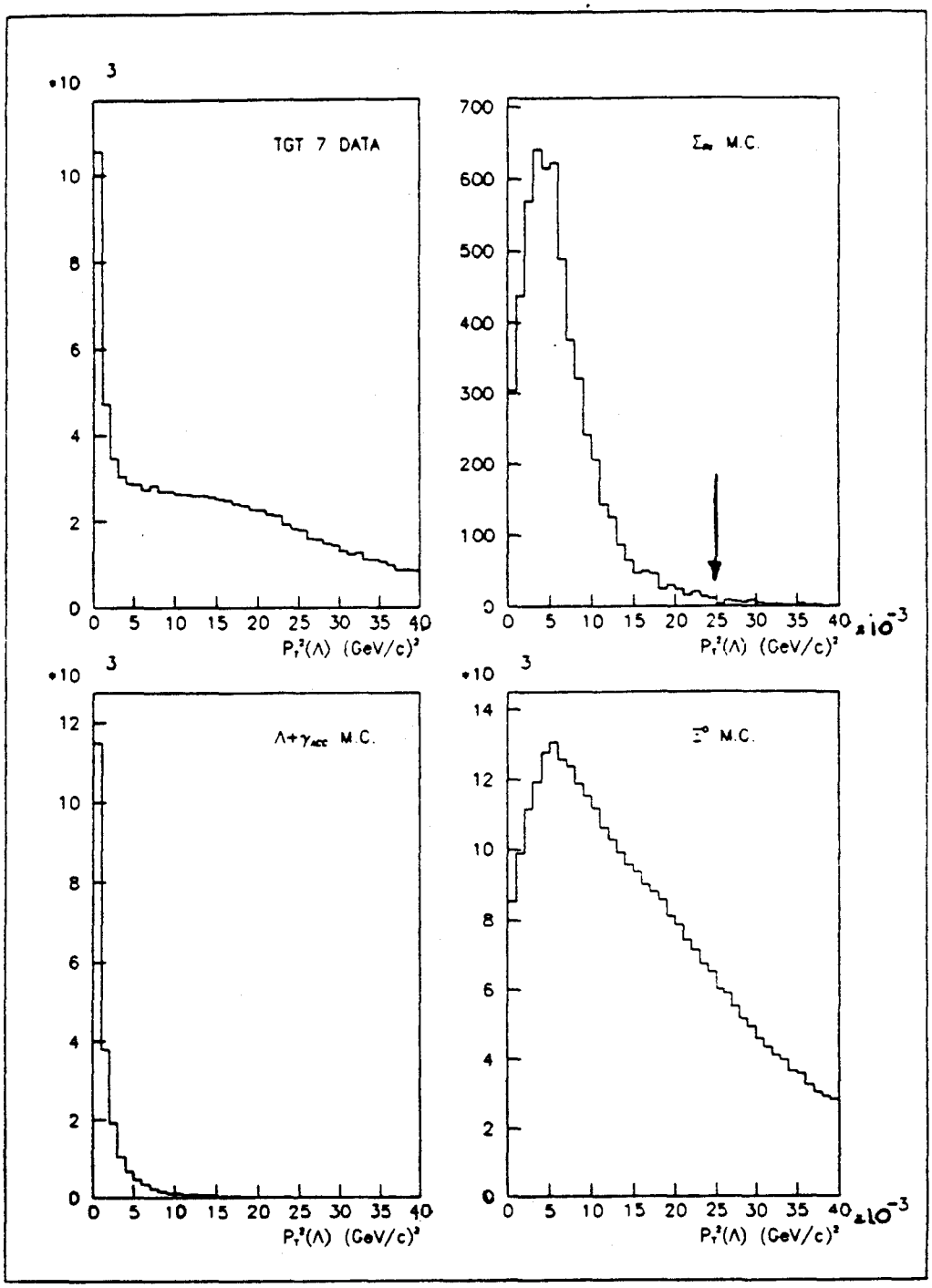

Figure 4.5 The distribution of the Λ transverse momentum relative to the beam: $p^2_t(\Lambda)$ for target 7 data.

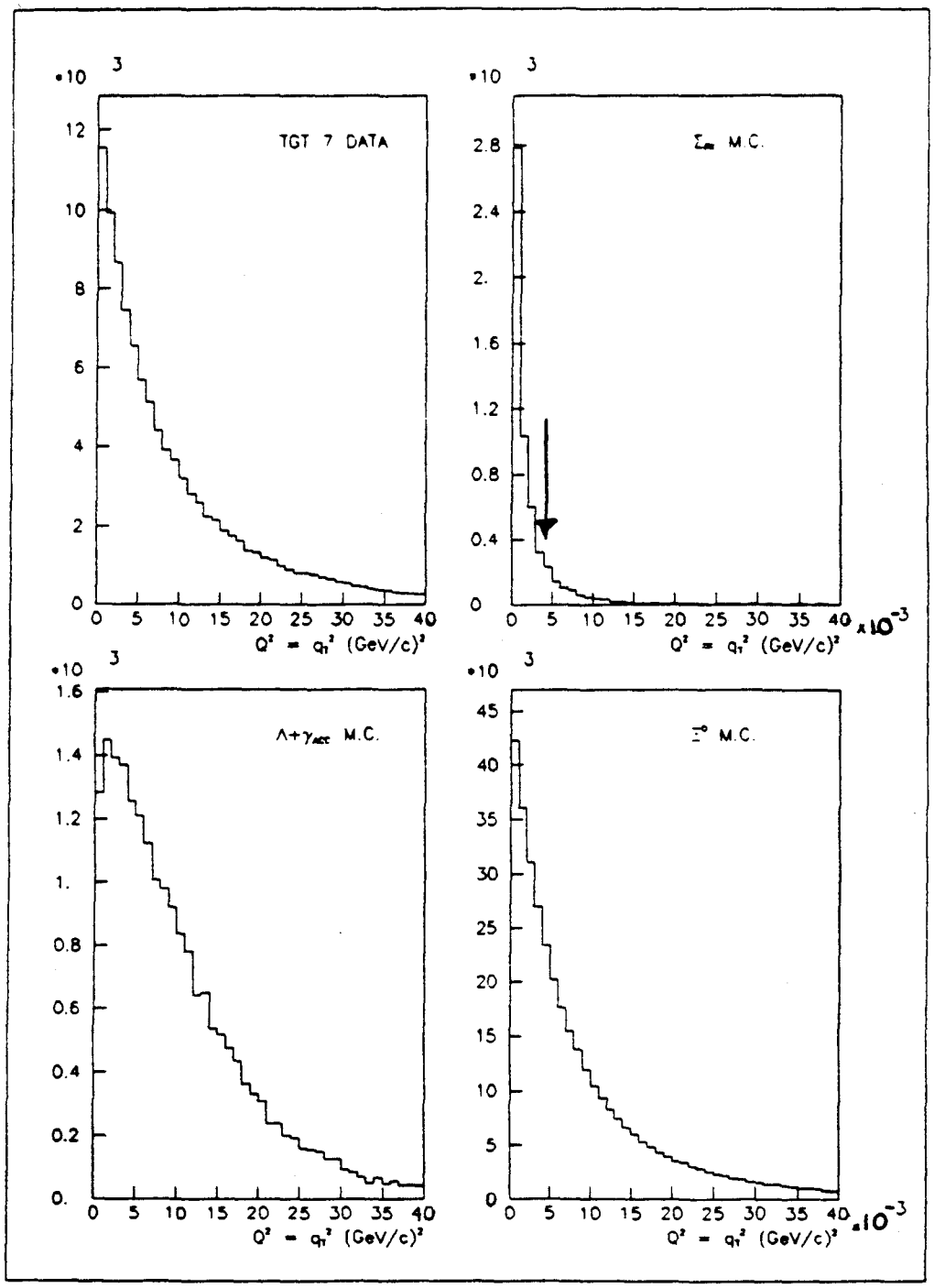

Figure 4.6 The distribution of the Σ° transverse momentum relative to the beam: $Q^2=q^2_t$ for target 7 data.

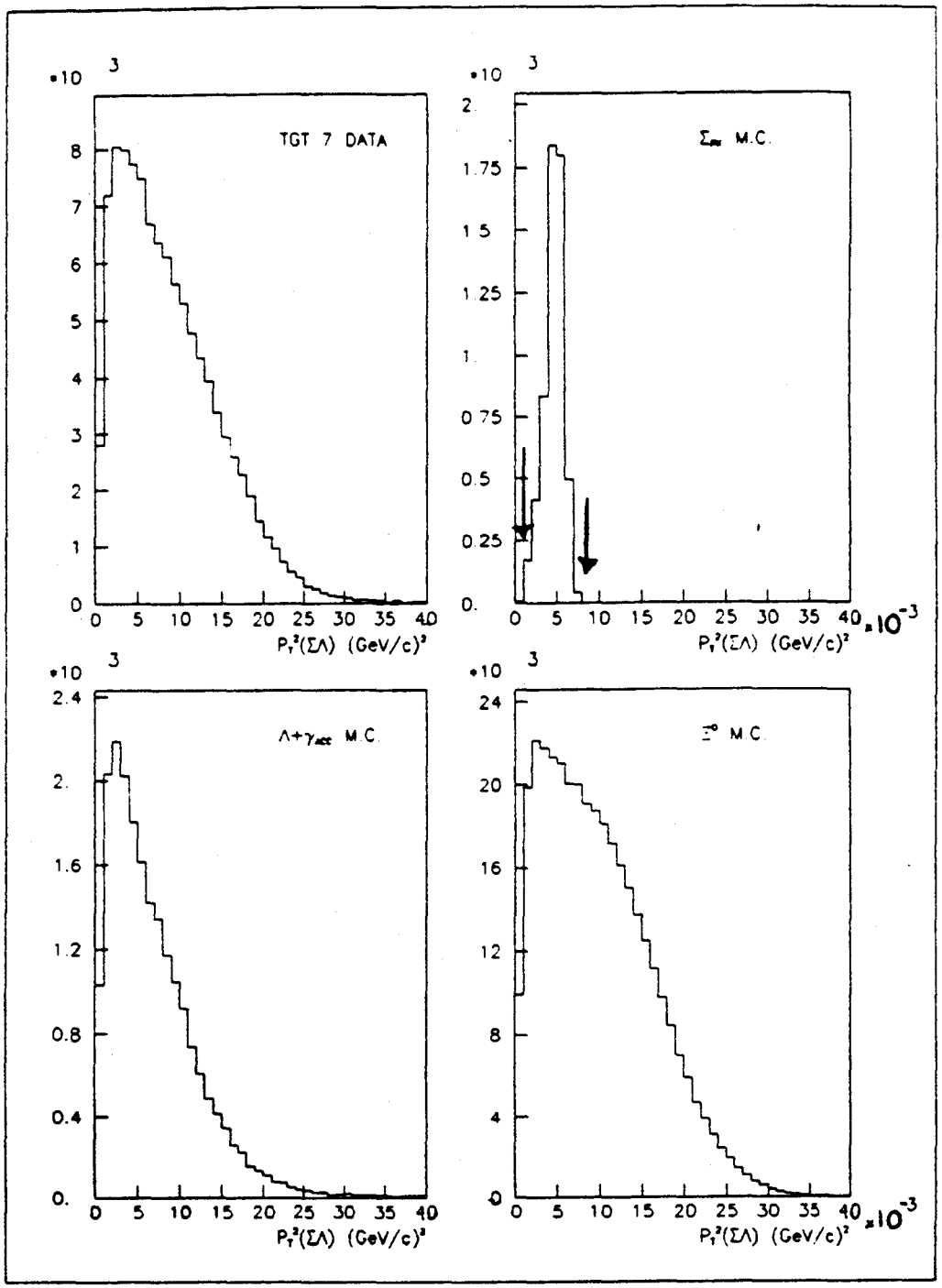

Figure 4.7 The distribution of the Λ transverse momentum relative to the parent Σ°: $p^2_t(\Sigma^\circ\Lambda)$ for target 7 data.

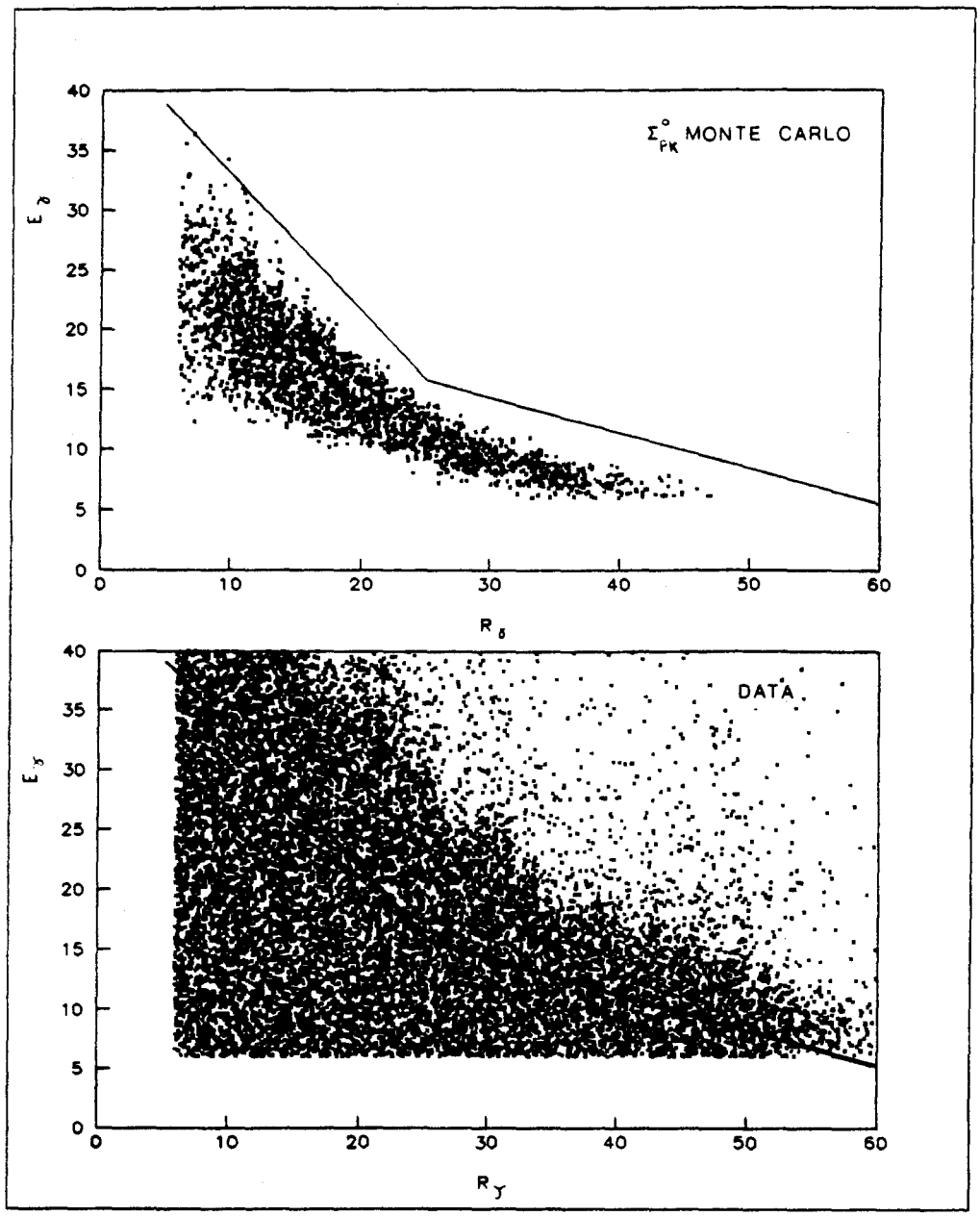

Figure 4.8 Gamma energy vs. distance to the glass hit from the array center. Lines indicate ECUT boundary; all events above it were rejected.

vertex constrained at the Primakoff target was plotted, these events all clustered in a peak centered at the Σ° mass, Fig 4.9. Although the distribution resembles a Σ° mass peak, these events are not predominantly Σ°'s. A Monte Carlo analysis shows that they are mostly Ξ°s and beam Λ's + γ_{acc} which have survived all the additional cuts precisely because they are kinematically identical to the Primakoff Σ°'s. The problem can be restated as follows: since the center of mass momentum for Σ° decay is so low, it doesn't take much energy in the glass to combine with a beam Λ to form a Σ° facsimile. On the other hand, the center of mass momentum for $\Xi^\circ \rightarrow \Lambda \pi^\circ$ is high enough (135 MeV/c) that the loss of one γ puts the remaining Λ and γ into the same kinematic region as the Σ° decay products.

It is very difficult to subtract the background from the sample in Fig 4.9 since the shape of all the Monte Carlo's look alike after these cuts. One is forced to rely on normalizing the high-Z target data to the low-Z in order to obtain an answer. Since that method is fraught with possible systematic errors, it would clearly be preferable to be able to obtain the answer independently for each target.

No cuts, however, can be found which drastically reduce the background under the Σ° peak. Instead, they only shave the edges off the invariant mass plot until background and

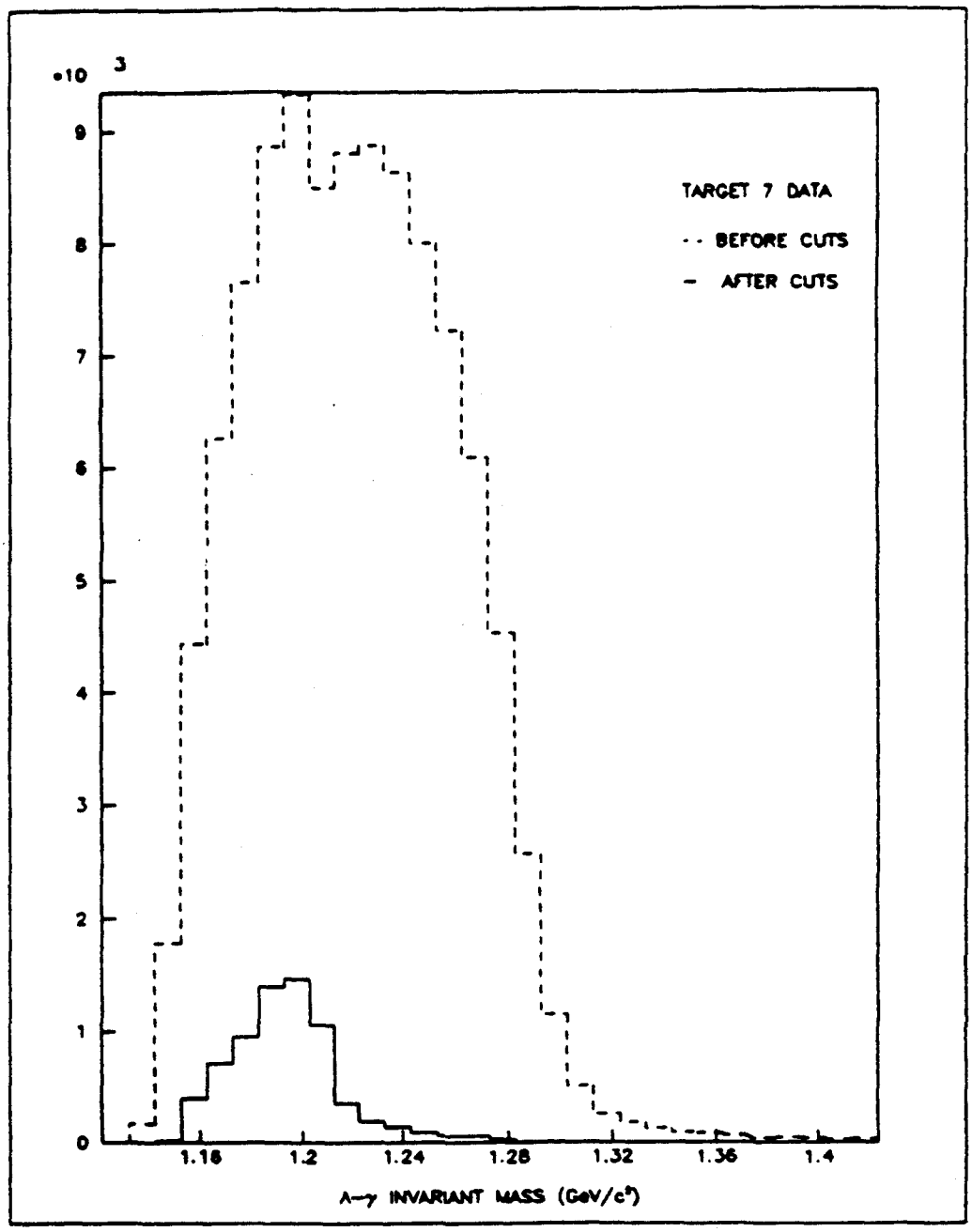

Figure 4.9 The ΛΥ invariant mass for target 7 data before and after tight kinematic cuts. See Figs 4.3-4.8 for details on the cut boundaries.

signal are indistinguishable. Even an attempt at full reconstruction of the Ξ^0s met with failure. The data were reconstructed as if they consisted solely of Ξ^0s. The decay vertex was determined from the z of closest approach of the daughter Λ to the beam and the second γ was constrained to not hit the glass. This was done in the hopes that the true Ξ^0s could be eliminated on the basis of a good χ^2 to this Ξ^0 hypothesis. When the Σ^0 Monte Carlo was run through the analysis, its χ^2 distribution was as narrow as the χ^2 from generated Ξ^0 events with one γ in the glass, and the approach was abandoned.

4.2.4 Multi-dimensional Statistical Analysis

4.2.4.1 Introduction

Since it was impossible to obtain a clean Σ^0 sample, a statistical method was applied. Instead of using the variables described in the previous sections as cuts, they were used as shapes characteristic of each source of background. If each shape is given the proper normalization, the shape of their sum should match the shape of the corresponding variable in the data. A multi-dimensional χ^2 fit was performed over three such variables, varying the

relative proportions of four input populations, to give the best fit to the data.

4.2.4.2 Input Populations

The input populations consisted of the Primakoff signal and three types of background. Two populations, the Σ°_{Pk} and Ξ° Monte Carlo, have already been described in some detail. A third population was created by combining the Λ_B Monte Carlo with the glass and latch information from data collected with the Σ° trigger ($\Lambda_B+\gamma_{acc}$ Monte Carlo). A fourth Monte Carlo simulated incoherent strong Σ° production by generating Σ°'s with an e^{-AQ^2} transverse momentum dependence. A coefficient of A=10 GeV^{-2} matched the target 7 data at $Q^2 > 0.02$ GeV^2 where the signal was easier to pick out of the background and where the strong production dominated. An e^{-10Q^2} dependence is similar to the p_t distributions for many strong production processes. The statistics were too poor to distinguish among the various targets.

All the input populations came in sets of seven. Subtle differences in the γ environment due to the size of the Primakoff target, necessitated target dependent γ information for the $\Lambda_B+\gamma_{acc}$ Monte Carlo. Since the drift chambers were

not always operative and decoding efficiencies varied with time, target data sets had differing track resolutions as well. Therefore, data from each of the seven targets were fitted to input distributions uniquely tailored to the resolution, chamber efficiency, and γ environment of each sample.

4.2.4.3 Global Fit

Each input population was subjected to only the minimal Σ° cuts of Table 3.1, thus maintaining the variable shapes characteristic of each group. Then three variables not involved in the cuts were binned to form a 3-dimensional matrix for each population. These matrices, $\{C_{ijk}\}_m$, along with the data matrix $\{E_{ijk}\}$, were used to form the following sum:

$$\chi^2 = \sum_{ijk} \frac{[E_{ijk} - \sum_m a_m C_{ijkm}]^2}{\sigma^2_{ijk}}$$

where indices ijk run over variable bins, m runs over the number of populations, and σ_{ijk} is the standard deviation. In this analysis σ_{ijk} was defined as

$$\sigma_{ijk} = \sqrt{E_{ijk} + \sum_m a_m^2 C'_{ijkm}}$$

Usually, $C'_{ijk} = C_{ijk}$, but if $E_{ijk} = 0$, then bin ijk was not included in the sum over populations, e.g. $C'_{ijkm} = 0$. If $E_{ijk} \neq 0$, and $C_{ijk} \neq 0$ for at least one other population, then corresponding bins in the other groups which were zero were assigned a value of unity, e.g., if $C_{ijkm} = 0$; $C'_{ijkm} = 1$.

The coefficients a_m gave the relative proportion of each input population. The χ^2 was minimized with respect to these coefficients yielding a system of four simultaneous equations which were then solved for a_m. Since the coefficients were also used to calculate σ_{ijk}, the minimization procedure had to be iterated several times. The advantage of this statistical method is that not only does it yield the number of Σ^o's with uncertainties for each target, but the χ^2 automatically gives a measure of how well the background is understood. Table 4.3 lists the number of events from each population fitted to each of the target data sets using $M_{\Lambda\gamma}$, Q^2, and $r^2_{prod}(\Lambda)$ as the three variables. These three variables were chosen because they are relatively independent of each other and are each sensitive to different distinguishing characteristics of the input populations.

The Coefficients derived from the fit can be used to weight the input populations and their sum can be visually inspected to see how well the fit procedure is working. Q^2

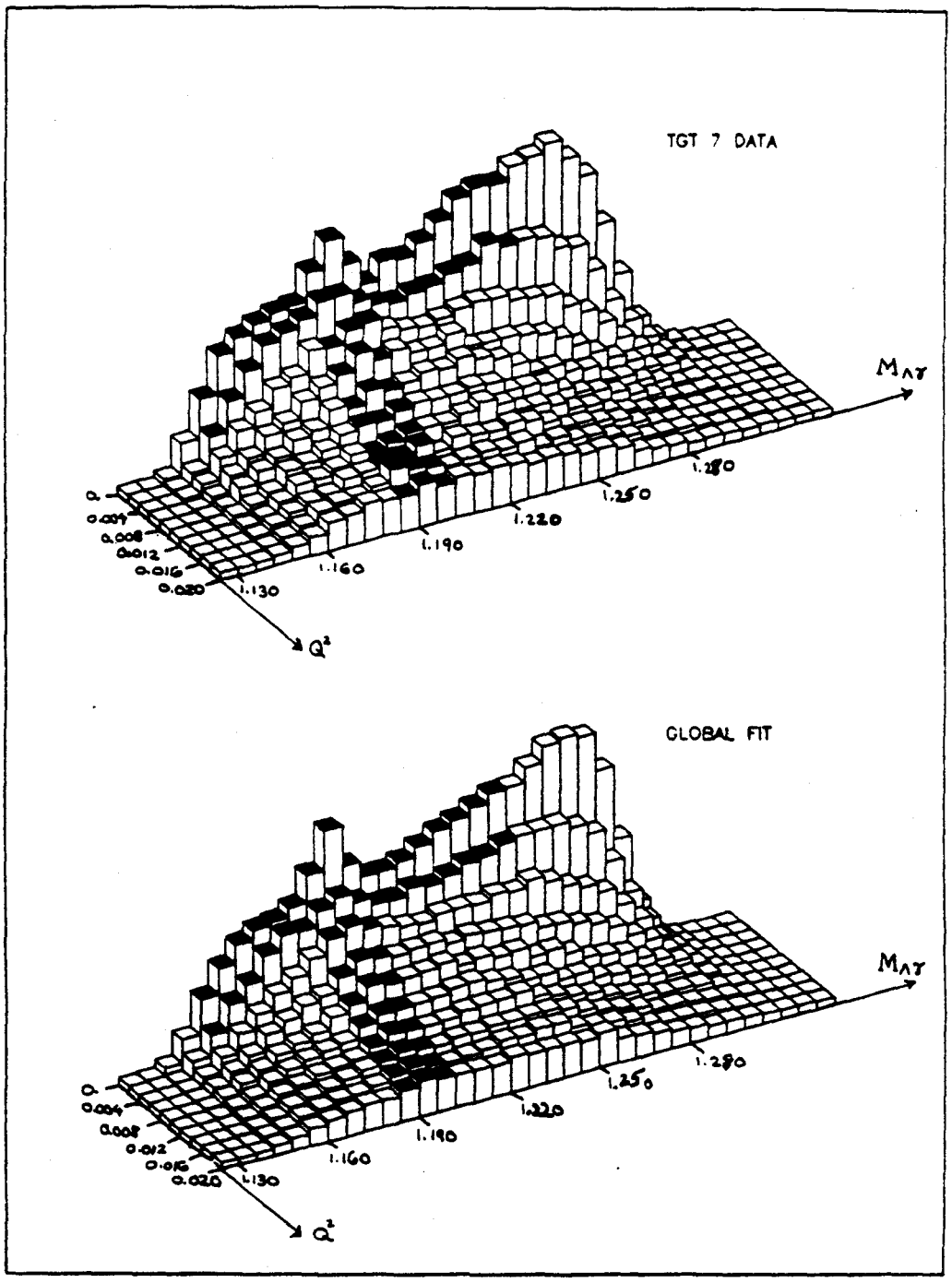

Figure 4.10 The $\Lambda\gamma$ invariant mass vs Q^2 for target 7 data (a) and the sum of the fitted input populations (b).

and the $\Lambda\gamma$ invariant mass are two variables in which the Primakoff Σ°'s have an easily identifiable signature. These variables are plotted as a 2-dimensional histogram in Fig 4.10 for both target 7 data and the sum of the fitted input populations.

Since the background populations cover a large kinematic range, they may fit well globally, but deviate locally, perhaps in the narrow region populated by Primakoff Σ°'s. For example, completely removing the $\Sigma^{\circ}{}_{Pk}$ Monte Carlo population from the global target 7 fit changes the Ξ° contribution by 0.6% and the $\Lambda\gamma$ by 0.1%, while increasing the χ^2 per degree of freedom by only 4%. Thus, the importance of the global fit lies not in the number of fitted Σ°'s, but in how well it simulates the background in the Σ° kinematic region. This is crucial in how one interprets the $\Sigma^{\circ}{}_{Pk}$ signal. At the Σ° mass, Q^2 should show a sharp forward peak compared to the off-mass distributions. A naïve estimate of the Primakoff signal would then be obtained by counting the number of events above background in this low Q^2 peak. In fact, an examination of Fig 4.10 shows that both high and low mass regions are more sharply peaked at low Q^2. The mass distribution is equally hard to interpret. At high Q^2, the data tends to peak broadly at the Σ° mass. At low Q^2 it is unclear whether there is still a broad hump under the $\Sigma^{\circ}{}_{Pk}$ events or not.

The situation can be understood by examining the sum of the background populations after normalization by the global fit coefficients. Slices in both Q^2 ($1.183<M_{\Lambda\gamma}<1.203$) and $M_{\Lambda\gamma}$ ($Q^2<0.004$), corresponding to the shaded areas in Fig 4.10, are plotted in Fig 4.11 for only the fitted background. The flattening of the Q^2 background near zero and the slight concavity of the $M_{\Lambda\gamma}$ background at the Σ° mass indicate that straightforward counting will yield systematically low results for the Σ°_{Pk} cross section.

4.2.4.4 Background Subtraction

The final determination of the number of Σ°'s was performed in the following manner. A file of the fitted background was created using the coefficients from the global fit described above. This background file did not include the Σ°_{Pk} Monte Carlo, nor the Σ°_{str} Monte Carlo component which will be subtracted explicitly from the Primakoff signal later (see Section 4.3). Figs 4.12-4.15 show the invariant mass of the data minus this fitted background file for each target. Any flaws in the global fitting program now show up as a secondary uncancelled background.

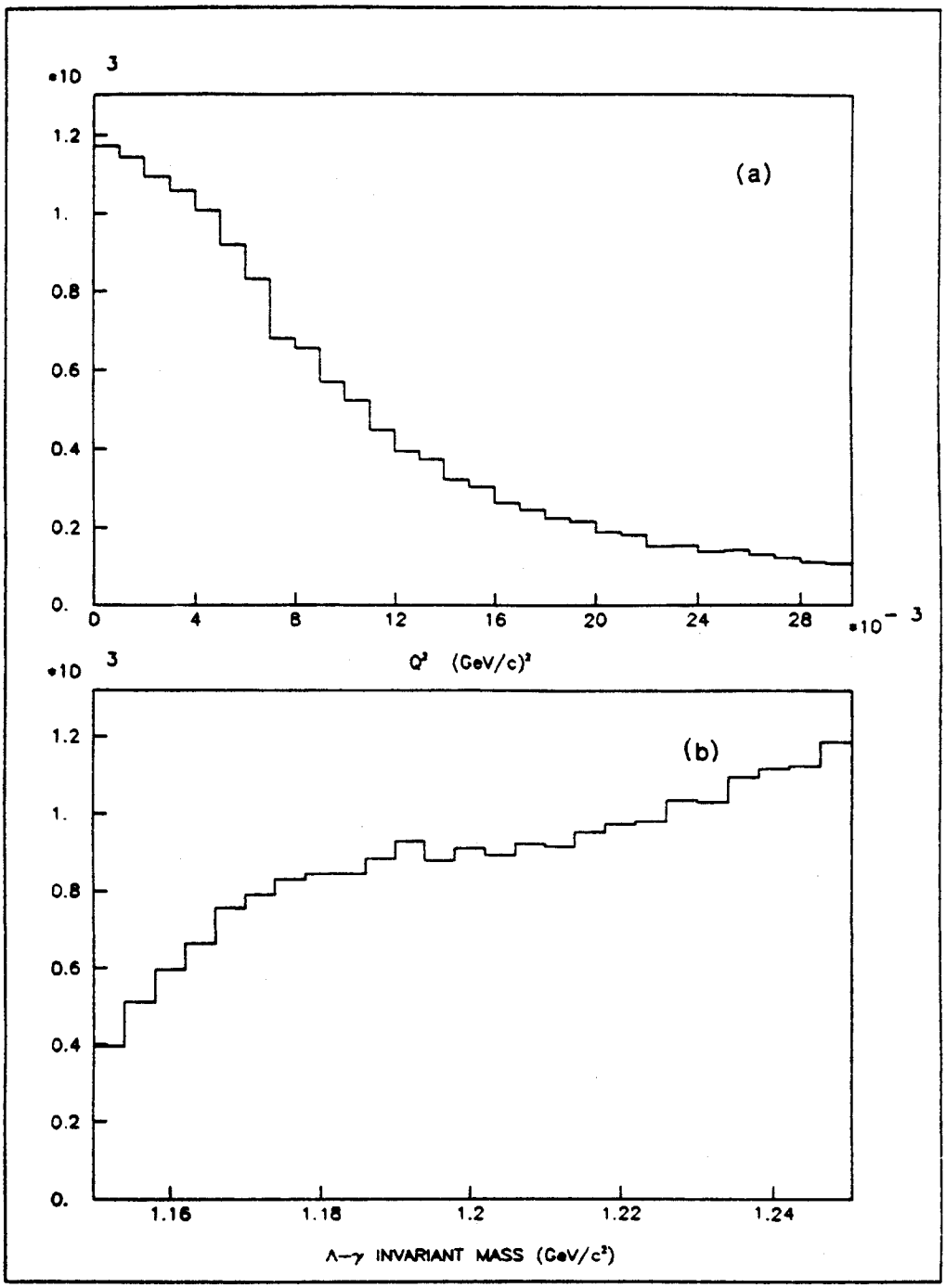

Figure 4.11 The Q^2 (a) and M(ΛY) (b) distributions from the fitted input populations omitting the Σ^0_{Pk} component.

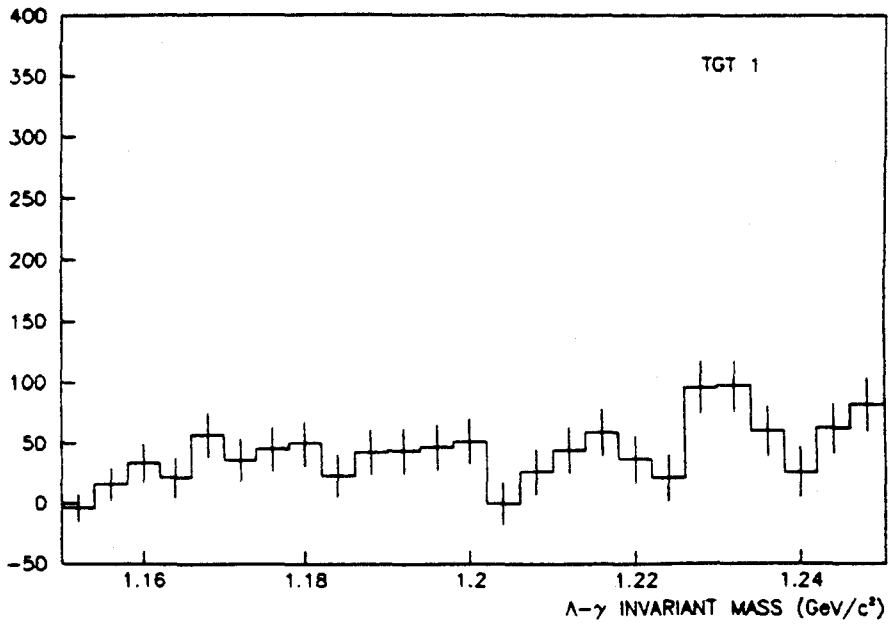

Figure 4.12 The ΛΥ invariant mass distribution with $Q^2 < 0.004$ for the air target. The fitted input distributions (except for the Σ^0_{Pk} and Σ^0_{str} Monte Carlos) have been subtracted from the data.

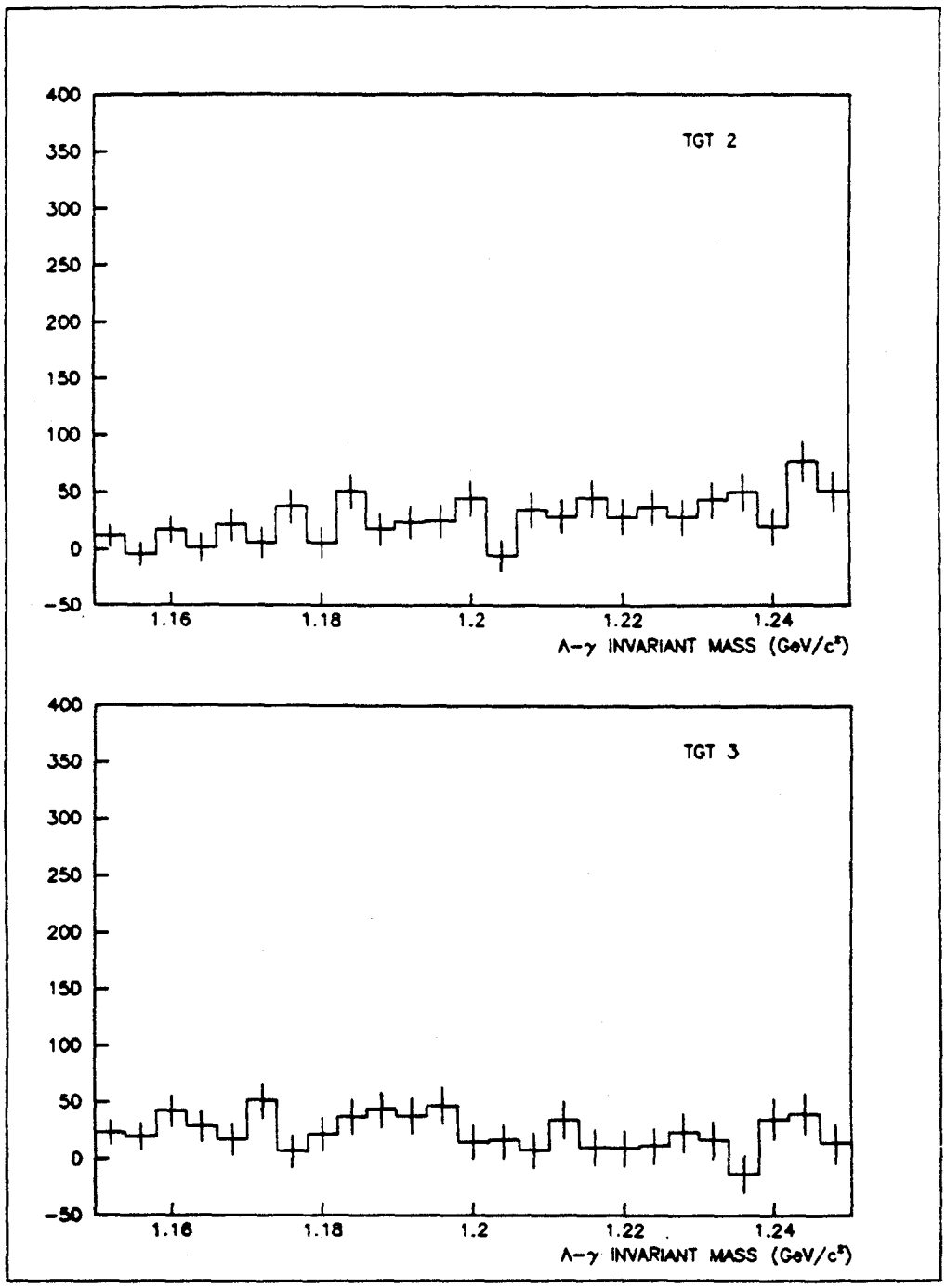

Figure 4.13 The ΛΥ invariant mass distribution with $Q^2 < 0.004$ for the beryllium targets. The fitted input distributions (except for the Σ^0_{Pk} and Σ^0_{str} Monte Carlos) have been subtracted from the data.

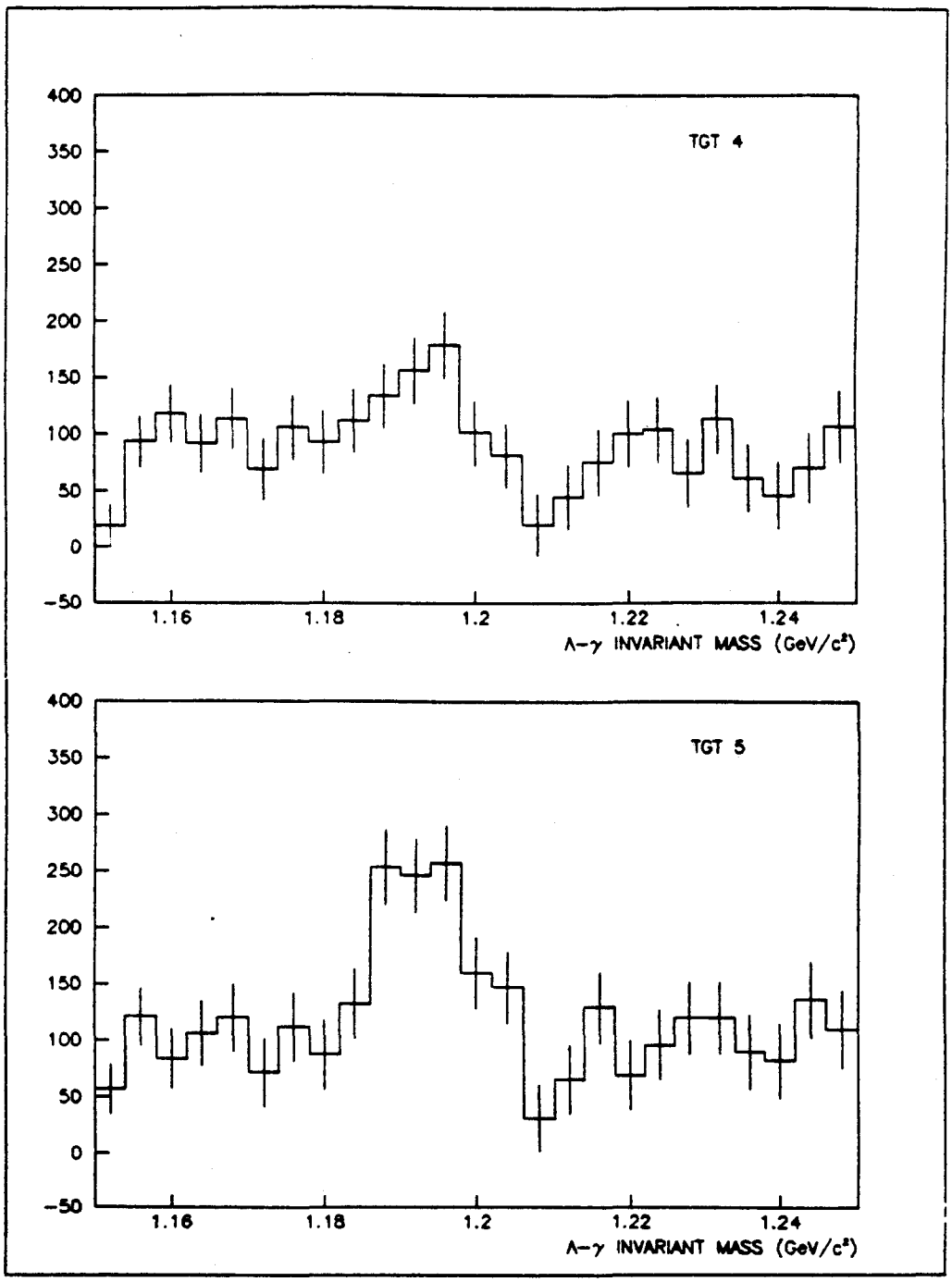

Figure 4.14 The ΛΥ invariant mass distribution with $Q^2 < 0.004$ for the tin targets. The fitted input distributions (except for the Σ^0_{Pk} and Σ^0_{str} Monte Carlos) have been subtracted from the data.

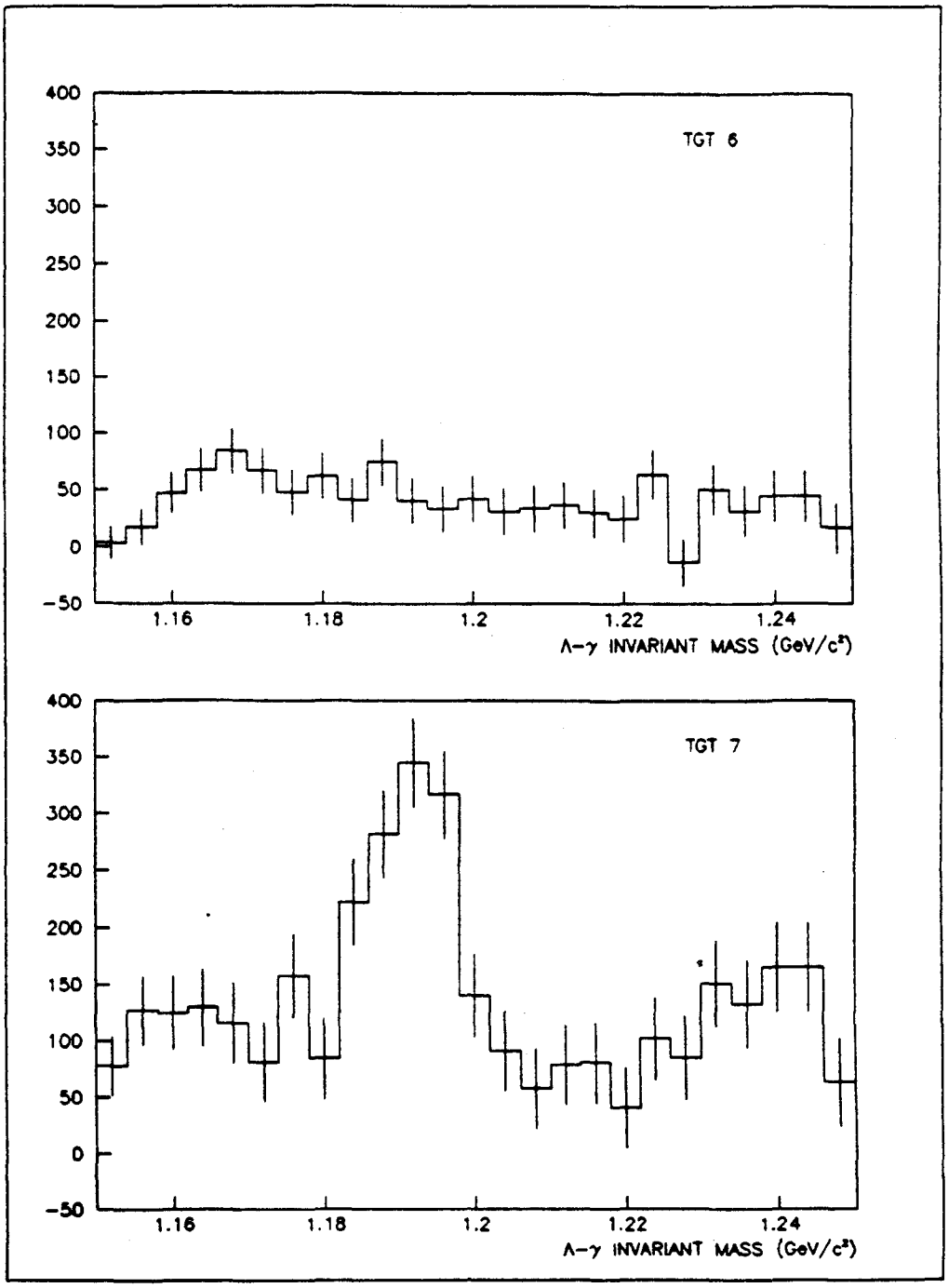

Figure 4.15 The ΛΥ invariant mass distribution with $Q^2 < 0.004$ for the lead targets. The fitted input distributions (except for the Σ^0_{Pk} and Σ^0_{str} Monte Carlos) have been subtracted from the data.

Table 4.3

Results of Global Fit

Target	χ^2 / d.f.	No. of Fitted Events from each Population
1	940 / 630	Σ°(Pk) = 106 ± 44
		Σ°(st) = -50 ± 571
		$\Lambda\Upsilon$ = 5333 ± 165
		Ξ° = 24207 ± 411
2	617 / 567	Σ°(Pk) = -10 ± 34
		Σ°(st) = 1325 ± 534
		$\Lambda\Upsilon$ = 3345 ± 133
		Ξ° = 15560 ± 450
3	817 / 600	Σ°(Pk) = 138 ± 39
		Σ°(st) = -421 ± 500
		$\Lambda\Upsilon$ = 3131 ± 130
		Ξ° = 18978 ± 345
4	1241 / 649	Σ°(Pk) = 564 ± 71
		Σ°(st) = 950 ± 987
		$\Lambda\Upsilon$ = 10329 ± 254
		Ξ° = 51727 ± 643
5	1234 / 631	Σ°(Pk) = 706 ± 79
		Σ°(st) = 4385 ± 1145
		$\Lambda\Upsilon$ = 12713 ± 287
		Ξ° = 58292 ± 717
6	1009 / 623	Σ°(Pk) = 131 ± 48
		Σ°(st) = -425 ± 660
		$\Lambda\Upsilon$ = 6111 ± 182
		Ξ° = 28944 ± 446
7	1352 / 648	Σ°(Pk) = 845 ± 93
		Σ°(st) = 3249 ± 1308
		$\Lambda\Upsilon$ = 17165 ± 347
		Ξ° = 77356 ± 829

Table 4.4

Invariant Mass Fit

Target	$\frac{\chi^2}{d.f.}$	No. of Σ^0 Events
1	$\frac{15.0}{9}$	9 ± 41
2	$\frac{3.5}{9}$	53 ± 33
3	$\frac{8.3}{9}$	53 ± 36
4	$\frac{19.4}{8}$	266 ± 60
5	$\frac{10.2}{8}$	621 ± 65
6	$\frac{22.8}{9}$	64 ± 44
7	$\frac{17.4}{8}$	887 ± 76

The wings of the $M_{\Lambda\gamma}$ distribution for data-background were fitted to a polynomial. A linear fit was used for the target samples with low statistics and a quadratic fit was used for targets 4, 5 and 7. The fit was subtracted from the number of events in the mass peak. Table 4.4 lists the number of Σ°'s in each target sample and the χ^2/d.f. of the fit to the secondary background.

4.3 Strong Production of Σ°s

The Σ°'s produced by strong interactions are also a small, highly localized population. Thus, the global fit is probably not very reliable at determining their relative proportion in the data sample. Indeed, three of the target data sets with low statistics show a negative contribution from this source. This section describes an attempt to gain an independent understanding of the magnitude of the strongly-produced Σ° background.

The non-Σ° background at $Q^2 > 0.1$ is very small and essentially flat in the invariant mass. At these high Q^2 values, any possible forward-peaked component is absent. The $\Lambda\gamma$ invariant mass for $Q^2 > 0.1$ is plotted in Figs 4.16-4.19 for each target, and the number of Σ°'s after background subtraction is listed in Table 4.5. These numbers can be

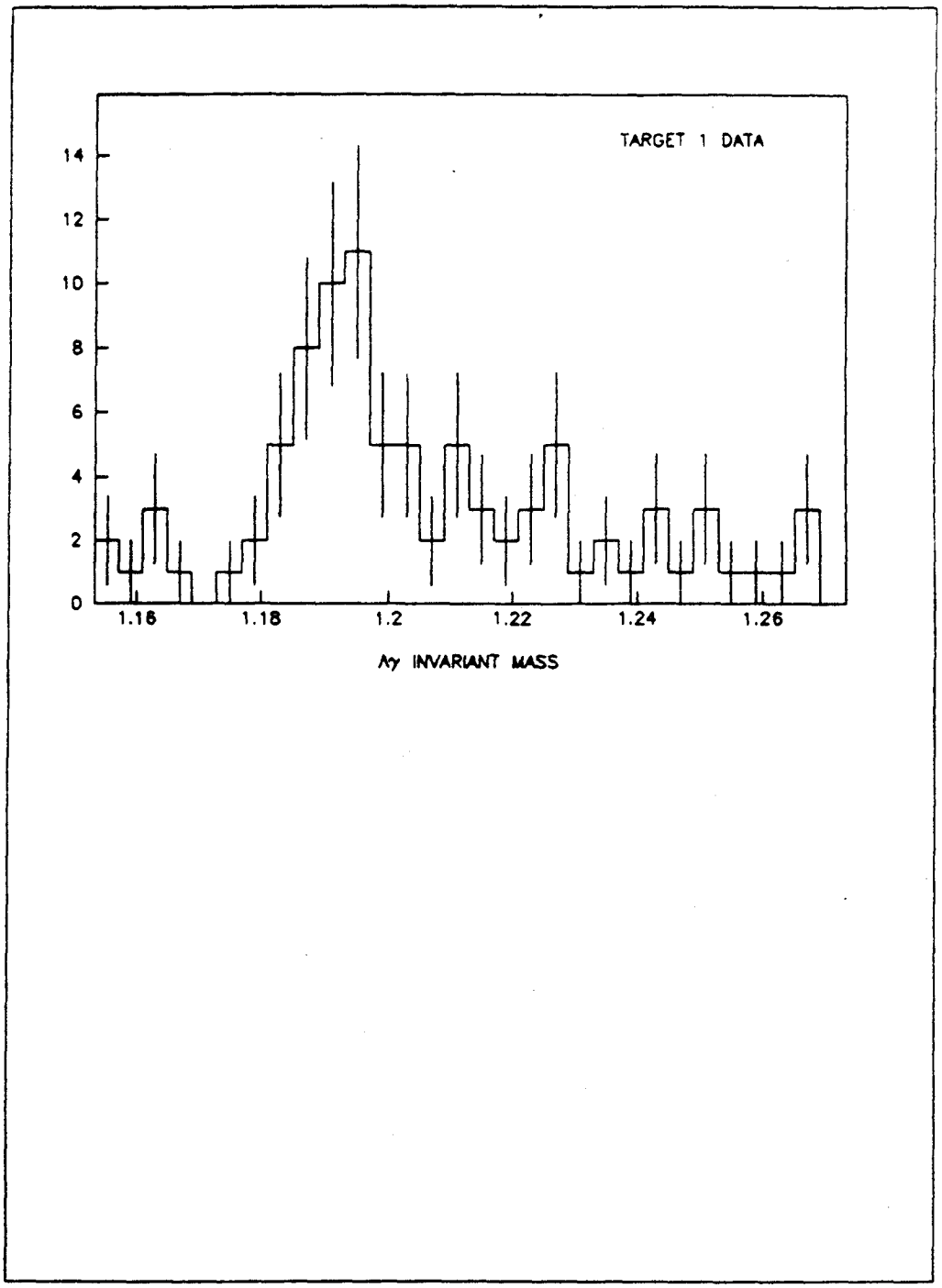

Figure 4.16 The ΛΥ invariant mass distribution with $Q^2 > 0.1$ for the air target.

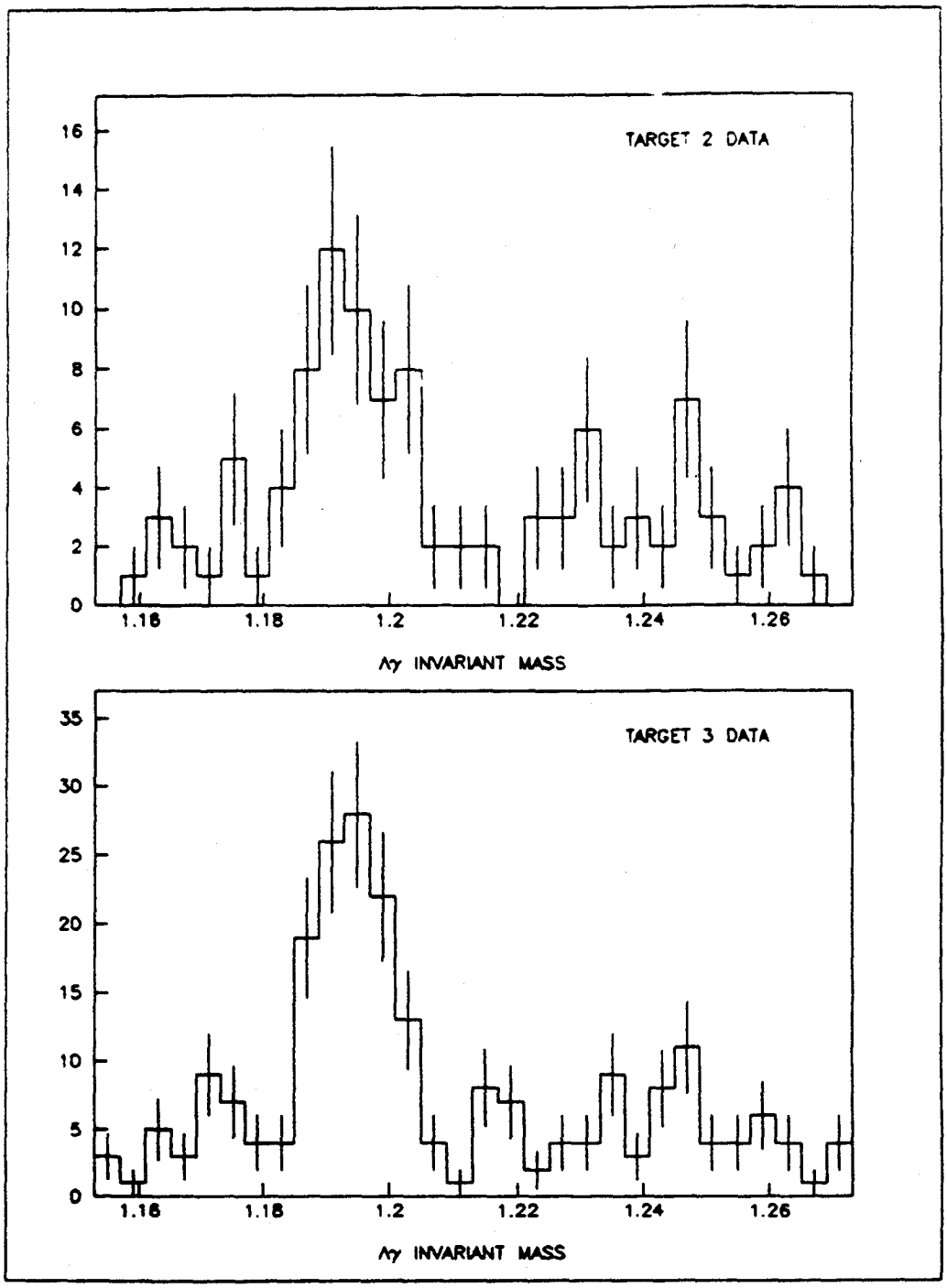

Figure 4.17 The ΛΥ invariant mass distribution with $Q^2 > 0.1$ for the berylium targets.

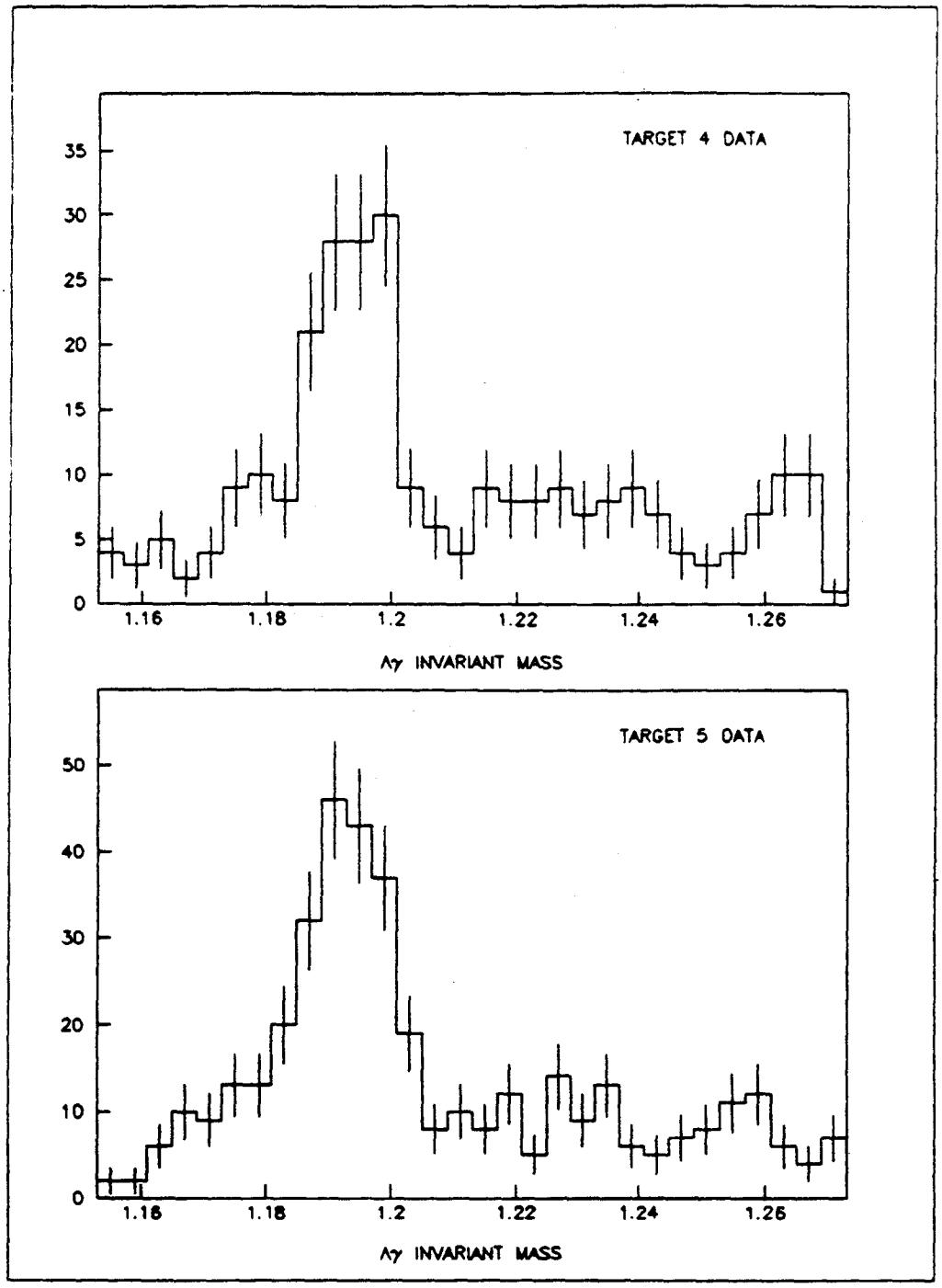

Figure 4.18 The ΛΥ invariant mass distribution with $Q^2 > 0.1$ for the tin targets.

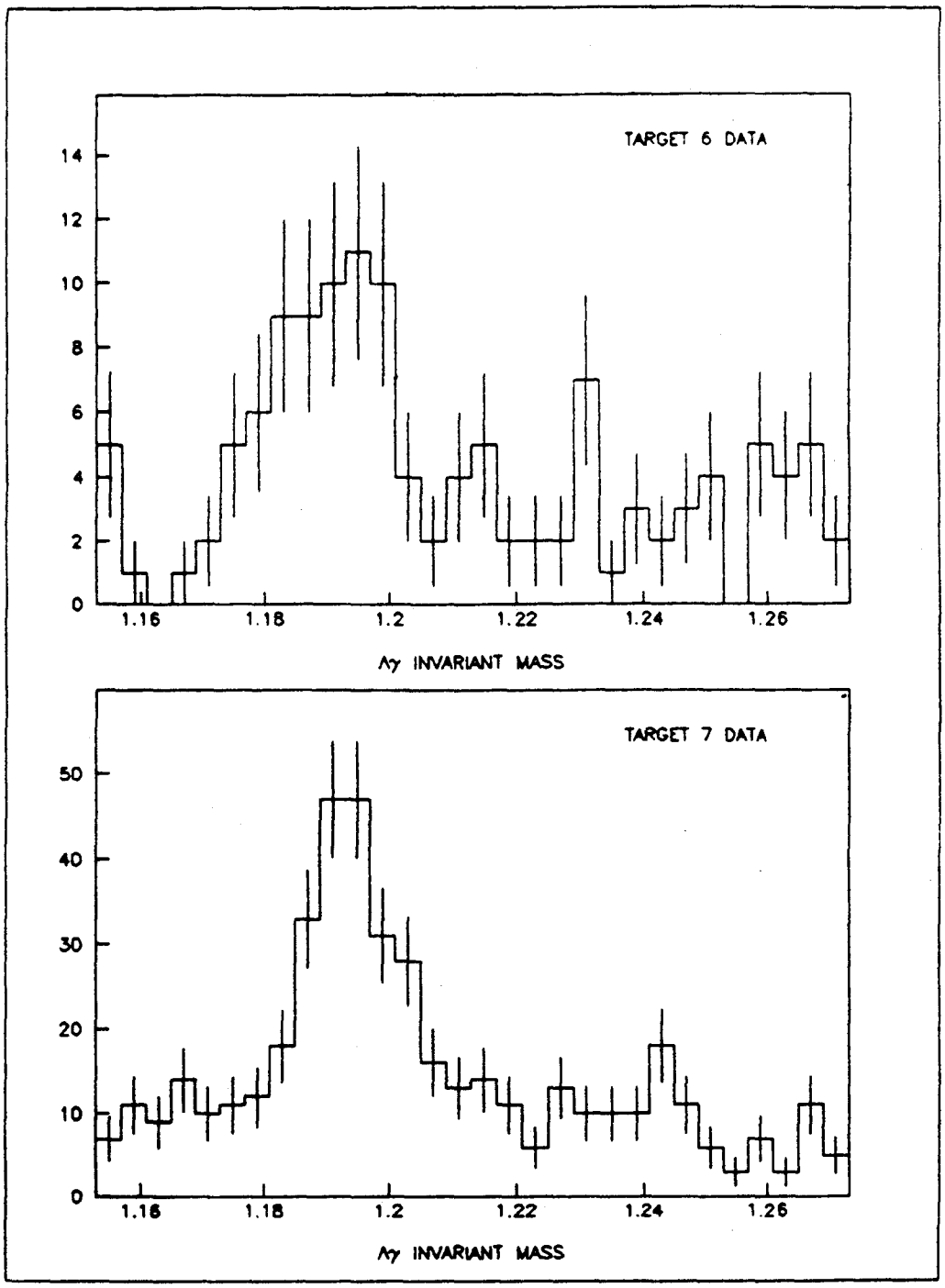

Figure 4.19 The ΛΥ invariant mass distribution with $Q^2 > 0.1$ for the lead targets.

Table 4.5

Strong Production of Σ^{o}'s

Target	no. of strong Σ^{o}'s ($Q^2>0.1$)	$\frac{N(\Sigma)(Q^2>0.1)}{N(\Lambda)}$ ($\times 10^{-6}$)	M.C. Assumes e^{-10Q^2} dependence Acceptance is also a function of Q^2			
			total no. of strong Σ^{o}'s	no. of strong Σ^{o}'s (± 2) ($Q^2<0.004$)	Partial cross section (mb)	$\frac{\sigma}{A^{\frac{2}{3}}}$
1	23±5	1.8±0.4	99	6	--	--
2	27±5	2.9±0.5	117	6	0.37±0.07	0.08±0.01
3	83±9	8.5±0.9	358	20	0.31±0.03	0.07±0.01
4	74±8	3.0±0.3	319	18	2.1±0.2	0.08±0.01
5	143±12	5.2±0.4	616	36	2.4±0.2	0.09±0.01
6	31±6	2.3±0.4	134	8	4.7±0.9	0.13±0.02
7	140±12	4.0±0.3	603	36	3.8±0.3	0.10±0.01

normalized to the number of beam Λ's, corrected for the target self-veto effect, and plotted with respect to the number of absorption lengths in the beam. Two Primakoff veto counters, three upstream scintillation counters, and four meters of air combine to give 0.037 absorption lengths of non-target material which must be added to the target absorption lengths found in Table 2.1. The obvious proportionality displayed in Fig 4.20 is a good indication that the Σ°'s are produced by the strong interaction.

From the Σ°_{str} Monte Carlo, the number of strongly-produced Σ°'s over the whole Q range can be estimated. A partial cross section of the order of millibarns for Σ°'s strongly-produced by the target can be obtained by first multiplying $N(\Sigma)_{str}/N(\Lambda)$ by $L_{abs}(target)/L_{abs}(total)$ and then converting to $\sigma(\Sigma^\circ)_{str}$ using Eq. 4.2. Although it is unclear how to interpret a cross section for totally neutral final state Σ° production (by some poorly known combination of Λ's and neutrons); it is heartening to note that the cross sections do have the roughly $A^{\frac{2}{3}}$ dependence previously noted in the L_{abs} proportionality.

The Σ°_{str} Monte Carlo can be used to estimate the number of strongly-produced Σ°'s under the $Q^2 < 0.004$ Σ° mass peak from the number found at $Q^2 > 0.1$. These numbers, also listed

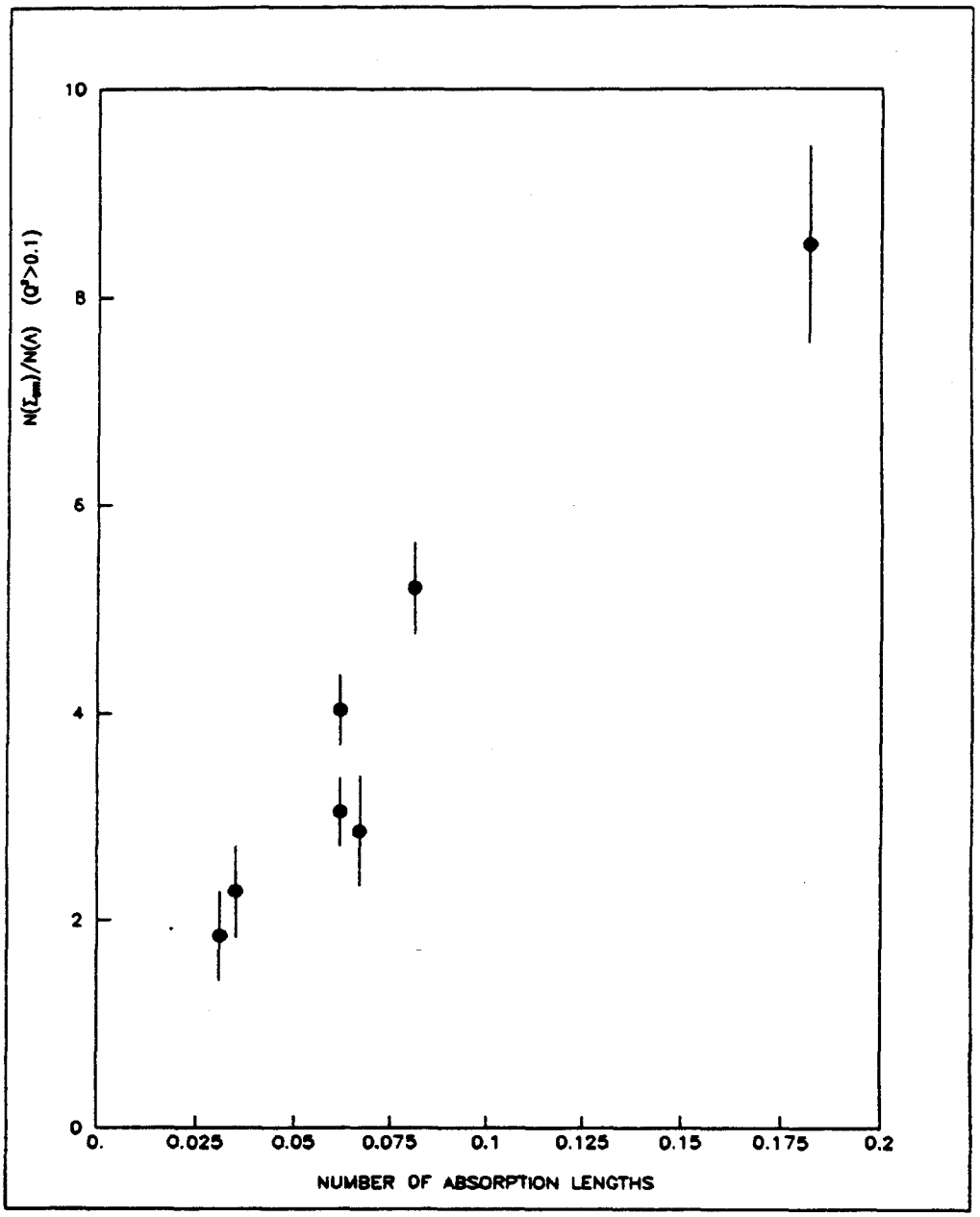

Figure 4.20 The number of Σ^0's with $Q^2 > 0.1$ (incoherent strong production), normalized to the number of beam Λ's, and plotted with respect to the total number of absorption lengths of material between counters S1 and S2.

in Table 4.5, represent a lower limit to the strong contamination of the Coulomb signal and were subtracted.

4.4 Subtraction of Non-target Primakoff Σ^os

Besides the Primakoff target, there were four meters of air and 5 scintillation counters (4 after tape FE2373) upstream of the decay region. The extra 0.079 radiation lengths of material can produce Σ^o's by the Primakoff effect. The number of Σ^o's which can be Coulomb-produced by this material is proportional to $\sum_i \frac{\rho_i}{A_i} L_i G_i Z_i$ where Z_i = the radiation length, ρ_i = density, and A_i = atomic number. The sum runs over non-target elements in the beam. $G_i = \frac{9}{7} X_i \, (1-e^{-\frac{7}{9}X_i})$ where X_i = number of radiation lengths in an element of length L_i, accounts for vetoing of the event due to pair production in the extra material. An additional suppression factor of $e^{-\frac{7}{9}X_t}$ (pair production in the target) must also be applied to all Σ^o production upstream of the target.

This proportionality (without the $e^{-\frac{7}{9}X_t}$ factor) is also valid for Σ^o's Coulomb-produced by the target. It therefore provides a means of calculating the percentage of the Primakoff signal which is due to the target material alone. As can be seen in Table 4.6, this represents a sizeable correction for the short targets.

Table 4.6

Non-Target Coulomb Production

Target	$\frac{N(tgt)}{N(\Lambda)}$ [a]	$\frac{N(non\text{-}tgt)}{N(\Lambda)}$ [a]	$\frac{N(tgt)/N(\Lambda)}{N(total)/N(\Lambda)}$ [b]
1	0.0	10.24	0.00
2	3.63	10.44	0.26
3	16.52	9.34	0.64
4	86.2	6.70	0.93
5	129.3	4.77	0.96
6	28.5	9.23	0.76
7	143.5	4.81	0.97

Notes: (a) Estimate 5% uncertainty

(b) Estimate 7% uncertainty

4.5 Beam Λ Normalization

Determining the number of beam Λ's is a much simpler task. It is not, however, quite as simple as counting the number of prescaled Λ' triggers because these triggers were a mixture of beam Λ's, Ξ^0 daughters, and scattered Λ's. In order to determine the relative proportions of each sample, a stripped-down version of the multi-dimensional χ^2 fitting program was used. A cut on $r^2_{prod}(\Lambda) < 20$ mm^2 effectively removed the scattered Λ contribution. Thus only two input populations, the Λ_B Monte Carlo and the Ξ^0 Monte Carlo, were used. The variables with the most distinguishing power were $r^2_{prod}(\Lambda)$ and the z vertex of the Λ decay.

The fitting procedure yielded the fraction of beam Λ's in those Λ' triggers with $r^2_{prod}(\Lambda) < 20$ mm^2. This number was multiplied by the total number of low $r^2_{prod}(\Lambda)$ prescaled Λ' triggers to give the total number of beam Λ's with $r^2_{prod}(\Lambda) < 20$ mm^2. It was then adjusted for the full $r^2_{prod}(\Lambda)$ range by consulting the Λ_B Monte Carlo distribution to give the $N(\Lambda)$ term in Eq. 4.2. All pertinant numbers are multiplied by the appropriate prescale factor, and listed by target in Table 4.7. On average, the reconstructed Λ's from the Λ' trigger were 91% beam Λ's.

Table 4.7

Beam Λ Normalization

Target	Reconstructed Λ's in Λ' Trigger after "Λ" Cuts ($\times 10^7$)	From Fit: Beam Λ's with $r^2_{prod}(\Lambda) < 20\ mm^2$ ($\times 10^7$)	$f \cdot N(\Lambda)$ ($\times 10^7$)
1	1.360	1.142	1.255
2	1.050	0.876	0.965
3	1.163	0.953	1.046
4	3.351	2.774	3.044
5	4.404	3.634	3.993
6	1.602	1.322	1.453
7	5.537	4.594	5.044

Note: Systematic error due to fitting procedure is 1.2%

4.6 Cross Section Calculation

The value for $N(\Sigma^\circ)/N(\Lambda)$ was extracted from the data for each target in the following way. The strongly-produced Σ° background from Table 4.5 was subtracted from the number of Σ°'s found in Table 4.4. The resulting number was multiplied by the correction factor in the third column of Table 4.6 to get the number of Σ°'s with $Q^2 < 0.004$ which were Coulomb-produced by the target. The Σ°_{Pk} Monte Carlo (with corrections for target dependent resolution) was then used to convert this number to $N(\Sigma^\circ)$, the number of Σ°'s expected for all Q. The Monte Carlo used in the fitting procedure included Primakoff production from the extra upstream sources, but the Monte Carlo used to convert from narrow to full Q range was for target production alone. $N(\Sigma^\circ)$ was then normalized by the number of beam Λ's, $N(\Lambda)$. The $\sigma(\Sigma^\circ)_{Pk}$ cross section was obtained from equation 4.2. These cross sections are expected to be a roughly linear function of Z^2. Table 4.8 and Fig 4.21 show that this is indeed the case. The weighted averages of the cross sections for the three materials used in this experiment are $\sigma_{Be} = 0.033 \pm 0.022$ mb, $\sigma_{Sn} = 3.28 \pm 0.34$ mb, and $\sigma_{Pb} = 9.20 \pm 0.81$ mb.

Table 4.8

Cross Section and Magnetic Moment

Target	$N(\Sigma^\circ)$	$\sigma(\Sigma^\circ)_{Pk}$ (a) in mbarns	$\mu^2_{\Sigma\Lambda}$ (b) (nuclear magnetons)^2
2	15 ± 10	0.068 ± 0.048	6.50 ± 4.58
3	24 ± 27	0.023 ± 0.025	2.20 ± 2.39
4	271 ± 66	2.65 ± 0.64	1.95 ± 0.47
5	701 ± 73	3.48 ± 0.36	2.56 ± 0.27
6	49 ± 39	8.17 ± 6.45	2.34 ± 1.85
7	968 ± 86	9.22 ± 0.82	2.64 ± 0.24

Note: (a) In addition to the quoted statistical uncertainties, there is a correlated systematic uncertainty of 7%.

(b) A 5% systematic uncertainty in the Primakoff formalism applies, in addition to the 7% systematic uncertainty in the analysis.

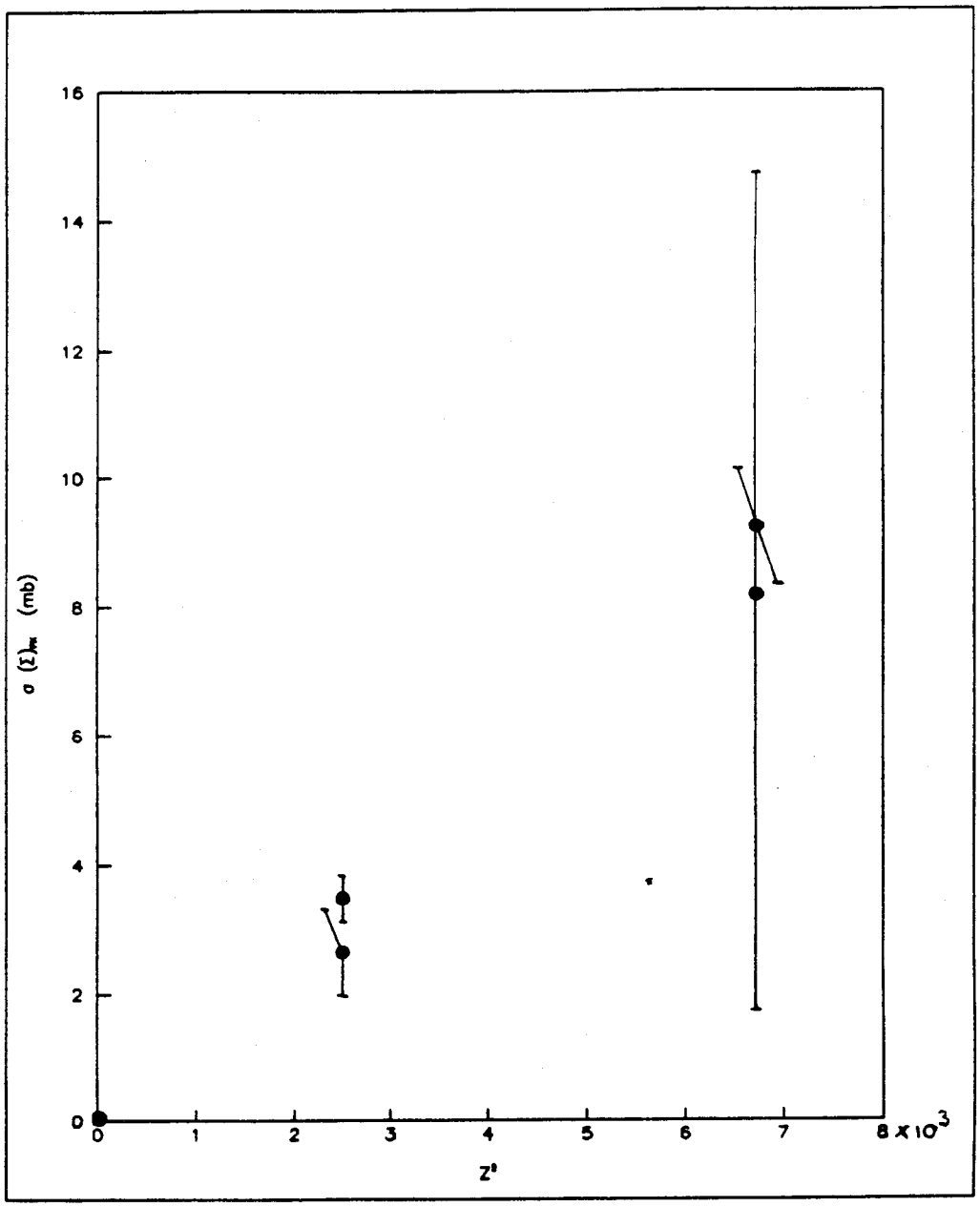

Figure 4.21 The experimental cross section for Coulomb-produced Σ^0's as a function of the square of the target atomic number.

4.7 Systematic Uncertainties

All the uncertainties quoted thus far have been statistical in origin. It still remains to estimate the possible error due to systematic effects. The uncertainties in the denominator of the cross section formula (see Eq. 4.2) are purely systematic, since the statistical uncertainty on 10^7 beam Λ's is negligible. The quoted uncertainties on the four ε_i's are combined with an estimated uncertainty of 1.2% from the beam Λ fitting procedure to yield a 4.5% systematic uncertainty for each target.

The numerator, $N(\Sigma^\circ)$, is stable within the assigned statistical limits against changes in the range and choice of variables in the global fit. However, the shape of the Q^2 distribution between $0.0 < Q^2 < 0.004$ for the extracted Σ°_{Pk} peak is broader for the data than the Monte Carlo. Three effects determine the shape of the Q^2-dependence of the Σ° population at low Q^2: Primakoff Σ° production, possible forward-peaked strong Σ° production, and the resolving power of the experiment. Primakoff production at energies ~150 GeV is very sharply peaked in the vicinity of $Q^2 \sim 10^{-6}$ GeV^2 (Q_{rms} = 1 MeV), and is broadened by the experimental resolution to $Q^2 \sim 0.0014$ GeV^2 (Q_{rms} = 37 MeV).

The normalized sample of Monte Carlo Σ^o's with all known experimental effects was compared with the background-subtracted Σ^o data in the Q^2 variable. Although they agree qualitatively, a quantitative comparison of the bins $0 < Q^2 < 0.002$ GeV^2 and $0.002 < Q^2 < 0.004$ GeV^2 show a marginally significant discrepancy for the two target sets with sufficient data for the comparison (tgts 5 and 7). Either of two effects could explain the discrepancy: the presence of a forward-peaked strongly-produced Σ^o background or a slight disagreement between the Monte Carlo Q^2 resolution and the true Q^2 resolution.

Coherent processes such as elastic scattering, can be very sharply peaked in the forward direction. A true coherent process requires that there be no change in quantum numbers. Since the production of a Σ^o from a Λ changes isospin by one, coherent strong production is expressly forbidden. One can envision a "quasi-coherent" process in which a relatively low-mass state, forward-produced by either neutrons or Λ's, decays into a Σ^o and other neutral particles. Since the Q^2 dependence of the incoherent production is based on data at relatively large Q^2 (the data doesn't become manageable until $Q^2 > 0.02$), there is the possibility that some quasi-coherent process contributes to the Σ^o signal in the mid-Q^2 range. To estimate the magnitude of this contribution, the invariant mass was examined in the

region $0.002 < Q^2 < 0.008$. Assuming a Q^2 dependence of e^{-100Q^2} for the quasi-coherent Σ^o's gave an upper limit of 70 ± 50 such events in the $Q^2 < 0.004$ region. If strong production of Σ^o's is responsible for the Q^2 mismatch, then the number of Coulomb-produced Σ^o's in the target 7 sample should be <u>reduced</u> by 6%.

The discrepancy could also be caused by an error in the width of the Q^2 distribution from the Σ^o_{Pk} Monte Carlo. Assuming that the spectrometer acceptance is flat in this region and that only the experimental resolution contributes to the width, the shape of the Q^2 distribution can be approximated by a Gaussian, e^{-aQ^2}. Then the discrepancy in Q^2 corresponds to a difference in the widths of the distributions of Q_{rms}=37 MeV/c for the Σ^o_{Pk} Monte Carlo and Q_{rms}=39 MeV/c for the data. This is not an unreasonable error. The error introduced into the answer, however, will depend on the size of the Q^2 bin within which the Primakoff signal is evaluated since the Σ^o_{Pk} Monte Carlo is used to correct $N(\Sigma^o)$ to the full Q^2 range. This Monte Carlo correction factor is 1.45 for $N(\Sigma^o)$ evaluated for $Q^2 < 0.002$ and 1.17 for $N(\Sigma^o)$ with $Q^2 < 0.004$. If the mismatch in Q^2 is due to an underestimated experimental resolution, then the number of Coulomb-produced Σ^o's in the target 7 sample should be <u>increased</u> by 10% or 5% for the two choices respectively. Obviously, the looser Q^2 cut is preferable for this reason.

No evidence exists to choose between these two possibilities, which would revise the result in opposite directions by roughly similar amounts. The same effect can be observed in the other high statistics data sample (tgt 5), but at a slightly lower level. Since this is presumed to be a correlated systematic effect, an average uncertainty of 5% was assigned to all targets. The uncertainties in numerator and denominator were added in quadrature to give a correlated systematic uncertainty of 6.7%.

CHAPTER 5

Results and Conclusions

5.1 Introduction

The Primakoff formalism yields an equation for $\frac{d\sigma}{dq^2}$ as a function of the square of the magnetic moment (see Eq. 1.1), and thus provides a means of determining $\mu_{\Sigma\Lambda}$ from the measured $\sigma(\Sigma^\circ)_{Pk}$. The differential cross section relation comes from the fact that the electromagnetic matrix elements for both $\Sigma^\circ \rightarrow \Lambda\gamma$ and $\Lambda+Z \rightarrow \Sigma^\circ$ processes are analogous except for a source term: the Coulomb field of virtual photons. In the limit of forward $\Lambda \rightarrow \Sigma^\circ$ conversion and high energy incident Λ's, the source term becomes less important and the momentum terms simplify. Thus, the derivation of Eq. 1.1 requires no ingredients other than QED and matrix algebra. This is not true for the total cross section which requires

an explicit model for the nuclear form factor, $F(q^2)$. In the following analysis, a semi-empirical $\overline{F}_Z$ is obtained for each target, the Z^2 dependence is factored out, and $\mu^2_{\Sigma\Lambda}$ is calculated for each target.

5.2 Nuclear Absorption Correction

In equation 1.2 a black sphere approximation to $F(q^2)$ enabled one to write an analytic expression for $\sigma(\Sigma^\circ)_{Pk}$. A better approach is to use a complete optical model and do a numeric integration. A program developed by Colin Wilkin[15] uses a parametrization of $F(q^2)$ derived from electron-nuclear elastic scattering data and takes account of the absorption of both incoming and outgoing hyperons. This program was used to find the degree of absorption expected for the three target materials. Included in the input parameters were the Σ° lifetime, incident Λ momentum, and the nucleon-hyperon cross section. The program was run for an ensemble of incident momenta weighted according to the experimental Λ momentum spectrum. A Λp total cross section of $\sigma_{\Lambda p} = 35.5 \pm 1.0$ mb comes from unpublished Fermilab data[16] at 200 GeV, and is consistent with CERN hyperon data at 20 Gev[17]. The uncertainty in $\sigma_{\Lambda p}$ corresponds to only a 0.2% change in the calculated Primakoff cross section.

The total cross section can now be written

$$\sigma_{Pk}(\Sigma\Lambda) = 63.2\left(\frac{\mu_{\Sigma\Lambda}}{\mu_N}\right)^2\left(\frac{Z}{82}\right)^2 \overline{F}_Z = K_Z\left(\frac{\mu_{\Sigma\Lambda}}{\mu_N}\right)^2 Z^2 \quad \text{mb} \qquad (5)$$

$\overline{F}_Z$ is the result of integrating $F^2(q^2)$ over q^2 and averaging over incident p_Λ. Absorbing the numerical factors gives constants of proportionality $K_{Be} = 6.542 \times 10^{-4}$, $K_{Sn} = 5.444 \times 10^{-4}$, and $K_{Pb} = 5.187 \times 10^{-4}$. The percentage change in the cross section due to the inclusion of absorption effects is 1.4%, 9.2%, and 11.9% for beryllium, tin, and lead respectively. The model is estimated to be accurate to less than 5%, comparable to most estimates of the accuracy of the Primakoff formalism itself. This theoretical uncertainty is quoted as a separate systematic error on the derived quantities: $<$ 5% on τ and Γ, $<$ 2.5% on $|\mu_{\Sigma\Lambda}|$.

5.3 Electron Screening

It is a feature of the Primakoff cross section that the momentum transfer, q_t^2, decreases (or equivalently the impact parameter increases) as the energy increases. When $1/q_t$ approaches atomic dimensions, some correction for electron shielding of the Coulomb field must be taken into account. An estimate of the percentage change in cross section induced by screening is calculated following the treatment of Fäldt et al.[8] Replacing the form factor $F(q^2)$ in equation 1.1 by

$(F_n - F_e)$, and remembering that in the interaction range where F_e is significant, $F_n \sim 1$, we get $F_{tot}^2 = F_n^2 - (2F_e - F_e^2)$. Fäldt then determines an empirical formula for $F_e(q^2)$, inserts it in the cross section expression, and integrates over all values of the momentum transfer. In terms of the variables used in this paper, the change in cross section can be written

$$\Delta\sigma = 0.496\left(\frac{Z}{82}\right)^2\left(\frac{\mu_{\Sigma\Lambda}}{\mu_N}\right)^2 \{0.508\tau_{min}^{-\frac{1}{4}} - [1 - 0.156\tau_{min}^{-\frac{1}{4}} - 0.176\tau_{min}^{-1}]\}$$

where $\tau = 10^{19} Z^{-\frac{2}{3}} q^2$ (dimensionless when q^2 is in units of $(GeV/c)^2$) and $\tau_{min} = \tau(q^2)$ evaluated at $q_t^2 = q_l^2$. Most of the Coulomb production occurs at $q_t = q_l = (m_{\Sigma^0}^2 - m_\Lambda^2)/2p_\Lambda$ which corresponds to a 0.6 MeV virtual photon at $p_\Lambda = 150$ GeV/c. Assuming $\mu_{\Sigma\Lambda}/\mu_N = 1.6$ and plugging in the appropriate values for τ_{min} gives $\Delta\sigma = 6.5\times10^{-6}$ mb, 3.7×10^{-3} mb, and 1.3×10^{-2} mb for beryllium, tin, and lead respectively. The correction in beryllium is completely negligible. However, even for lead, $\Delta\sigma$ is only 0.16% of the Primakoff cross section. Since this is a tenth of the uncertainty assigned to the lead cross section determination, electron screening was ignored in the final magnetic moment analysis. It should be noted, however, that the problem gets more serious for higher energy Λ beams (see Fig 1.1 for details).

5.4 Transition Magnetic Moment

Eq. 5.1 can be inverted to give

$$\left(\frac{\mu_{\Sigma\Lambda}}{\mu_N}\right)^2 = \frac{\sigma(\Sigma^0)}{K_Z\ Z^2}Pk$$

The calculation was done individually for the six non-empty targets and then averaged with the appropriate weights to yield $(\mu_{\Sigma\Lambda}/\mu_N)^2 = 2.53 \pm 0.17 \pm 0.17$ (refer to Table 4.8 and Fig 5.1). This is algebraically identical to performing a least squares fit to the line $\sigma_{Pk}/K_Z = aZ^2+b$ where b is constrained to zero and $a=(\mu_{\Sigma\Lambda}/\mu_N)^2$. Taking the square root gives a final answer of $|\mu_{\Sigma\Lambda}| = 1.59 \pm 0.05 \pm 0.5$ nuclear magnetons (n.m.). Although this experiment did not measure the sign of the moment, we assume that it has a negative value consistent with the SU(6) prediction.

The lifetime and decay width come from Fermi's Golden Rule for M1 transitions using relativistic Dirac spinors[5] rather than the Schrödinger-Pauli approximation: $\Gamma = \tau^{-1} = 4\mu^2_{\Sigma\Lambda}k^3$ in natural units, where k is the momentum of the decay photon, $kc = (m_{\Sigma^0}^2 - m_\Lambda^2)/2m_{\Sigma^0} = 74.4$ MeV. Putting in all the necessary factors gives

$$\Gamma = 4\left(\frac{\mu_{\Sigma\Lambda}}{\mu_N}\right)^2\left(\frac{e\hbar}{2m_pc}\right)^2 k^3 = \left(\frac{\mu_{\Sigma\Lambda}}{\mu_N}\right)^2 \frac{\alpha\ k^3}{m_p^2} = (8.6 \pm 0.6 \pm 0.6)\ \text{keV}$$

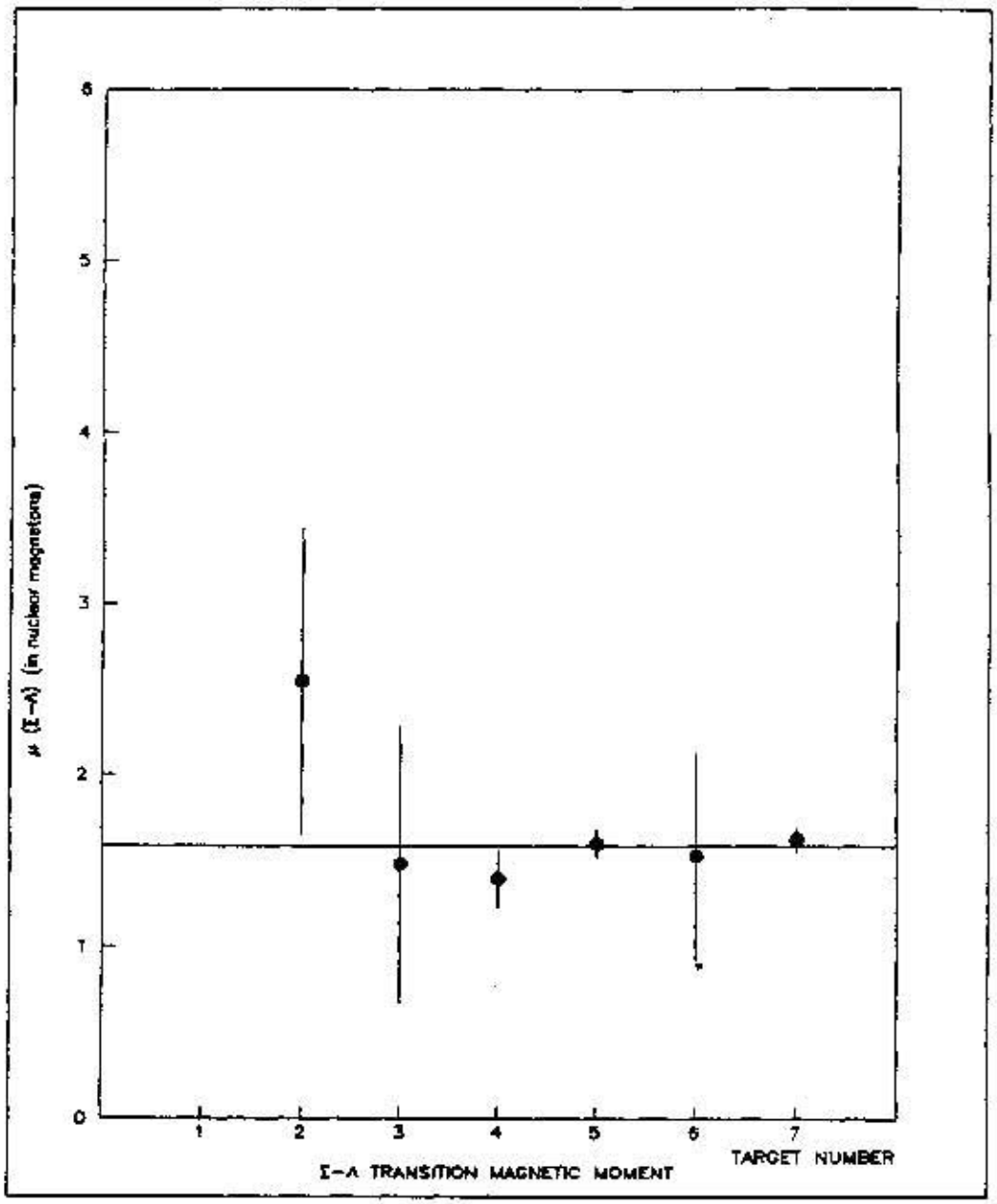

Figure 5.1 The Σ^0-Λ transition magnetic moment determined separately for the various Primakoff targets. The line represents the root mean square, $\mu_{\Sigma\Lambda} = 1.60 \pm 0.05$ n.m., where the uncertainty is statistical only.

This corresponds to a lifetime of

$$\tau = (1.929 \times 10^{-19}\ \text{sec}) \left(\frac{\mu_{\Sigma\Lambda}}{\mu_N}\right)^{-2} = (0.76 \pm 0.05 \pm 0.05) \times 10^{-19}\ \text{sec.}$$

5.5 Comparison with Previous Experiment

A previous experiment by Dydak et al.[18] at the CERN Proton Synchrotron has also measured the Σ^0-Λ transition moment. They reported a value of $|\mu_{\Sigma\Lambda}| = 1.82\ ^{+0.25}_{-0.18}$ n.m. using the Primakoff method and a similar apparatus. This value has been revised by changing the order in which reciprocals and weighted averages were performed, and correcting for an approximation made in the original Dreitlein and Primakoff paper.[6] See Appendix B for the details. The revised value of $|\mu_{\Sigma\Lambda}| = 1.75\ ^{+0.18}_{-0.20}$ is consistent with the value reported by this paper, but the uncertainty has been more than halved. This is partly due to statistics since the final E619 sample contained 2028 ± 139 Primakoff Σ^0's compared to 357 ± 55 at CERN. On the other hand, Dydak et al. had a better signal/background ratio. In the $Q^2 < 0.001\ (\text{GeV/c})^2$ region after a mass cut of $1.175 < M_{\Lambda\gamma} < 1.205$ GeV/c², their signal/background ratio was 1:2 for both uranium and nickle data, while this experiment was closer to 1:6 for target 7 data after similar cuts.

The CERN experiment ran at an average neutral beam enery of 15 GeV, a factor of 10 lower than the Fermilab neutral beam. The higher Fermilab energy conferred a distinct advantage since the impact parameter increases with energy. Thus, at Fermilab energies the interaction took place further from the nucleus, and corrections for nuclear absorption were consequently smaller. A 34% correction was required for the CERN experiment compared with the 12% for lead reported here.

5.6 Comparison with Theory

The experimental results can be compared to several theoretical models. Sum rules derived from SU(3) x SU(2) group symmetries[2] provide a fairly simple procedure for calculating the Σ^0-Λ transition moment, as well as the other static moments. Assuming the baryons are s-wave states of three non-relativistic quarks, antisymmetry in color and symmetry in spin, space, and flavor enable one to write the wavefunctions for Σ^0 and Λ as

$$|\Sigma^0\rangle = \sqrt{\tfrac{2}{3}}\, u\uparrow d\uparrow s\uparrow - \sqrt{\tfrac{1}{3}}\left[\sqrt{\tfrac{1}{2}}(u\uparrow d\uparrow + u\uparrow d\uparrow)s\uparrow\right]$$

$$|\Lambda\rangle = \sqrt{\tfrac{1}{2}}(u\uparrow d\uparrow - u\uparrow d\uparrow)s\uparrow$$

where $u\uparrow$, for example, is the wavefunction for a spin-up u quark. Inserting these into the equation $\overline{\mu}_B = \sum_i \langle\Sigma^0|\overline{\mu}_i|\Lambda\rangle$ gives the transition moment in terms of the quark moments:

$\mu_{\Sigma\Lambda} = \sqrt{\frac{1}{3}}(\mu_d - \mu_u)$. If, as in Table 1.1, the measured p, n, and Λ moments are used to determine the quark moments, a value of $\mu_{\Sigma\Lambda}/\mu_N = -1.63$ n.m. is obtained which is independent of any assumptions about the quark masses.

Alternatively, in a constituent quark model, a mass can be assigned to the quark on the basis of the baryon mass spectrum. If this quark mass is put into the Dirac moment, $\mu_i = \frac{q\hbar}{2mc}$, then the baryon moments can be calculated. In the limit of exact SU(3) symmetry, the masses of the u, d, and s quarks are identical[19]. This implies that the quark moments are related to each other by the ratio of their charges: $\mu_d = \mu_s = -2\mu_u$.

Although the μ_d/μ_u ratio yields $\mu_p/\mu_n = -3/2$ which is close to the experimental determination, μ_s/μ_d is inconsistent with the measured moments of the strange baryons. Non-degenerate masses within the baryon decuplet and octet also indicate that the SU(3) symmetry is not exact. The baryon mass spectrum can be fairly well described by assuming that the symmetry breaking is only in the quark masses, the s quark being heavier than the u and d quarks. A generalized one-gluon exchange force between quarks gives rise to a dynamical explanation for the observed mass spectrum (including the Σ-Λ and Δ-N mass differences) as

hyperfine splitting in the Color field[20]. The actual quark masses obtained depend upon the model used, but hover around $m_u = m_d = 330$ MeV/c² and $m_s = 1.67 m_u = 550$ MeV/c². These numbers come from the harmonic oscillator potential of the Isgur-Karl model[21]. The value of $\mu_{\Sigma\Lambda}$ obtained from these constituent quark masses is -1.64 n.m.

The constituent quark model gives qualitative agreement with the experimental moments, but there are still discrepancies, even in the p, n, and Λ moments. Specifically, the predicted μ_p/μ_n ratio is 3% too high, suggesting that $\mu_d < -\frac{1}{2}\mu_u$. Corrections arising from pion cloud contributions reduce the effective magnetic moment of the d quark and could be responsible for this discrepancy[22]. The value of $\mu_{\Sigma\Lambda}$ could be useful in addressing this problem since it depends only on the difference between μ_d and μ_u.

Modifying μ_d/μ_u does not eliminate the other existing discrepancies which are as large as 30%. This can be seen by comparing columns 1 and 2 of Table 1.1 where μ_d/μ_u has been adjusted to give the experimental μ_p/μ_n ratio. It can be further observed in the poor χ^2 obtained by a global fit to all the measured static moments[23] of (a) $\frac{\chi^2}{d.f.} = 57/6$ ($\mu_u = -2\mu_d$) or (b) $\frac{\chi^2}{d.f.} = 44/5$ (unconstrained). Such a fit predicts (a) $\mu_{\Sigma\Lambda} = -1.52$ n.m. and (b) $\mu_{\Sigma\Lambda} = -1.60$ n.m.

Numerous schemes have been put forth to address this problem. They usually proceed by relaxing one of the naïve assumptions present in a non-relativistic, s-wave system of confined pointlike quarks. Relativistic corrections and configuration mixing have made some global improvement in the discrepancies,[24-28] but only by a few percent. Additional symmetry breaking can also be introduced, either as a u-d mass difference[23,28,29] or by making the quark mass dependent on its baryon bound state.[30,31,32] Again, the improvement is slight. In general, the predictions for $|\mu_{\Sigma\Lambda}|$ which are obtained from such "fine-tuned" models are smaller than that obtained by the naïve model: 1.21 n.m.,[29] 1.35 n.m.,[30] 1.46 n.m.,[31] and 1.45 n.m.[32] These values are also smaller than the new world average of 1.61 ± 0.07 n.m.. Since $\mu_{\Sigma\Lambda}$ is not usually included as input to a global fit, the higher experimental value indicates that the global improvements noted above may be accidental. Lipkin[33] notes that the experimental moments of the Σ and Ξ seem to indicate that the u and d-quarks are reduced ("quenched") in the presence of the s-quark. Again, if this were the case, then $|\mu_{\Sigma\Lambda}|$ should yield a smaller value than it does. Correcting for both relativistic effects (estimated from the bag model) and configuration mixing in the Isgur-Karl model[25] also reduces the $|\mu_{\Sigma\Lambda}|$ prediction (from 1.64 n.m. to 1.51 n.m.).

Comparison of the radiative decay widths in the meson sector also show serious discrepancies with the naïve quark model. The Σ^0-Λ transition moment provides an interesting link between the two sectors; as a baryon it should be related to the baryon constituent quark moments, yet it is actually a measurement of a decay width by the Primakoff method in much the same way as the meson experiments. Geffen and Wilson[28] have shown that the correction needed for both baryon and meson sectors is comparable when interpreted as an effective anomalous quark moment (see also references 34 and 35). Their global fit includes configuration mixing, but predicts a larger $|\mu_{\Sigma\Lambda}|$ of 1.96 n.m.

In conclusion, although the quark model is qualitatively correct in its predictions of the meson radiative widths and baryon moments, it is very difficult to obtain a better match by correcting some of the naïve assumptions. Better limits on the measured baryon moments, including the transition moment, may eventually point to a solution, but as yet they only serve to underline the discrepancies. A more promising avenue may be theories which proceed from a more dynamical basis. Lattice gauge calculations[1] are still too limited to have much predictive power, but Bag models[36-40] are beginning to approach the same level of accuracy as the naïve quark

model without recourse to extra parameters like the constituent quark masses. In the end they may be able to shed some light on the shortcomings of the naïve quark model, or perhaps tell us why it works so well!

APPENDIX A

TDC Event Offset Problem

A-1. Introduction

The drift chamber wire information and timing information for the 90 lead glass blocks were read out through four TDC modules. Unfortunately, a combination of several malfunctions caused TDC information from one event to be associated with spectrometer data from a different one. Since the experiment was dependent on the drift chambers to obtain the necessary charged track resolution, this problem could not be ignored. The effect was not discovered until after the experiment was over because the problem only occurred about 50% of the time, which meant that a first attempt at calibrating the drift chambers showed a concentration of events in a reasonable TDC counts/time pattern with a large background of randomly placed hits. In other words, the event offset problem masqueraded as a resolution problem. When the truth was finally realized, only correctly correlated events were used to obtain the calibration and resolution described in Section 2.10. The calibration constants were then used along with the MWPC

tracks to determine the degree of the event shift for each TDC.

A-2. The Cause of the Event Offset Problem

The event confusion was caused by a combination of poor TDC design and insufficient buffer space for certain anomalously large event records. The TDC model in question, LeCroy 2770A, maintained a 40 word FIFO memory in which wire addresses and timing information were stored for each event, separated by end-of-event (or end-of-TDC) words. At random intervals, events occurred in which bursts of noise in the spectrometer set the latches for huge numbers of MWPC wires. The number of hits exceeded the maximum assigned event length, thus preventing completion of the CAMAC list commands. Since the TDC's were the last item on the list, an F2 command (read and shift registers) was not sent to the TDC for these types of events. Instead, the contents of the register were read by the next event, thus incrementing the event offset between spectrometer and TDC data.

Another process acted to decrease the offset. If too many MWPC wires were hit for a particular event or if the event offset became large enough, the TDC memory overflowed. This resulted in a partial TDC event record with no end-of-event word. After another read shifted the registers,

TDC information from the next event was appended to the previous partial event record. When the contents of this register were read out, the two events appeared as one. These two competing processes had the effect of changing the event offset between the drift chambers and the rest of the data in an apparently random fashion. Since the anomalous events varied in record length, the offset shifted independently in each TDC. Furthermore, the CAMAC initiated Clears between beam spills, which would have reduced the effect considerably, did not work on these modules as advertised.

A-3. Drift Chamber Event Offset Correction

Calibration constants were obtained from a sample of obviously correlated hits in the infected tapes and data from the few tapes which were actually free of the problem in the drift chamber TDC's. Once calibration constants were known, the drift chamber hits were transformed to x and y coordinates and scanned to find the hit closest to each MWPC track per chamber per xy plane per event. A buffer of the previous ten events was subjected to this scrutiny. If the closest hit was within 1 cm of the fitted track, it and its partner on the ambiguity plane (if extant) were retained. Corrections were made for two charged tracks entering the same or adjoining cells, and thus resetting the TDC.

A code based on the data was then assigned independently to each chamber for each of the ten buffered TDC events. The higher the code, the higher the probability that the buffered TDC information was associated with the event in question. An important correlation criterion was the fact that the offset tended to stay stable for a while before shifting. Therefore, events with the same offset as the previous match were preferentially coded. Each correlation per track per xy plane also incremented the code. Since all the protons passed through a narrow central region it was relatively easy to find a false correlation for the proton track. Therefore, the π^- track was weighted more heavily. Another positive criterion was the existance of both partners of an ambiguity pair with a sum of drift lengths within 1 mm of the cell size (track slope included).

Offsets ranged from 0-4 events, typically shifting every 20-100 events. The program found correlated drift chamber information for 90-98% of the events. Of that information about 20% are probably false correlations caused by the narrowness of the beam cone through these upstream chambers (see Section 3.9). Poor correlations were later eliminated by second pass χ^2 tests.

A-4 Lead Glass Event Offset Correction

The TDC offset problem also affected the timing information for the lead glass array. Since ADC information existed for each block, unscrambling the TDC information was a much easier job. It only required matching the set of blocks recorded by the TDC's to the same set of ADC blocks. Some care was taken to make the matching criteria loose enough to account for the variation of TDC thresholds and for missing information in either the ADC or the TDC.

Glass TDC offsets ranged from 6-12 events and the correlation search extended to 25 events. About 10-15% of the glass TDC data was actually lost due to event offset shifts and the efficiency of the unscrambling procedure was approximately 75%. Thus about 65% of the events had block timing information restored. However, the percentage of hits with timing information in the final cut analysis sample is higher (near 83%). The degree of the offset problem for both glass and drift chambers varied enormously from run to run. The quoted efficiencies and data losses are averages.

APPENDIX B

The Primakoff Cross Section

B-1. Formulae and Definitions

In the original paper by Dreitlein and Primakoff[6] (DP), an approximation was made which, although justified in the context of that report, cannot be used at the present level of experimental accuracy. Eq. 11b of DP is

$$\frac{m_{\Sigma^0}^2 - m_\Lambda^2}{2m_{\Sigma^0}} \approx 0.97(m_{\Sigma^0} - m_\Lambda) \qquad \text{(B.1)}$$

This substitution is made in subsequent equations and the factor 0.97 is dropped. When numerical factors are evaluated in Eq. 35a of DP the approximation amounts to $-(0.97)^5$, yielding the coefficient 70 mb/sr.

The value of 70 mb/sr was subsequently used in Dydak et al.[18] and in the Wilkin computer program[15] used by them to obtain the theoretical cross sections. To the best of our knowledge, all the equations on this topic in Fäldt's paper[8] are correct. In order to clarify the situation for future

workers, we set down here the correct formulae. The numerical values of the masses and the other constants used in evaluating the factors are from The Particle Data Group (Rev. Mod. Phys. 56, Part II (1984)):

$$m_{\Sigma^o} = 1.19246 \text{ GeV}/c^2$$

$$m_\Lambda = 1.11560 \text{ GeV}/c^2$$

$$m_p = 0.9382796 \text{ GeV}/c^2$$

$$\hbar = 6.582173 \times 10^{-6} \text{ (GeV) } (10^{-19} \text{ sec})$$

$$\hbar c = 0.19732858 \text{ GeV-fm}$$

$$1 \text{ fm}^2 = 10 \text{ mb}$$

$$\alpha = 1/137.03604 \tag{B.2}$$

The relationship between the Σ^o lifetime and the transition magnetic moment is

$$\frac{\mu_{\Sigma\Lambda}}{\mu_N}^2 = \frac{1}{\tau} \cdot \frac{8\,\hbar\, m_p{}^2 m_{\Sigma^o}^3}{\alpha(m_{\Sigma^o}^2 - m_\Lambda{}^2)^3} = 1.92951 \left(\frac{10^{-19} \text{ sec}}{\tau} \right) \tag{B.3}$$

The correct evaluation for Eq. 35a (DP) for the differential cross section is

$$\frac{d\sigma}{d\Omega} = \frac{8\, Z^2 e^2 m_{\Sigma^o}^3}{(m_{\Sigma^o}^2 - m_\Lambda{}^2)^3\, \delta^2} \cdot \frac{\delta^2\, \theta^2}{(\delta^2 + \theta^2)^2} \cdot \frac{1}{\tau} \tag{B.4}$$

where $\delta = (m_{\Sigma^o}^2 - m_\Lambda{}^2)/2p_\Lambda{}^2$ and $\theta = \Sigma^o\text{-}\Lambda$ production angle.

After inserting all the factors needed to get practical units, this becomes

$$\frac{d\sigma}{d\Omega} = \frac{320\ (82)^2\ \alpha\ m_\Lambda{}^4 m_{\Sigma^\circ}^3\ \hbar\ (\hbar c)^2}{(m_{\Sigma^\circ}^2 - m_\Lambda{}^2)^5}\ \frac{mb}{sr} \quad \times$$

$$\left(\frac{p_\Lambda}{m_\Lambda}\right)^4 \left(\frac{10^{-19}\ sec}{\tau}\right)\left(\frac{Z}{82}\right)^2 \frac{\frac{\theta^2}{\delta^2}}{(1 + \frac{\theta^2}{\delta^2})^2}$$

$$= (60.16172\ \frac{mb}{sr})\left(\frac{p_\Lambda}{m_\Lambda}\right)^4 \left(\frac{10^{-19}\ sec}{\tau}\right)\left(\frac{Z}{82}\right)^2 \frac{\frac{\theta^2}{\delta^2}}{(1 + \frac{\theta^2}{\delta^2})^2} \qquad (B.5)$$

This appears also in a slightly modified form in Eq. 3 of Ref. 18, for which the correct expression is

$$\frac{d\sigma}{dt} = \frac{d\sigma}{dq_t{}^2} = \frac{\pi\ d\sigma}{p_\Lambda{}^2 d\Omega} = (60.16172\ \pi\ mb)\ \frac{p_\Lambda{}^2}{m_\Lambda{}^4}\left(\frac{10^{-19}\ sec}{\tau}\right)\left(\frac{Z}{82}\right)^2 \frac{q_l{}^2 q_t{}^2}{q^4} \qquad (B.6)$$

where $q_t = p_\Lambda\theta$ and $q_l = p_\Lambda\delta$ are the transverse and longitudinal momentum transfer and $q^2 = q_l{}^2 + q_t{}^2$.

A useful related expression where the lifetime is replaced by the moment is

$$\frac{d\sigma}{dt} = (97.954\ mb)\ \frac{p_\Lambda{}^2}{m_\Lambda{}^4}\left(\frac{\mu_{\Sigma\Lambda}}{\mu_N}\right)^2 \left(\frac{Z}{82}\right)^2 \frac{q_t{}^2 q_l{}^2}{q^4} \qquad (B.7)$$

In all of the cross section expressions, we have omitted the form factor $F(q^2)$ which is discussed in DP and also in Fäldt[8].

B-2. Corrections to the Dydak et al. Cross Section

The procedure used in Dydak et al.[18] to calculate the lifetime and transition moment can be improved by two modifications: the use of more exact expressions for the theoretical cross sections and the order in which reciprocals and weighted averages are performed. Although the resulting change is within their quoted uncertainties, it is worth correcting their result before comparing to the present result or forming a weighted average of the two experiments.

Table 1 of Ref. 18 contains the measured and theoretical (based on $\tau = 10^{-19}$ sec) cross sections. The values of the theoretical cross sections contain the ~14% error discussed above. The lifetime was computed from the ratio $\sigma_{theor}/\sigma_{meas}$ with no attention to the asymmetry in the uncertainties of the reciprocal. The lifetimes were then averaged and the reciprocal again taken to determine $(\mu_{\Sigma\Lambda}/\mu_N)^2$, at which point the asymmetric propagation of uncertainties was taken into account. Finally, the square root was performed, again with correct uncertainty propagation, to obtain $|\mu_{\Sigma\Lambda}/\mu_N|$.

The values of σ_{theor} were based on a computer program, PRIMAK, of Wilkin[15]. Using PRIMAK in its original form, we were able to reproduce the quoted values of σ_{theor} for Uranium (5 momentum bins) assuming a nuclear radius of $R(A) = (1.20\ fm)A^{\frac{1}{3}}$, a lambda-nucleon total cross section of 34.0 mb,[17] a nucleon radius of 0.94 fm, and the coefficient of 70 mb from Eq. 3 of Dydak et al.

We were unable to reproduce the values of σ_{theor} for Nickel (4 momentum bins) with any reasonable choices for the constants. However, if we assumed that the momentum bins for Ni were actually 2 GeV lower than those quoted in the table, then σ_{theor} for Ni were reproduced. The Ni data have one less momentum bin than the Uranium data. From the information in the table, the lowest bin was dropped. On the other hand, the momentum spectrum in Fig. 5 of Dydak et al. shows the highest bin to be the least populated, and, therefore, more likely to be dropped. We have proceded on the assumption that the momentum bins for Ni in the original table are mislabelled by 2 GeV.

Subsequently, we corrected the numerical factors in PRIMAK and re-ran it to produce a revised set of values for σ_{theor} for $(\mu_{\Sigma\Lambda}/\mu_N)^2 = 1.00$. Further, we assumed $R(A) = (1.14\ fm)A^{\frac{1}{3}}$, $\sigma_{\Lambda N} = 34.0$, a nucleon radius of 0.94 fm, and a numerical coefficient of 60.16172 mb for the Primakoff

cross section. (See Eq. B-6 above.) Table B-1 presents our re-analysis of the cross sections of Dydak et al. to obtain the value of $(\mu_{\Sigma\Lambda}/\mu_N)^2$. Since no reciprocals or square roots are taken in this calculation, the symmetric fractional uncertainties propagate to $(\mu_{\Sigma\Lambda}/\mu_N)^2$ and into the weighted average:

$$(\mu_{\Sigma\Lambda}/\mu_N)^2 = 3.07 \pm 0.66$$

The resulting lifetime is

$$\tau = (0.63 \,^{+0.17}_{-0.11}) \times 10^{-19} \text{ sec}$$

and the transition magnetic moment is

$$|\mu_{\Sigma\Lambda}/\mu_N| = 1.75 \,^{+0.18}_{-0.20} \text{ n.m.}$$

Table B-1

Σ^o Production

(A Revision of Table 1 of Dydak et al.[a])

p_{Σ^o}[b] (GeV/c)	Number of Σ^o Events	σ_{meas} (mb)	σ_{theor}[c] (mb)	$\left(\frac{\mu}{\mu_N}\right)^2$	$\left(\frac{\mu}{\mu_N}\right)^2$[d]
on Uranium					
9-11	66 ± 26	3.6 ± 1.5	0.97	3.7 ± 1.5	3.7 ± 2.7
11-13	73 ± 27	2.8 ± 1.1	1.16	2.4 ± 1.0	2.4 ± 1.7
13-15	51 ± 25	2.5 ± 1.3	1.32	1.9 ± 1.0	1.9 ± 1.5
15-17	60 ± 16	5.2 ± 1.5	1.47	3.5 ± 1.0	3.5 ± 1.8
17-19	18 ± 11	4.3 ± 2.8	1.60	2.7 ± 1.7	2.7 ± 2.2
				2.72 ± 0.51[e]	2.65 ± 0.82[e]
on Nickel					
9-11	33 ± 14	0.58 ± 0.26	0.132	4.4 ± 2.0	
11-13	26 ± 15	0.49 ± 0.30	0.151	3.2 ± 2.0	
13-15	23 ± 11	0.68 ± 0.34	0.168	4.0 ± 2.0	
15-17	7 ± 7	0.56 ± 0.59	0.182	3.1 ± 3.2	
				3.80 ± 1.08[e]	

Notes: (a) F. Dydak et al., Phys. Lett. B118, 1 (1977).

(b) Original table quoted momentum bins for Ni 2 GeV higher. See text.

(c) Based on $(\mu/\mu_N)^2=1.00$

(d) Uncertainty includes possible interference with strong coherent production. Scaled from original table.

(e) Weighted Average.

REFERENCES

1. G.Martinelli et al., Phys. Lett. 116B, 434 (1982); Phys Lett. 117B, 434 (1982).
   C. Bernard et al., Phys. Rev. Lett. 49, 1076 (1982).

2. H. Rubinstein, F. Scheck, and R. H. Socolow, Phys. Rev. 154, 1608 (1967).
   J. Franklin, Phys. Rev. 172, 1807 (1968); Phys. Rev. 182, (1969).

3. For a good explanation of the method, see L. Schachinger et al., Phys. Rev. Lett. 41, 1348 (1978).

4. D. W. Hertzog et al., Phys. Rev. Lett. 51, 1131, 1813(E) (1983).

5. J. Sucher, Rep. Prog. Phys. 41, 1781 (1978).

6. J. Dreitlein and H. Primakoff, Phys. Rev. 125, 1671 (1962).

7. I. Ya. Pomeranchuk and I. M. Schmushkevitch, Nucl. Phys. 23, 452 (1961).

8. G. Fäldt et al., Nucl. Phys. B41, 125 (1972).

9. P. Skubic et al., Phys. Rev. D18, 3115 (1978).
   A. Beretvas et al., to be submitted to Phys. Rev. (1985).

10. P. Skubic, Ph.D. thesis, "Neutral Strange Particle Production from Nuclear Targets by 300 Gev Protons" (Univ. of Mich. 1977).

11. R. L. Ford and W. R. Nelson, SLAC-210 (1978).

12. J .F. Bartlett et al., "RT/RSX MULTI: Packages for Data Acquisition and Analysis in High Energy Physics", Topical Conf. on Computerized Data Acquisition Systems in Particle and Nuclear Physics. Santa Fe, New Mexico (1979).

13. J. B. Marion and B. A. Zimmerman, Nucl. Inst. Meth. 51, 93 (1967). (In particular, Table 1 for B=6)

14. V. L. Highland, Nucl. Instr. Meth. 129, 497 (1975).

15. C. Wilkin (Private Communication).

16. T. Devlin (Private Communication).

17. S. Gjesdal et al., Phys, Lett. 40B, 152 (1972).

18. F. Dydak et al., Nucl. Phys. B118, 1 (1977).

19. S. Coleman and S. L. Glashow, Phys. Rev. Lett. 6, 423 (1961).

20. A. DeRujula, H. Georgi, S. L. Glashow, Phys. Rev. D12, 147 (1975).

21. N. Isgur and G. Karl, Phys. Rev. D20, 1191 (1979).

22. G. E. Brown, M. Rho, and V. Vento, Phys. Lett. 97, 423 (1980).

23. J. Franklin, Phys. Rev. D29, 2648 (1984).

24. H. J. Lipkin, Phys. Lett. 35B, 534, (1971).

25. N. Isgur and G. Karl, Phys. Rev. D21, 3175 (1980).

26. J. Franklin, Phys. Rev. Lett. 45, 1607 (1980).

27. J. Franklin, Phys, Rev. D20, 1742 (1979).

28. D. A. Geffen and W. Wilson, Phys. Rev. Lett. 44, 370 (1980).

29. Y. Tomozawa, Phys. Rev. D19, 1626 (1979).

30. S. Oneida et al., Paper no. 819: XX Intl. Conf. on High Energy Physics, Madison, Wisconsin (1980).

31. R. C. Verma, "Magnetic Moments of Baryons in Broken Spin-Unitary-Spin Symmetry." Univ. of Alberta Report Thy-5-80.

32. R. B. Teese and R. Settles, Phys. Lett. 87B, 111 (1979).

33. H. J. Lipkin, Phys. Rev. D24, 1437 (1981).

34. Y. Dothan, Phys. Rev. D27, 2139 (1983).

35. A. Bohm and R. B. Teese, Phys. Rev. D18, 330 (1978).

36. A. Chodos et al., Phys. Rev. D9, 3471 (1974) (MIT Bag Model).

37. T. DeGrand et al., Phys. Rev. D12, 2060 (1975) (MIT bag with massive quarks).

38. T. Barnes, Nucl. Phys. B96, 353 (1975) and
E. Allen, Phys. Lett. 57B, 263 (1975) (symmetry-breaking with a massive s-quark).

39. J. F. Donoghue and K. Johnson, Phys. Rev. D21, 1975 (1980) (recoil corrections).

40. S. Theberge and A. W. Thomas, Phys. Rev. D25, 284 (1982) (Cloudy Bag Model).

CURRICULUM VITAE

Priscilla Cushman Petersen

1954 ..... Born April 2 in Meriden, Connecticut.

1972 ..... Graduated from Ethel Walker School, Simsbury, Connecticut.

1972-1976 .. Attended Harvard University, Cambridge, Massachusetts. Majored in Physics and Philosophy.

1972-1974 .. Research Technician with Harvard College Observatory. (Atomic Physics Group)

1974-1976 .. Worked for Smithsonian Observatory on Einstein and UHURU satellites. Senior Honors Thesis: "An X-Ray Luminosity Function for Rich Clusters of Galaxies." Center for Astrophysics Preprint, 1977.

1976 ..... B.A., Harvard University.

1976-1979 .. Senior Staff Scientist for Aeronautical Research Associates of Princeton.

1977 ..... Article: "The Ignition, Combustion, and Radiant Intensity of Spherical Clouds of Hydrogen." ARAP Report no. 241, April 1977.

1977 ..... Article: "Ultraviolet Single Scattering Phase Functions of Naturally Occuring Atmospheric Aerosols." ARAP Report no. 314, September 1977.

1978 ..... Article: "An Analytical Investigation of the Effects of Scattering on the Ultraviolet Radiation Emitted by Particulate Laden Plumes." 8th Tri-Service UV Technology Meeting, Air Force Avionics Laboratory, WPAFB, Ohio, July 1978.

1978 ..... Article: "Atmospheric Propagation of Ultraviolet Radiation through the Lower Atmosphere." 8th Tri-Service UV Technology Meeting, Air Force Avionics Laboratory, WPAFB, Ohio, July 1978. ARAP Report no. 374, Nov. 1978.

1979 ..... Article: "Seasonal Variation of Single Scattering Phase Functions in the Ultraviolet." 8th Tri-Service UV Technology Meeting, Air Force Avionics Laboratory, WPAFB, Ohio, July 1978. ARAP Report no. 383, Feb. 1979.

1979-1981 .. Teaching Assistant in the Physics Dept., Rutgers University.

1981-1985 .. Graduate Assistant in High Energy Experimental Physics. Thesis Experiment: "The Σ°-Λ Transition Magnetic Moment" was performed at the Fermi National Lab, Batavia, Illinois, in 1982.

1982 ..... Article: "Polarization of Inclusively Produced Hyperons." AIP Conference Proceedings 95.

1982 ..... Article: "Search for Polarization in $\overline{\Xi^{\circ}}$ Hyperons." AIP Conference Proceedings 95.